Edge states in Chern Insulators and Majorana fermions in topological superconductors

Doru Sticlet

Université Paris-Sud

École doctorale: Physique de la région parisienne

Laboratoire de Physique des Solides

Discipline: Physique Théorique

Thèse de doctorat

soutenue le 27 Novembre 2012

par

Doru C. **Sticleț**

Edge States in Chern Insulators and Majorana Fermions in Topological Superconductors

Composition du jury:

Gilles **Montambaux**	Président du jury
David **Carpentier**	Rapporteur
Gil **Refael**	Rapporteur
Julia S. **Meyer**	Examinatrice
Karyn **Le Hur**	Examinatrice
Pascal **Simon**	Directeur de thèse
Frederic **Piéchon**	Membre invité

Contents

Acknowledgments

Here you have a thesis with an author on its covers. Nevertheless, it is not the contribution of one voice. It conveys the results of a continuous dialog. Sometimes it involved a mute relation with articles and books, but, at its best, it was an exchange of ideas with the people in the scientific community. Here are some of them...

I thank my thesis advisor, Pascal Simon, for his unrelenting drive and his ability to spot open directions for research. The work on Majorana fermions is particularly indebted to the fruitful collaboration with Cristina Bena and Denis Chevallier. Our joint work deserves future cooperation.

A special thanks is owed to the unofficial thesis advisor, Fred Piéchon. Countless hours spent circling around the subject of topological insulators taught me the meaning of research in physics. His availability for intelligent discussion was a fuel for many ideas developed in this thesis.

Thanks to my colleagues, LPS has become in three years a welcoming environment for studying the topological matter. Hopefully, the influence of the clear and sharp mind of Jean-Noël Fuchs transpires in the following pages. His scientific generosity has benefited all people around him. The same can be said about the good-humored Marc Goerbig, who made coffee breaks an occasion to learn physics wrapped in anecdotes.

It is hard to match the fortuitous encounters with Pavel Kalugin. The few moments in which I shared his mathematical perspective on the subject of topological insulators were transcending.

I also benefited from discussion with Gilles Montambaux, Pierre Delplace, Rafaël de Gail, Lih-King Lim, Guangquan Wang and Clément Dutreix. The "graphene-people" are naturally close to the topics presented inside this thesis and, even unknowingly, have shaped the formulation of ideas presented here.

It was a pleasure to collaborate with François Crépin, who made discussions about bosonization and renormalization fun. I cannot forget several discussions with the ever-inquisitive Nicolas Thiébaut. I hope our topics will meet in the future and the blackboard discussions can turn in a collaboration. In the same vein, I thank to Emilio Winograd, Jean-René Souquet, Yi Liu, Mattias Albert, Nicolas Charpentier, and Ilya Belopolski for introducing me into their respective fields of research. It is true that science is just

a big system of communicating vessels. It was a pleasure to share ideas with Jason Alicea. Talking with him was as illuminating as reading his clear articles. Misha Polianski is a lost friend; his presence inspired my first year of PhD and his sudden disappearance cannot delete his memory.

When mathematics became disorienting, Adrian Viorel, Ioan Mărcuț, and Ori Yudilevich were always available for discussions. Thank you!

All physicists that crossed path with me in the institute, in courses, in summer schools etc. deserve a mention. Alas, only some of them could be named in this brief acknowledgment. Furthermore my gratitude is extended to all the people at the LPS, who made the institute such a comfortable place for research.

Finally, nothing would have been possible without my family. When the long days in a foreign land turned bleak, they always brightened them up.

Introduction

The recent years have witnessed a revolution in condensed matter physics. It consisted in discovering a wealth of new phases of matter that are not distinguished by broken symmetries, but from the topology of the wave-functions describing the system [1–3]. The tremendous work from recent years has a starting point in the theoretical proposal of two-dimensional $\mathbb{Z}_2$ topological insulators (the quantum spin Hall insulators) [4, 5] and the rapid experimental discovery in HgTe/CdTe quantum wells [6]. Soon after, it was understood that the 2D quantum spin Hall insulator is but an instance of possible topological insulators and superconductors. Venerable phenomena such as the Shockley surface states [7], the topological excitations in the Su-Schrieffer-Heeger polymer chain [8], the integer quantum Hall effect [9], and many others, were all put together as pieces of a greater picture; these phenomena crucially depend on the presence of edge states that are manifestations of topological phases in a gapped bulk.

The topological insulators and superconductors share the same intriguing feature: the presence of robust edge states in the bulk gap. For example, the edge states are not removed under the action of weak disorder which does not close the bulk gap. Hence the persistence of these states cannot be attributed to the point group symmetries, which can be destroyed in the presence of disorder. In the absence of point group symmetries, one is left with at least two basic discrete symmetries: time-reversal symmetry (TRS) and charge conjugation or particle-hole symmetry (PHS). They form the basis for the classification of non-interacting gapped Hamiltonians in arbitrary dimensions [10]. This allowed to group the Hamiltonians into ten classes in each spatial dimension.

More precisely, the time-reversal and charge conjugation acting on a Hamiltonian matrix, in a basis of creation and annihilation operators, are represented by the anti-unitary operators, $\mathfrak{T}$ and $\mathfrak{C}$, that can square to ± 1 [11]. Then, counting also the possibility that the system is not invariant under these symmetries, there are 9 possible classes. A third chiral or sublattice symmetry (SLS) is represented by a unitary operator $\mathfrak{S} = \mathfrak{T}\mathfrak{C}$. The value of $\mathfrak{S}$ is entirely determined by the behavior of $\mathfrak{C}$ and $\mathfrak{T}$, except in the particular case where SLS is a symmetry of the system when both TRS and PHS are broken. This case raises the number of symmetry classes to 10 [11]. The resulting classification is represented in Tab. 1.

System	Cartan nomenclature	TRS	PHS	SLS	$d=1$	$d=2$	$d=3$
standard (Wigner-Dyson)	A (unitary)	0	0	0	-	$\mathbb{Z}$	-
	AI (orthogonal)	$+1$	0	0	-	-	-
	AII (symplectic)	-1	0	0	-	$\mathbb{Z}_2$	$\mathbb{Z}_2$
chiral (sublattice)	AIII (chiral unit.)	0	0	1	$\mathbb{Z}$	-	$\mathbb{Z}$
	BDI (chiral orthog.)	$+1$	$+1$	1	$\mathbb{Z}$	-	-
	CII (chiral sympl.)	-1	-1	1	$\mathbb{Z}$	-	$\mathbb{Z}_2$
BdG	D	0	$+1$	0	$\mathbb{Z}_2$	$\mathbb{Z}$	-
	C	0	-1	0	-	$\mathbb{Z}$	-
	DIII	-1	$+1$	1	$\mathbb{Z}_2$	$\mathbb{Z}_2$	$\mathbb{Z}$
	CI	$+1$	-1	1	-	-	$\mathbb{Z}$

Table 1: Classification of free fermionic gapped Hamiltonians as a function of symmetries: TRS, PHS and SLS. The dimensionality is denoted by d. The present thesis touches almost exclusively models belonging to the classes marked in red. (Table taken from Ref. [13].)

Furthermore, not all gapped ground states for a given class are identical. Five classes in every dimension have gapped ground states that are divided into topological sectors. The Hamiltonians in these classes form the topological insulators and superconductors [11–14]. Note from Tab. 1 that they have associated a descriptor, $\mathbb{Z}$ or $\mathbb{Z}_2$. This denotes the topological invariant that describes the ground state of the system and is used throughout to identify the type of topological insulator (superconductor). The invariant counts how many distinct gapped phases are in a specific class: only two, $\mathbb{Z}_2$, or a numerable infinity of phases, $\mathbb{Z}$. Always one of the gapped phases is trivial in the sense that it can be adiabatically connected to the vacuum. Passing from a gapped phase to another requires closing the bulk gap [12]. Connecting two topologically distinct gapped phases of topological insulators (superconductors) creates an interface where edge states appear. This general result is called the bulk-boundary correspondence [15, 16] and is the basis of the physics grown around the subject of topological insulators (superconductors). The *robust* edge states are a consequence of connecting ground states with different values of the topological invariant. Adding a weak perturbation that obeys the symmetries specific to a class, cannot destroy these states.

From a practical perspective the robustness of edge states constitutes a central motivation to study the topological materials. For example in 2D and 3D, the edges harbor quantized metallic states that are robust with respect to disorder and could carry current without dissipation. A prime example are the integer quantum Hall edge states. They belong to a 2D $\mathbb{Z}$ insulator in class A that is described by an integer topological invariant, the first Chern number $\mathcal{C}$. Weak disorder does not destroy the edge states and, furthermore, they are quantized; they carry current and have a Hall conductance proportional to $\mathcal{C}$ [17–19].

There are five non-interacting topological insulators and superconductors in each

dimension. Nevertheless, not all of them have found an experimental realization. This poses a continuous challenge to condensed matter physics; from the experimental point of view, it is to find or engineer systems that will support topological phases of matter and, of course, to detect these exotic states of matter. The theoretician needs to propose possible candidates, imagine detection schemes and good quantities to measure. Furthermore, the road ahead is not entirely mapped. At the moment, it still remains to have a systematical view of the topological matter in the context of interacting systems. Already the classification schemes for free Hamiltonians need to be revised in this new light [20–22].

In this thesis

The present thesis will not dwell on the abstract matters concerning the classification of topological insulators and superconductors. It is applied entirely to non-interacting topological insulators and superconductors as the ones classified in Tab. 1. The table should be used to pinpoint the object of the present study in a more general context.

The thesis is divided into two parts. Each one will receive a more detailed introduction at its respective beginning. It suffices here to draw the main directions of research.

The first part of the thesis is focused mostly on 2D topological insulators in class A. The most famous inhabitant was already named: the integer quantum Hall effect (IQHE). Here TRS is broken through an external magnetic field. However, a different possibility exists, that was first illustrated by Haldane [23]. Theoretically the IQHE physics can arise in the absence of an external field, by adding fluxes at the scale smaller that the cell size, but which cancel overall. Thus TRS is still broken, and one could expect dissipationless current at zero magnetic field. Such a model did not have an experimental fulfillment, but was central in imagining the first $\mathbb{Z}_2$ insulator in graphene [4]. Due to its connection to IQHE, the $\mathbb{Z}$ insulator was named quantum anomalous Hall (QAH) insulator. The topological invariant characterizing the 2D QAH insulators remains a Chern number.

The present study focuses mostly on minimal two-band models of QAH insulators and investigates the conditions for the production of bands with high Chern number. The nontrivial aspect of the research is that the high Chern number is not obtained by multiplying the bands, but by creating a *single* band with a high Chern number. This is reflected as usual in a multiplication of the edge channels.

Chap. 1 is concerned entirely with the bulk characterization of QAH insulators in a tight-binding formulation. It is shown how one can simplify the treatment of these models to the study of systems with Dirac points. Subsequently, producing higher Chern number reduces in this case to the requirement that the nodes in the dispersion for gapless models are multiplied through addition of hopping terms between distant sites. The theory is first put to test in the context of an endogenous artificial model with five Chern phases, and, secondly, by modifying the QAH Haldane model.

Chap. 2 contends mostly with numerical and analytical solutions for edge-state wave

functions in a model with Chern $|\mathcal{C}| = 2$. Moreover, a few extensions to four-band models are analyzed using the methods developed in the previous chapter, and their topological phase diagram is determined.

The second part of the thesis is centered around the study of Majorana fermions in a spin-orbit coupled semiconducting wire in the proximity of an s-wave superconductor [24, 25]. This physical system realizes a one-dimensional topological superconductor in class D (see Tab. 1) that supports particular edge states: the Majorana fermions. An introduction to these fascinating (quasi)particles is offered in Chap. 3.

In Chap. 4 the system is reconsidered in the presence of Dresselhaus spin-orbit interaction. It is shown that the spin of the electronic degrees of freedom of the zero-energy edge modes responds to ratio between the Rashba and Dresselhaus spin-orbit coupling. There is an opposite spin-polarization of the edge modes, in a direction transverse to a magnetic field, which could be accessible through tunneling spectroscopy. The following chapter (5) considers hybrid structures of the types: superconductor-normal and superconductor-normal metal-superconductor built upon the aforementioned system. Furthermore, it investigates ring geometries, under the action of a uniform superconducting phase gradient, which in certain condition can be mapped to a SNS heterostructure. The central interest lies in the extended nature of Majorana fermions that develop in the normal part of the heterostructures.

Finally, Chap. 6 changes gears and touches upon Majorana fermions in a two-band tight-binding BDI class superconductor. The interest lies in the fact that the system is described by a $\mathbb{Z}$ topological invariant and supports *several* Majorana fermions at its edge (see Tab. 1). It is important to note the connection with the $\mathbb{Z}$ insulators treated in the first part. The same mechanism, i.e. addition of coupling terms between distant sites, is responsible for creating multiple zero modes. Conclusion and possible perspectives are contained in the final chapter.

Part I

Topological insulators

Chapter 1

Quantum anomalous Hall phases in a two-dimensional Chern insulator

1.1 Introduction

The quantum spin Hall (QSH) insulator that debuted the recent excitement in the field of topological insulators (and superconductors) [1–3] has one important precursor which is the subject of the first part of this thesis. It is the quantum anomalous Hall (QAH) insulator that received a first theoretical realization in the work of Haldane [23]. It is a $\mathbb{Z}$ insulator that has chiral edge states similar to those of integer quantum Hall effect (IQHE) with the crucial difference that they exist in zero magnetic field. A QAH insulator in two dimensions exists only in class A, which lacks TRS, PHS or the sublattice symmetry (see Tab. 1). It will be also referred in the following as a Chern insulator due to the fact that it is described by a Chern topological invariant $\mathcal{C}$. Because it requires no particular discrete symmetry, one expects that edge state of this system are extremely robust, similarly to the ones in IQHE [9]. Furthermore, it acquires a quantized Hall conductivity proportional to the Chern index, $\sigma_H = \mathcal{C} \times e^2/h$.

The Haldane tight-binding model is treated in more detail in Sec. 1.4. It suffices to say that it describes spinless electrons and the TRS is broken through currents induced at a scale smaller that the cell size. More generally, in a spinful system such physics could be caused by magnetic ordering in the presence of spin-orbit interaction [23, 26]. Theoretical proposals to realize QAH invoke effects of disorder in metallic ferromagnets [26] or magnetic doping of QSH insulators [27]. However, to this moment, there is no indisputable physical realization of the QAH insulator, and only recently experimentalists claim detection in magnetic topological insulators [28]. By contrast, the QSH effect was ostensibly investigated in HgTe/CdTe quantum wells [6]. The birth of the QSH insulator is related to the insight that combining a QAH insulator with its time reversal copy produces a time-reversal invariant (TRI) $\mathbb{Z}_2$ insulator that can have spin-polarized chiral edge states [4].

The question that drives the first part of the thesis is how to determine efficiently the topological invariant for the case of a two-band non-interacting Chern insulator (see Sec. 1.2). Moreover, how can one multiply the topological phases in the system while keeping only two bands? Equivalently, how can there be a single band with a large Chern number? Note that without the two-band constraint, the answer must follow the same lines of the IQHE; the number of edge channels is multiplied by having more bands [29, 30]. The search for bands with high Chern numbers in QAH insulators has recently intersected with the study of flat band topological models in which it is expected to encounter fractional quantum Hall effect [31–33]. In this context, the search for high Chern numbers was motivated by the need to discover physics above the lowest Landau level [34–37].

The short general answer that is elaborated in the present thesis claims: a single band can increase its Chern number by adding distant-site hoppings in the system [38]. (The same question was answered in the context of flat-band topological models by showing that a multi-band system can be projected to a two-band model with effective distant-neighbor hoppings [37].) In particular, these questions are given a more concrete answer by building a model with five Chern phases in Sec. 1.3 and by creating high Chern phases in the Haldane model in Sec. 1.4. This question can be seen as a bridge to the second part of the thesis, where couplings between distant sites can produce several Majorana modes at a single edge. There the time-reversal and chiral symmetries ensure that they do not hybridize to form regular electronic states (see Chap. 6). The second chapter treats mostly the edge physics in a model QAH insulator. There the question is how to determine analytically and numerically the edge states in a model with $|\mathcal{C}| = 2$. Finally, the chapter contains two extensions that show ways in which the analytical determination of the Chern number can be used in cases of four-band models. Sec. 2.3 treats a four-band TRI $\mathbb{Z}_2$ model. Here the edge states from $|\mathcal{C}| = 2$ are gapped by TRI one-particle perturbation. In Sec. 2.4 the Chern number is used to predict new metallic states that appear in a "striped" topological insulator.

1.2 Bulk characterization of a Chern insulator

1.2.1 Topological invariant

Chern number for a class A insulator in 2D

This subsection contains a description of the topological invariant that characterizes a two-dimensional $\mathbb{Z}$ topological insulator in class A. This insulating system has no chiral symmetry or any of the anti-unitary symmetries: TRS and PHS. Subsequently it is characterized by a Chern number. The main argument advanced here is that the topological invariant can receive a discrete formulation that allows to draw a direct parallel with the physics of Dirac fermions. The discrete formulation of the topological invariant has the added interest that gives an efficient way to compute and discriminate the topologically

insulating phases of a two-band insulators.

The tight-binding Hamiltonian for a free fermion theory is written in a site basis

$$H = \sum_i \varepsilon_i |i\rangle\langle i| + \sum_{ij} t_{ij} |i\rangle\langle j|. \tag{1.1}$$

The on-site energy is given by ε_i and the hopping integrals between different neighbor sites are given by t_{ij}. In the following, only systems without disorder are considered. Therefore the system is invariant under a translation with a Bravais lattice vector. A Fourier transform allows to express the Hamiltonian in reciprocal space

$$H = \sum_{\mathbf{k}\in \mathrm{BZ}} \mathcal{H}(\mathbf{k}) |\mathbf{k}\rangle\langle\mathbf{k}|, \tag{1.2}$$

where $|\mathbf{k}\rangle$ are Bloch states. Because there are no anti-unitary symmetries imposed, the Hamiltonian $\mathcal{H}$ is generally a matrix in $Herm(n)$, the set of $n \times n$ Hermitian matrices with complex coefficients. There are n bands that can be due to the presence of different orbitals per site and nonequivalent atoms in a unit cell. Note that the variable $\mathbf{k}$ is continuous and the Brillouin zone is a manifold, a torus T^2. To each point in the BZ, $\mathcal{H}(\mathbf{k})$ associates a value, and therefore it is a mapping from the torus to the parameter space of $\mathcal{H}$

$$\mathcal{H} : T^2 \to Herm(n). \tag{1.3}$$

Topology enters the discussion with the following question: when are two Hamiltonians $\mathcal{H}$ equivalent? They are equivalent if the functions can be smoothly deformed into each other. From a topological point of view they are homotopically equivalent.

The Chern number indexes the classes of homotopically equivalent functions $\mathcal{H}$. For the multiband system it can be defined using the notion of projector on the occupied bands. If there is a gap between the valence and conduction band, then the phases are indexed by

$$\mathcal{C} = \frac{i}{2\pi} \int_{\mathrm{BZ}} \mathrm{Tr}(dP \wedge PdP), \tag{1.4}$$

where P is the projector on the occupied bands [39].

A non-zero Chern number can be understood as an obstruction to a global gauge choice for the wave function on the BZ. Physically this phenomenon is directly related to the quantization of the Hall conductivity $\sigma_H = \mathcal{C} \times e^2/h$, where $\mathcal{C}$ corresponds to the number of edge states [17, 40].

In the following, the focus is almost entirely on two-band band translation invariant Hamiltonians ($n = 2$). Hence the momentum space Hamiltonian can generally be decomposed in a basis of Pauli matrices

$$\mathcal{H} = \sum_{\mu=0}^{3} h_\mu(\mathbf{k}) \cdot \sigma_\mu. \tag{1.5}$$

The σ Pauli matrices are not given a physical interpretation for the moment. They might refer to a space of two orbitals on a site or two nonequivalent sites in the unit cell. The term $h_0\sigma_0$ just shifts identically the energy bands and does not modify the topology of the Hamiltonian. It is neglected in the following, and therefore the Hamiltonian reads

$$\mathcal{H}(\mathbf{k}) = \mathbf{h}(\mathbf{k}) \cdot \boldsymbol{\sigma}. \tag{1.6}$$

This form is reminiscent of a Zeeman Hamiltonian for a spin $1/2$ particle in a magnetic field, except that the "field" $\mathbf{h}(\mathbf{k})$ is defined in momentum space. There are two energy bands given by

$$E_{\pm} = \pm|\mathbf{h}|. \tag{1.7}$$

For an insulating system, there is always a gap between the bands. Therefore the three vector components of $\mathbf{h}(\mathbf{k})$ never vanish simultaneously, when $\mathbf{k}$ varies in the BZ. Then it follows that the unit vector Hamiltonian $\hat{\mathbf{h}}$

$$\hat{\mathbf{h}} = \mathbf{h}/|\mathbf{h}| \tag{1.8}$$

is well defined. Under the simplification of having only two bands, the Chern number will index phases of $\hat{\mathbf{h}}$

$$\hat{\mathbf{h}} : T^2 \to S^2, \tag{1.9}$$

from the BZ to the Bloch sphere. The bands of $\hat{\mathbf{h}}$ correspond to a flattening of the bands pertaining to the original Hamiltonian. This adiabatic flattening preserves the gap and thus preserves the topology for the Hamiltonian [12]. This observation amounts to say that the target space of $\mathbf{h}$, i.e. $\mathbb{R}\backslash\{(0,0,0)\}$, is homotopic equivalent to S^2. Then $\hat{\mathbf{h}}$ can be thought of as a composition $\hat{\mathbf{h}} = \text{proj} \circ \mathbf{h}$, where

$$\text{proj} : \mathbb{R}^3\backslash\{(0,0,0)\} \to S^2 \tag{1.10}$$

is the central projection to the unit sphere.

All functions $\mathbf{h}$ that can be smoothly transformed into each other, while preserving the spectral gap, form a homotopy class. In $\mathbb{Z}$ insulators there is a integer index distinguishing the different phases (i.e. the different homotopy classes) of $\mathbf{h}$, the Chern number $\mathcal{C}$. A different way to express this idea is to say that the homotopy group of the mapping $\hat{\mathbf{h}}$ is the group of integers $\mathbb{Z}$. Without elaborating on these issues that go beyond the scope of the present section, it is noteworthy to point out that Chern numbers index mappings between d-spheres, here $S^2 \to S^2$, and the homotopy group is $\pi(S^d, S^d) \equiv \pi_d(S^d) = \mathbb{Z}$. However, the homotopy group of the torus is equivalent to that of the sphere,

$$\pi(T^2, S^2) = \pi_2(S^2) = \mathbb{Z}. \tag{1.11}$$

Then TKNN numbers used to index the integer Hall phases [17, 41] are indeed Chern numbers [42].

These considerations extend to the case of the n-band systems with nondegenerate bands where the topological invariant is given by a vector of Chern number of dimension $n-1$

$$\pi_2(Herm(n)) = \bigoplus_{i=1}^{n-1} \mathbb{Z}. \tag{1.12}$$

Each band has an associated invariant, such that the sum of Chern numbers for the entire system is zero. The $n-1$ dimension of the vector follows because the invariant for any one of the bands is entirely determined by the sum of the other invariants [42].

Chern number as a finite sum

Let us come back to the two-band case in order to find a workable formula for the topological invariant. The projector on the occupied band in terms of $\hat{\mathbf{h}}$ reads

$$P = \frac{1}{2}(\sigma_0 - \hat{\mathbf{h}} \cdot \boldsymbol{\sigma}). \tag{1.13}$$

The substitution of P in Eq. (1.4) yields immediately the expression for the first Chern number for the occupied band

$$\mathcal{C} = \frac{1}{4\pi} \int_{\mathrm{BZ}} d^2\mathbf{k}\, \hat{\mathbf{h}} \cdot (\partial_{k_x}\hat{\mathbf{h}} \times \partial_{k_y}\hat{\mathbf{h}}). \tag{1.14}$$

The above formula shows that the Chern number is a winding number that counts how many times does the surface traced by $\mathbf{h}$ wrap around the origin $(0,0,0)$ when $\mathbf{k}$ varies in the BZ [43]. The only practical difficulty in determining the Chern number lies in performing the integration in Eq. (1.14). The main point of this section is that $\mathcal{C}$ can be computed using a discrete summation by determining directly the Brouwer degree of the map $\hat{\mathbf{h}}$ [44, 45] (defined below).

The condition to calculate the degree of $\hat{\mathbf{h}}$ are met: T^2 and S^2 are orientable manifolds without boundary and have the same dimension, T^2 is compact and S^2 is connected. In the general case, for a point $\mathbf{k}$ in T^2 one defines the derivative map between tangent vector spaces

$$d\hat{\mathbf{h}}(\mathbf{k}) : T_{\mathbf{k}}T^2 \to T_z S^2. \tag{1.15}$$

Let sgn $d\hat{\mathbf{h}}(\mathbf{k})$ stand for the sign of the corresponding Jacobian at $\mathbf{k}$. Then Chern number $\mathcal{C}$ is equal to the Brouwer degree of $\hat{\mathbf{h}}$ at a regular point z on the unit sphere

$$\mathcal{C} = \sum_{\mathbf{k}\in\hat{\mathbf{h}}^{-1}(z)} \mathrm{sgn}\, d\hat{\mathbf{h}}(\mathbf{k}). \tag{1.16}$$

The Chern number can be computed also in terms of $\mathbf{h}$ in the following way. For convenience, let $\mathcal{M}$ denote the image of the BZ through $\mathbf{h}$

$$\mathbf{h}(T^2) = \mathcal{M} \subset \mathbb{R}^3 \backslash \{(0,0,0)\}. \tag{1.17}$$

Consider the set $Y = \mathcal{M} \cap \text{proj}^{-1}(z)$. Then one has

$$\mathcal{C} = \sum_{\mathbf{y} \in Y} \sum_{\mathbf{k} \in \mathbf{h}^{-1}(\mathbf{y})} \text{sgn}[(\partial_{k_x}\mathbf{h} \times \partial_{k_y}\mathbf{h}) \cdot \mathbf{n}], \tag{1.18}$$

where the $\mathbf{n}$ is the unit vector towards z. This expression is just the generalization of the calculation of the winding number for a closed curve in 2D wrapping around a point p [45, 46].

The formula in Eq. (1.18) can be further simplified by an appropriate choice of the point z. The central projection proj maps any intersection point between $\mathcal{M}$ and a ray originating at $(0,0,0)$ to z. If this ray does not cross the surface $\mathcal{M}$ traced by $\mathbf{h}$, then it follows that the surface does not wrap around the origin and the Chern number is zero. For a point z on S^2, one can immediately obtain a set of points on $\mathcal{M}$ that project to z through proj. Since the expression (1.16) does not depend on z, the choice of the latter can be guided by convenience. For instance, one can consider z lying at a coordinate axis. Let us choose for example the σ_3-axis which intersects $\mathcal{M}$ in a set of points. This is equivalent to say that the components on the other axes are zero. Said differently, the intersection of $\mathcal{M}$ with the σ_3-axis are images of the band touchings originating from the simplified Hamiltonian $\sigma_1 h_1 + \sigma_2 h_2$. Consequently, instead of integrating over the entire BZ, one only needs to consider the band touchings of the simplified Hamiltonian. Note that if h_3 is also zero at these points, then the system is not in a gapped phase.

It only remains to account for the orientation of the surface at the intersection points with σ_3-axis. This can be done by studying the projection of the surface normal vector on the σ_3-axis $(\partial_{k_x}\mathbf{h} \times \partial_{k_y}\mathbf{h})_3$. When $h_3 > 0$, assume that the orientation is $(+1)$ when the sign of the projection is positive and, (-1), when the sign is negative; the converse is true when $h_3 < 0$. Then finding the Chern number amounts to a computation of a finite sum. Since the entire σ_3-axis was considered, instead of a ray, the sum yields twice the value of the Chern number.

The above argument can be generalized and summarized in the following formula for Chern numbers describing 2-band systems

$$\mathcal{C} = \frac{1}{2} \sum_{\mathbf{k} \in \mathbf{D}_i} \text{sgn}\big(\partial_{k_x}\mathbf{h} \times \partial_{k_y}\mathbf{h}\big)_i \text{sgn}(h_i). \tag{1.19}$$

where i is an arbitrary axis chosen in (pseudo-)spin space. Therefore the integral over momenta $\mathbf{k}$ in the BZ becomes a finite sum over $\mathbf{k}$ in the set of Dirac points $\mathbf{D}_i$ for Hamiltonians $H[h_i = 0]$ (where H is the original Hamiltonian $\mathbf{h} \cdot \boldsymbol{\sigma}$). Note that division by two is required because the entire axis was considered, instead of a ray originating in $(0,0,0)$.

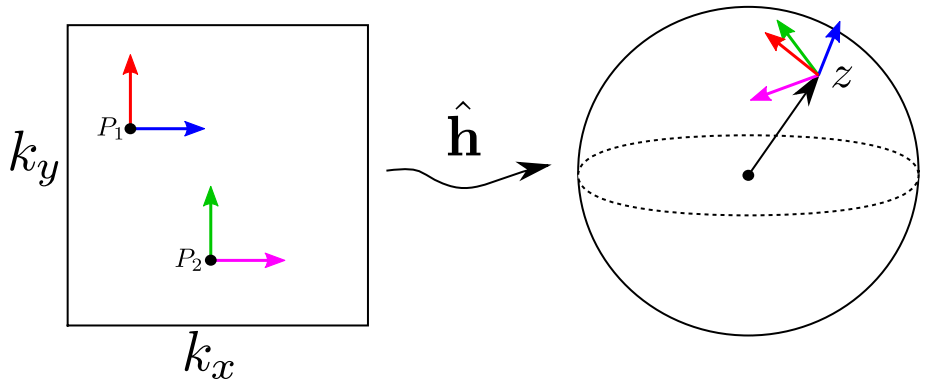

Fig. 1.1: An example of a discrete calculation of a Chern number. The topological invariant is calculated at single point z on the Bloch sphere. Here it has two preimage points on the BZ, P_1 and P_2. Under $\hat{\mathbf{h}}$, a basis at P_2 changes orientation when going to z. Then at z there are two topological charges canceling to give a zero Chern number.

Discussion

The topological invariant for an insulating system was connected to a simpler analysis for gapless two-band system that possess Dirac points. Once the Dirac points were identified, it is immediate to compute their chirality χ

$$\chi_i(\boldsymbol{\kappa}) = \mathrm{sgn}[\left(\partial_{k_x}\mathbf{h} \times \partial_{k_y}\mathbf{h}\right)_i]|_{\boldsymbol{\kappa}}. \tag{1.20}$$

The quantity χ indicates if the Berry phase gained by the wave function around the Dirac point is $\pm\pi$. Subsequently the system is gapped by h_i, which is the so called mass term. Then mass sign h_i and the chirality χ_i are sufficient to determine the Chern number $\mathcal{C}$ which indexes the insulating phase of the Hamiltonian. Note that due to the general arguments made above, there is no intrinsic meaning for the mass term and any component of $\mathbf{h}$ can play the mass role.

There is an important caveat to the above formula that needs to be addressed: it is not always true that preimage points for the intersections of axis with the Bloch sphere are Dirac points for the gapless systems. They can correspond to nonlinear band touchings such that the sign of the Jacobian at the band touching $\boldsymbol{\kappa}$ is not defined. This situation arises when the band touching is due to a merging of Dirac points. Then the first derivatives of $\mathbf{h}$ vanish, leading to $\chi = \mathrm{sgn}[0]$. Note that these cases correspond to a folding of the manifold $\mathcal{M}$ exactly on the spin axes (see Fig. 1.2). However the Eq. (1.19) remains useful. The first solution to maintaining its pertinence, is to choose a different axis in order to avoid the diabolical points where $\mathcal{M}$ folds. The second solution, which is illustrated in Sec. 1.4, consists in determining $\mathcal{C}$ from an analysis of chiralities pertaining to converging Dirac points. The idea rests on the fact that the merging solutions requires tuning the convergence of multiple Dirac points and it is generally unstable to perturbations. Then a small perturbation in the parameters of the Hamiltonian (a perturbation that does not cause a topological transition) splits the merging point into a set

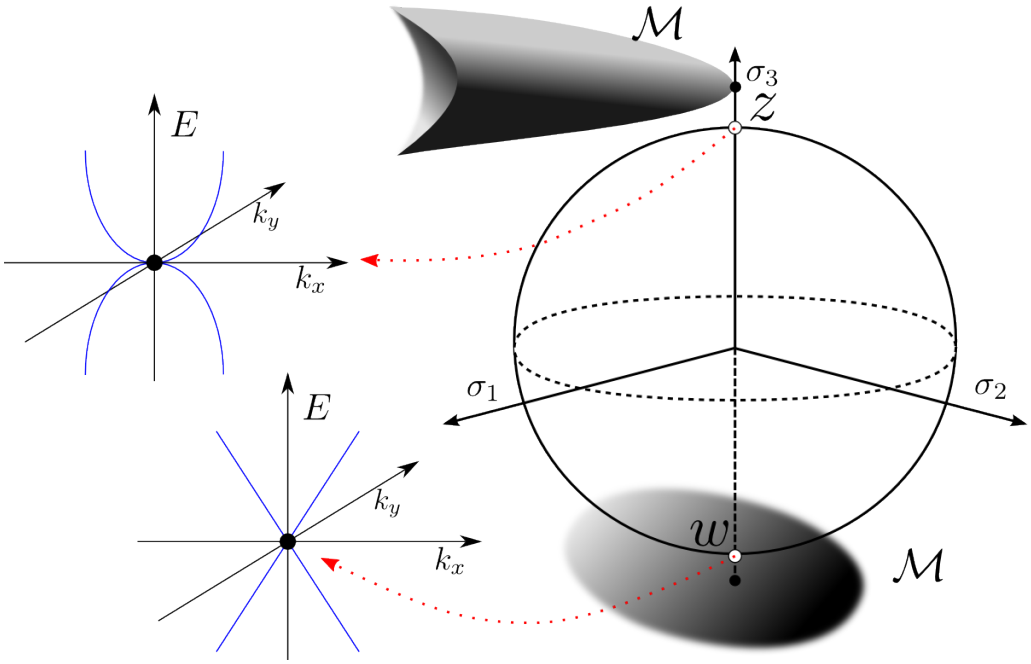

Fig. 1.2: Examples of situations that arise when computing the Chern number $\mathcal{C}$ as a finite sum. Here the privileged axis is σ_3 and therefore $h_1\sigma_1 + h_2\sigma_2$ is a gapless Hamiltonian. The surface traced by the full $\mathbf{h}$, $\mathcal{M}$, has a fold at σ_3-axis, such that the preimage of z gives a band touching with quadratic dispersion for the gapless model. This is an example of a diabolical point on the Bloch sphere that must be avoided in order to determine the insulating phases of the full model, using Eq. (1.19). At the other pole, there is the usual case of a well-behaved point w, that has a Dirac point as a preimage. When there are only Dirac points as preimages of z and w, the topological invariant is resolved as a sum over their chiralities using the finite sum formula.

of Dirac points. Furthermore, it was shown that the topological charge associated to a band touching with higher dispersion is conserved and equals the sum over the chiralities of the Dirac points [47, 48]. Then the diabolical points can be treated as limit cases for the same system close to the merging point and with multiple Dirac fermions.

Let us suppose for the moment that the privileged axis is σ_3 and the poles have only Dirac points as preimages in BZ. There are a few interesting consequences that ensue.

The sum over the chiralities of Dirac points is always zero. This is seen by adding a large constant mass term such that there is zero Chern number. Equivalently the Bloch sphere is translated on the σ_3 axis such that the origin $(0, 0, 0)$ is no longer included in the sphere. Then the sign of the mass can be factored out, and under the constraint $\mathcal{C} = 0$, the sum over chiralities must yield zero.

Also note that in order to get a nonzero Chern number, the mass term must change its sign at least once. This gives a meaning to the requirement of "inverted gap" in order to have nontrivial phases.

There is an equal number of Dirac fermions with $\chi = 1$ as those with $\chi = -1$, because the sum over chiralities is zero,. It follows that there is always an even number of Dirac fermions. This affirmation agrees with the predicted doubling of fermions on a lattice [49]. However, an odd number of Dirac fermions are permitted when the full Hamiltonian $\mathbf{h}$ is considered. This is the case at an interface between two $\mathbb{Z}$ insulators where the Chern number changes by an odd integer.

Finally, for a given model there is always a limit to the largest possible Chern phase and it manifestly depends on the minimum number of Dirac points. Let us suppose that the number is $2n$ because there is an even number of Dirac fermions ($n \in \mathbb{Z}$). Then the largest Chern number phase has $|\mathcal{C}| = n$ and it corresponds to gapping all Dirac fermions with a mass term that changes sign between the Dirac points. More precisely, the product between the chirality of a Dirac fermions and the sign of the mass that gaps must remain constant. This observation opens the road to the present chapter that essentially explores the notion of creating large Chern topological phases in model $\mathbb{Z}$ insulators in class A.

1.2.2 Examples

The efficiency of Eq. (1.19) to discriminate the topological phases is exemplified here on a couple of popular models of topological insulators: the Haldane model [23] and the Bernevig-Hughes-Zhang [5] (BHZ) "spin up" Hamiltonian for the HgTe/CdTe quantum wells. They will be treated at a formal level, only as an illustration of the technique.

Haldane model

Let us start by considering the paradigmatic Haldane model [23]. A more detailed analysis is undertaken in Sec. 1.4. Here suffices to observe that it can be seen as a modification on the graphene tight-binding system. The latter lives on a hexagonal lattice built out of two inter-penetrating triangular sub-lattices with A and B atoms. It is usually approximated as having only nearest-neighbor (NN) electron hopping with the hopping integral t_1. The Haldane model contains also next-nearest-neighbor (NNN) hopping t_2, such that when the hopping is performed clockwise in the unit cell the electron gains a phase ϕ. However, the overall phase on the unit cell is zero; there is no net magnetic flux. Let the vectors $(\mathbf{a}_1, \mathbf{a}_2, \mathbf{a}_3)$ describe the displacements from B atoms to NN A atoms and $\mathbf{b}_i = \frac{1}{2}\epsilon_{ijk}(\mathbf{a}_j - \mathbf{a}_k)$ vectors relating NNN sites (see Fig. 1.3). The time-reversal symmetry and particle-hole symmetry is broken by the presence of the flux ϕ. It also has an on-site energy $\pm M$ that has a sign alternating between the A and B sites. This term destroys the chiral symmetry of the lattice and therefore according to the classification of non-interacting, gapped, fermion systems, the Haldane model has insulating phases described by a Chern number.

The Bloch Hamiltonian reads

$$H(\mathbf{k}) = \sum_{i=1}^{3} \{2t_2 \cos(\phi) \cos(\mathbf{k}\cdot\mathbf{b_i})\sigma_0 + t_1[\cos(\mathbf{k}\cdot\mathbf{a_i})\sigma_1 + \sin(\mathbf{k}\cdot\mathbf{a_i})\sigma_2] + [\frac{M}{3} - 2t_2 \sin(\phi)\sin(\mathbf{k}\cdot\mathbf{b_i})]\sigma_3\}. \quad (1.21)$$

The term $\sigma_3 h_3$ is chosen as the mass term, and therefore the gapless submodel is the graphene Hamiltonian ($M \to 0$ and $t_2 \to 0$). The Dirac points in graphene are positioned at time-reversed points $\mathbf{K}$ and $\mathbf{K}' = -\mathbf{K}$ on BZ, where $\mathbf{K} = \left(\frac{4\pi}{3\sqrt{3}}, 0\right)$. The chirality of the Dirac points is readily determined from Eq. (1.20)

$$\chi(\pm\mathbf{K}) = \pm 1. \quad (1.22)$$

In order to calculate the Chern number, one must also consider the mass sign at the Dirac points, $\mathcal{M}_\pm := h_3(\pm\mathbf{K})$,

$$\mathcal{M}_\pm = M \mp 3\sqrt{3}t_2 \sin(\phi). \quad (1.23)$$

Therefore, using Eq. (1.19) one recovers Haldane result for the Chern number

$$\mathcal{C} = \frac{1}{2}(\mathrm{sgn}\mathcal{M}_- - \mathrm{sgn}\mathcal{M}_+). \quad (1.24)$$

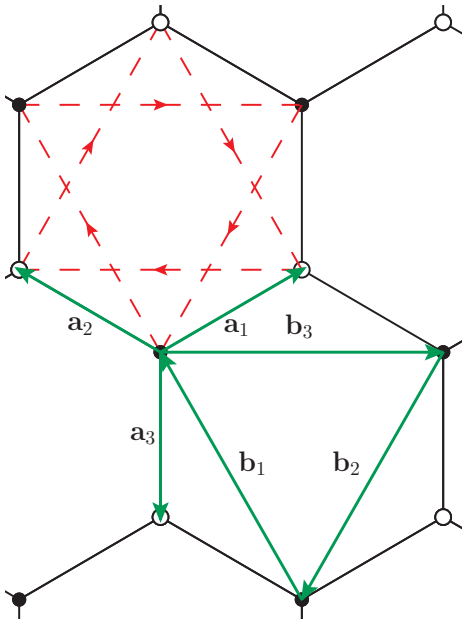

Fig. 1.3: Schematic representation of the Haldane model. The A (B) sites are represented by white (black) bullets, ∘ (•). Along the dashed lines an electron gains a phase ϕ in the direction of the red arrows. The vectors $\mathbf{a}$ and $\mathbf{b}$ are the NN and, respectively, NNN displacement vectors.

The transition from a topological insulator to a normal insulator is marked by a semi-metal state, where the gap closes at least at one Dirac point when $M = \pm 3\sqrt{3}t_2 \sin(\phi)$. In the normal insulating phase Dirac points have identical associated mass sign, such that $\mathcal{C}$ vanishes.

BHZ model

The Chern number calculation can be exemplified in the case of the recently discovered $\mathbb{Z}_2$ insulators such as the 2D HgTe/CdTe quantum wells [5]. The low energy Bloch Hamiltonian is written in a basis of four states $|E1, m_J = 1/2\rangle$, $|H1, m_J = 3/2\rangle$, $|E1, m_J = -1/2\rangle$, $|H1, m_J = -3/2\rangle$ and it has the form

$$\tilde{H} = \begin{pmatrix} H(\mathbf{k}) & 0 \\ 0 & H^*(-\mathbf{k}) \end{pmatrix}. \quad (1.25)$$

Dirac points	(0,0)	$(\pi,0)$	$(0,\pi)$	(π,π)	$\mathcal{C}$
mass h_3	M	$M-4B$	$M-4B$	$M-8B$	
chirality	$+$	$-$	$-$	$+$	
$M<0$	$-$	$+$	$+$	$-$	0
$M\in(0,4B)$	$+$	$+$	$+$	$-$	$+$
$M\in(4B,8B)$	$+$	$-$	$-$	$-$	$-$
$M>8B$	$+$	$-$	$-$	$+$	0

Table 1.1: Chern phases for a "spin-up" BHZ model as a function of system parameters, with $B>0$.

The system respects time reversal symmetry and realizes a $\mathbb{Z}_2$ topological insulator. However it is assembled out of two Chern insulators: $H(\mathbf{k})$ and its time reversed copy, indexed by $\mathcal{C}$ and $-\mathcal{C}$. If there are no interblock matrix elements, the topological invariant can be determined as a *spin Chern number*, expressed as $\mathcal{C}$ mod 2 [50].

Therefore it is enough to pick one Chern insulator, and illustrate the computation of $\mathcal{C}[H(\mathbf{k})]$.

$$H(\mathbf{k})=A\sin(k_x)\sigma_1+A\sin(k_y)\sigma_2+[M-2B(2-\cos(k_x)-\cos(k_y))]\sigma_3, \tag{1.26}$$

where A,B,M are material parameters. Let us consider again the surface traced by $\mathbf{h}$ and choose σ_3 as a special axis. The points where the σ_3-axis pierces the surface are given by the condition that h_1 and h_2 vanish simultaneously. That determines four "Dirac points" $(q_x,q_y)\in\{(0,0),(0,\pi),(\pi,0),(\pi,\pi)\}$.

The chirality of each Dirac point is given by Eq. (1.20)

$$\chi(\mathbf{q})=\mathrm{sgn}[\cos(q_x)\cos(q_y)] \tag{1.27}$$

evaluated at all Dirac points. The mass term h_3 has the following expression at the Dirac points, $h_3(0,0)=M$, $h_3(0,\pi)=h_3(\pi,0)=M-2B$ and $h_3(\pi,\pi)=M-4B$.

The Chern number can then be easily computed for different values of M and B by summing over the Dirac points. The results for the case $B>0$ are summarized in Tab. 1.1.

From Tab. 1.1 it follows that as M varies between 0 and $8B$, the Chern insulator $H(\mathbf{k})$ exhibits two topologically nontrivial phases with $\mathcal{C}=\pm1$. When M is outside the $(0,8B)$ region there is only a trivial insulator phase. Therefore nontrivial Chern phases will yield also nontrivial $\mathbb{Z}_2$ (QSH) phases.

1.3 Model building of a topological insulator with large Chern phases

1.3.1 General discussion

The objective of the present section is to explore in more detail the question of how to imagine two-band topological insulators with high Chern number. It is argued that understanding the topological invariant as a finite sum in addition to the symmetry constraints is sufficient to produce Hamiltonians with large Chern phases. In particular, following theoretical considerations, a simple model which can be tuned through five insulating phases, $\mathcal{C} \in \{0, \pm 1, \pm 2\}$ is produced step by step.

Note that when more than two bands are allowed, high Chern phases can ensue readily by having each occupied band contributing to the overall conductance. This is indeed the case of the integer quantum Hall effect where the larges Hall conductance is given by the number of bands. However the question posed here is how to create a *single* band with a high Chern number. Arguably, there is a gain in theoretical control of this situation, with all the insulating phases determined analytically.

The answer to the central question was already mentioned briefly in the previous section. It comes down to the way a $\mathbb{Z}$ insulator was understood by decomposing it into a gapless model with Dirac fermions and a mass term that gaps them [38].

For a system with translation symmetry, the application of Bloch theorem allows to write a general Hamiltonian in $\mathbf{k}$-space

$$H = \mathbf{h} \cdot \boldsymbol{\sigma}, \tag{1.28}$$

where the identity $h_0\sigma_0$ was dropped out because it does not weigh on the topological properties of the model. The Pauli matrices represent a pseudo-spin degree of freedom due to the presence of two orbitals on a site or two sites in the unit cell.

To fix ideas, the $h_3(\mathbf{k})\sigma_3$ is chosen as the mass term throughout the section. Hence the gapless model H_{12} reads

$$H_{12} = h_1(\mathbf{k})\sigma_1 + h_2(\mathbf{k})\sigma_2. \tag{1.29}$$

The Chern number from Eq. (1.19) reads

$$\mathcal{C} = \frac{1}{2} \sum_{\mathbf{k} \in \ker H_{12}} \operatorname{sgn}\big(\partial_{k_x}\mathbf{h} \times \partial_{k_y}\mathbf{h}\big)_3 \operatorname{sgn}(h_3). \tag{1.30}$$

The kernel of H_{12} contains all the values of $\mathbf{k}$ for which h_1 and h_2 vanish simultaneously. They are band touchings of the the gapless model H_{12} and, in general, they are Dirac points with chirality given by $\chi = \operatorname{sgn}\big(\partial_{k_x}\mathbf{h} \times \partial_{k_y}\mathbf{h}\big)_3$.

Then a necessary condition to obtain a Chern insulator with large Chern phases is to create multiple Dirac points. The largest Chern phase can be obtained by tuning a

mass term such that the product of the chirality and the gapping term is constant for all Dirac points. Therefore, if there are $2n$ Dirac points the largest Chern number is n.

Because $\mathbf{h}$ is periodic on BZ, the components h_i can be Fourier analyzed to give

$$h_i(\mathbf{k}) = c_{00}^{(i)} + \sum_{m,n} c_{m,n}^{(i)} \cos(\mathbf{k}\cdot(m\mathbf{a}_1 + n\mathbf{a}_2)) + \sum_{m,n} s_{m,n}^{(i)} \sin(\mathbf{k}\cdot(m\mathbf{a}_1 + n\mathbf{a}_2)), \quad (1.31)$$

where m and n are integers and never both equal to zero. The vectors $\mathbf{a}_1$ and $\mathbf{a}_2$ are the Bravais lattice vectors are . Adding coefficients s and c corresponds to adding hopping terms between orbitals. Then multiplying the Dirac points for H_{12} requires producing distant-neighbor hopping terms which contain sinusoidal components that oscillate faster and faster as m and n grow. That results in an energy dispersion which acquires more nodes when distant-neighbor hoppings are included.

The requirement of distant-neighbor hopping terms to produce large Chern phases poses a problem from a physical point of view. The wave functions in the tight-binding model are localized and presence of distant-neighbor interaction can be usually neglected. However it was already shown that low-energy models of multi-band system can be mapped to two-band systems with large Chern number [37]. Regardless of the physical realization, the inclusion of higher harmonics (or distant-neighbor hopping terms) is the unavoidable requirement to producing a large topological invariant.

To complete the discussion it is necessary to examine the symmetries, or lack thereof, for the $\mathbb{Z}$ topological insulator in two dimensions. In order to have a Chern insulator in class A it is necessary to break the time reversal, the particle-hole and the chiral (or sublattice) symmetries (see Tab. 1).

The symmetries can impose gneral constraints on the components of $\mathbf{h}$ to the effect of a vanishing Chern number. For example, the TRS and the PHS are represented by anti-unitary operators that will relate opposite momenta on the BZ. Therefore they will impose parity constraints on the components of $\mathbf{h}$. A rule of thumb to eliminate these symmetries is to mix odd and even functions in an arbitrary component of $\mathbf{h}$. The sublattice symmetry is represented by an unitary Hermitian operator $\mathfrak{S}$ and it is broken by adding hopping terms between the equivalent sites (orbitals). This corresponds to destroying the bipartite nature of the system [51].

Let us elaborate on the example of the TRS. For spinless electron models considered here, the time-reversal operator does not act on orbital or site space an hence it is simply the complex conjugation K required to reverse the momentum direction. Demanding time-reversal invariance and Hermiticity yields

$$\begin{aligned} h_1(\mathbf{k}) &= h_1(-\mathbf{k}), \\ h_2(\mathbf{k}) &= -h_2(-\mathbf{k}), \\ h_3(\mathbf{k}) &= h_3(-\mathbf{k}). \end{aligned} \quad (1.32)$$

Hence in a TRI system the Chern number vanishes because the integrand in equation (1.14) is an odd function of $\mathbf{k}$,

$$\hat{\mathbf{h}}\cdot(\partial_{k_x}\hat{\mathbf{h}} \times \partial_{k_y}\hat{\mathbf{h}}) = 0. \quad (1.33)$$

Generally, if a symmetry imposes that either exactly one of the components of $\mathbf{h}$ is an odd function, or that all components are odd, then the Chern vanishes under the same argument as above. The PHS will not be of concern in the following because by construction there are no superconducting pairing terms.

1.3.2 A model with five Chern phases

The objective is to create a toy model of a spinless Chern insulator with $|\mathcal{C}| = 2$. It is shown here that the model can be created with at most nearest-neighbor hopping terms. Such a model serves as a proof of principle for the form of an insulator with a large Chern number and it will be of use later, when the interest shifts to the investigation of edge solutions in a $\mathbb{Z}$ insulator.

First a gapless model with four Dirac points is proposed as a prerequisite. Secondly, the Dirac points are gapped by a mass term that can be locally tuned so that the Hamiltonian passes through all possible Chern phases $\{0, \pm 1, \pm 2\}$. The geometrical engineering of the insulators takes place in momentum space. At the end of the section, a real-space implementation of the model on a triangular lattice is discussed.

Topological phases for momentum space Hamiltonian

Let us start with the gapless model that serves as a template for the construction of the insulator. To have $|\mathcal{C}| = 2$, it is necessary to have four Dirac points. One of the most simple model has only NN hopping ($m < 1$ or $n < 1$) in the Fourier series (1.31). Choosing even functions $\mathbf{h}_1$ and $\mathbf{h}_2$, it follows that

$$\begin{aligned} H_{12} &= h_1(\mathbf{k})\sigma_1 + h_2(\mathbf{k})\sigma_2 \\ &= 2t_1[\cos(k_x)\sigma_1 + \cos(k_y)\sigma_2]. \end{aligned} \tag{1.34}$$

The energy dispersion reads

$$E = \pm 2t_1\sqrt{\cos^2(k_x) + \cos^2(k_y)}, \tag{1.35}$$

with four Dirac points at $\mathbf{q} = (\pm\pi/2, \pm\pi/2)$.

Note that to have time reversal invariance in a spinless model, h_2 must be an odd function. Hence the choice $\cos(k_y)$ ensures that the TRS is broken.

The chirality coresponding to Dirac points is given by the sign of the Jacobian

$$\chi(\mathbf{q}) = \mathrm{sgn}[\sin(q_x)\sin(q_y)]. \tag{1.36}$$

This determines the chirality χ of the four Dirac points as summarized in Tab. 1.2.

Note that the points at $\mathbf{q}$ and $-\mathbf{q}$ have the same chirality. They will be referred in the following as a pair of Dirac points.

To obtain a Chern insulator one needs to add a mass term. As one can see from Eq. (1.30), the Chern index depends on both the chiralities of the Dirac points and the sign

Dirac points	$(\frac{\pi}{2}, \frac{\pi}{2})$	$(\frac{\pi}{2}, -\frac{\pi}{2})$	$(-\frac{\pi}{2}, \frac{\pi}{2})$	$(-\frac{\pi}{2}, -\frac{\pi}{2})$
χ	+	−	−	+

Table 1.2: Chirality χ of the four different Dirac points.

of the mass term in their vicinity. Let us add a mass term of the form $h_3(\mathbf{q})\sigma_3$. Since h_3 is a periodic function on the BZ, in the general case, its zeros form a set of closed lines on the two-dimensional torus. The first condition in order to gap the initial system is that these lines must not pass through the Dirac points. Thus the lines of zeros delimit regions, $\mathcal{R}_1$ and $\mathcal{R}_2$, where the mass term has the same sign. For a proper choice of the gap term, it is somewhat simpler to see the problem from a geometrical point of view. In order to maximize $|\mathcal{C}|$, one needs that the lines of zeros separate the *pairs* of Dirac points such that a pair of points of a given chirality are contained in a region of positive mass, while pair of points of opposite chirality are contained in a region of negative mass region. In short, each *pair* of Dirac points are placed in regions where the mass term has different values. On the contrary, if a pair of Dirac points is "broken" (such that one is in region $\mathcal{R}_1$ and the other in region $\mathcal{R}_2$), then the topological charges will cancel out as can be directly inferred from Eq. (1.30).

Let us first realize topological phases with $C = \pm 2$, where each pair of Dirac points is in a different region $\mathcal{R}$. The chirality is an even function; hence keeping the product of chirality and mass sign constant is accomplished by an even function h_3. A simple solution is the periodic function

$$h_3 \propto \cos(k_x + k_y) \tag{1.37}$$

with lines of zeros given by $k_y = -k_x + \frac{2n+1}{2}\pi$. The regions $\mathcal{R}_1$ and $\mathcal{R}_2$ for this term are represented in Fig. 1.4(a). The mass term is negative in region $\mathcal{R}_1$ and positive in region $\mathcal{R}_2$. The lowest Chern number $\mathcal{C} = -2$ is obtained for this model. Let us consider that the term corresponds to a hopping term with an amplitude t_2. Hence, the insulating Hamiltonian with $|\mathcal{C}| = 2$ reads

$$H^{(1)}(\mathbf{k}) = 2t_1 \cos(k_x)\sigma_1 + 2t_1 \cos(k_y)\sigma_2 + 2t_2 \cos(k_x + k_y)\sigma_3. \tag{1.38}$$

The Chern number is readily determined

$$\mathcal{C}^{(1)} = -2\text{sgn}[t_2]. \tag{1.39}$$

Intuitively this is understood as a double covering of the Bloch sphere by $\mathbf{h}^{(1)}$ due to the fact that $\cos(k_x + k_y)$ has twice the frequency of $\cos(k_{x,y})$.

The Hamiltonian in Eq. (1.38) lacks trivial insulating phases or Chern phases with $\mathcal{C} = \pm 1$. To produce a trivial phase with $\mathcal{C} = 0$, it suffices to add a large, "staggered potential" $m\sigma_3$, such that all Dirac points are gapped identically. Then because the sum over chiralities is zero, $\mathcal{C}$ vanishes. Note that since Pauli matrices can act on any degree

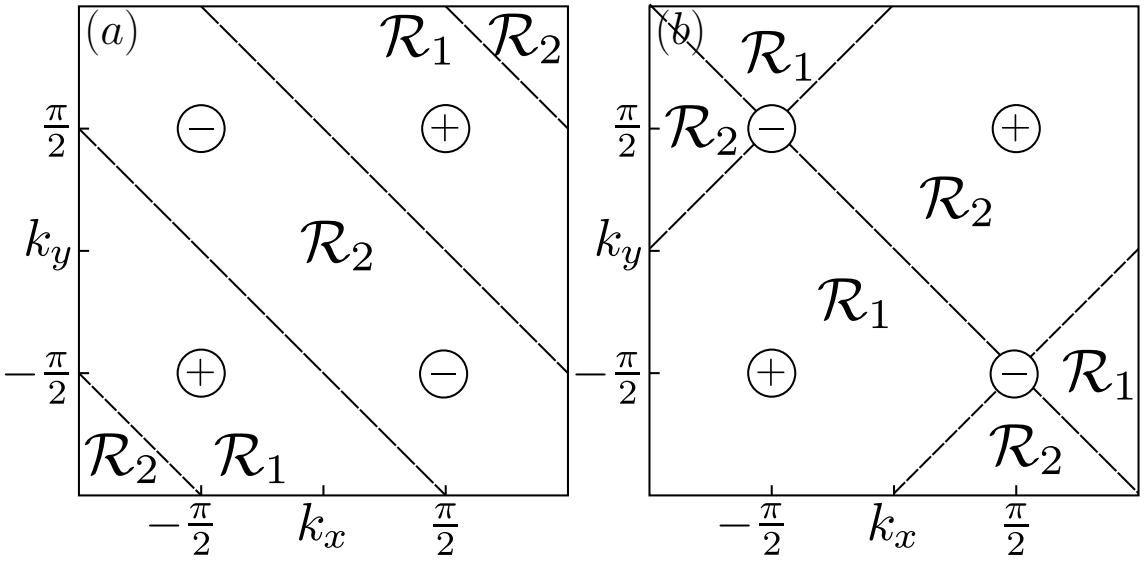

Fig. 1.4: Different mass terms, h_3, gap differently the Dirac points on the BZ to the effect of changing the Chern number. The solid circles represent Dirac points of the initial gapless system; the corresponding chiralities are marked by the signs within. Dashed lines are the zeroes of the mass term, while $\mathcal{R}_1$ and $\mathcal{R}_2$ denote regions with opposite sign for the mass term. (a) $h_3 = \cos(k_x + k_y)$. The mass term changes its sign an odd number of times between Dirac points of different chirality, therefore $\mathcal{C} = \pm 2$. (b) $h_3 = \sin(k_x) + \sin(k_y)$. Phases with $C = \pm 1$ are possible after the remaining Dirac points, $\ominus$, are identically gapped.

of freedom, the term "staggered" could for instance refer to the fact that two sites in a cell or two orbitals on a site have an associated $\pm m$ constant energy.

Therefore the Hamiltonian changes from $H^{(1)}$ to $H^{(2)} = H^{(1)} + m\sigma_3$, and, consequently, the Chern number becomes

$$\mathcal{C}^{(2)} = \text{sgn}[-m - 2t_2] + \text{sgn}[m - 2t_2]. \tag{1.40}$$

Hence, for a large energy m, $|m| > 2|t_2|$, the system enters a trivial phase and a transition between a $\mathcal{C} = \pm 2$ phase to a $\mathcal{C} = 0$ phase takes place.

To create Chern phases with $\mathcal{C} = \pm 1$, it is necessary to gap, with the same gap sign, a pair of Dirac points, while a second pair has its respective mass changing sign between the Dirac points. Because the chirality is an even function, the mass term has to be an odd function in order to get an odd function for the product between chirality and mass sign. The simplest choice would be to add the term proportional to $\sin(k_x) + \sin(k_y)$. The mass for one pair of Dirac points is unchanged, while, for the pair $(\mathbf{q}, -\mathbf{q})$ with $\mathbf{q} = (\pi/2, \pi/2)$, the mass changes. If only $\sin(k_x) + \sin(k_y)$ is present in the mass term, then the system is not an insulator, because there are band touchings at $\mathbf{q} = \pm(\pi/2, -\pi/2)$ (see Fig. 1.4(b)). However adding small even functions in the mass gaps identically these Dirac points and $\mathcal{C} = \pm 1$ phases follow.

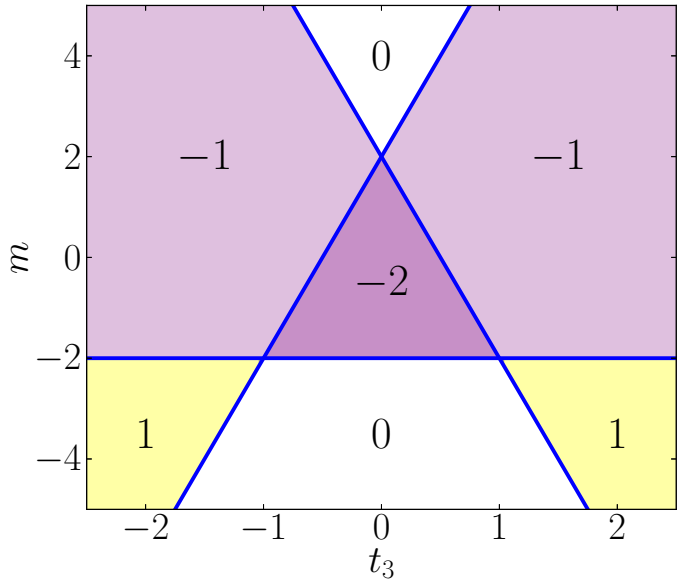

Fig. 1.5: Phase diagram of the system for $t_2 = 1$. Each region is denoted by the corresponding Chern number and represents an insulating topological phase. The boundaries of the regions represent topological transitions where the system becomes gapless.

Adding all terms together gives the following complete Bloch Hamiltonian for a model that has Chern phases in the set $\{0, \pm 1, \pm 2\}$

$$H = 2t_1 \cos(k_x)\sigma_1 + 2t_1 \cos(k_y)\sigma_2 + [m + 2t_2 \cos(k_x + k_y) + 2t_3(\sin(k_x) + \sin(k_y))]\sigma_3. \tag{1.41}$$

There are four free parameters (m, t_1, t_2, t_3) in the model. Let us assume that all parameters are real. All the phases can be reached by varying (m, t_2, t_3) while keeping t_1 fixed. The Chern number for the final model reads

$$\mathcal{C} = \text{sgn}(-m - 2t_2) + \frac{1}{2}[\text{sgn}(m - 2t_2 + 4t_3) + \text{sgn}(m - 2t_2 - 4t_3)]. \tag{1.42}$$

The expression for $\mathcal{C}$ yields immediately the phase diagram associated with the system described by the Hamiltonian in Eq. (1.41). Note that the parameter t_1 does not enter in the determination of the phases, but manifestly needs to be finite in order to have non-vanishing σ_1 and σ_2 components in the model. The formula (1.42) can be illustrated by the phase diagram in the Fig. (1.5). This diagram contains only four phases of the model; the phase with $\mathcal{C} = 2$ needs $t_2 < 0$.

Direct space realization

Until now the system was described abstractly in momentum space. However it will be of future interest to investigate the structure of its edge and therefore it is necessary to propose a lattice implementation for the model.

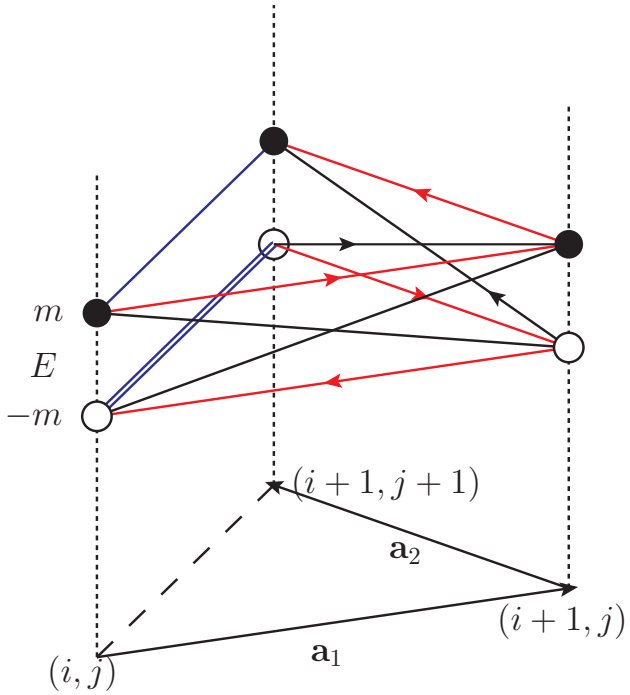

Fig. 1.6: Direct space realization of the model (1.41), see Eq. (1.43). (i,j) denotes lattice sites. The Bravais lattice vectors are denoted by $\mathbf{a}_{1/2}$, and $\bullet$ ($\circ$) represents orbitals with energy m ($-m$). The vertical axis represents the on-site energy difference between the two nonequivalent orbitals. Black lines represent t_1 hoppings, blue lines, t_2 hoppings, and red lines, t_3 hoppings. An arrow on a link indicates that an electron hopping in the corresponding direction gains a $\pi/2$ phase. Similarly a double line indicates a π phase gain.

The system could be realized on a triangular lattice with two orbitals on each site. The parameters are interpreted as $k_{x,y} = \mathbf{k} \cdot \mathbf{a}_{1,2}$ with $\mathbf{a}_1$ and $\mathbf{a}_2$, the two Bravais vectors. Then the Pauli matrices are operating in the space of two orbitals A and B with energy $\pm m$.

The Hamiltonian (1.41) can be rewritten in direct space

$$H = \sum_{ij} \Big[c_{ij}^\dagger \frac{m}{2} \sigma_3 c_{ij} + c_{i+1j}^\dagger (t_1\sigma_1 + it_3\sigma_3) c_{ij} + c_{ij+1}^\dagger (t_1\sigma_2 + it_3\sigma_3) c_{ij} + c_{i+1j+1}^\dagger t_2 \sigma_3 c_{ij} + \text{H.c.} \Big], \tag{1.43}$$

where the Fourier transformation for the annihilation operator reads

$$c_{\mathbf{k}} = \frac{1}{\sqrt{N}} \sum_{\mathbf{r}_{ij}} c_{ij} e^{-i\mathbf{k}\cdot\mathbf{r}_{ij}}. \tag{1.44}$$

The position of sites on the lattice is given by $\mathbf{r}_{ij} = i\mathbf{a}_1 + j\mathbf{a}_2$, with $\mathbf{a}_1$ and $\mathbf{a}_2$ as Bravais vectors making an angle $2\pi/3$ between them (see Fig (1.6)). The lattice constant was set to one, $a = 1$.

The model is represented in Fig. 1.6. On each site there are two different orbitals with energy $\pm m$. The Hamiltonian (1.43) describes through t-terms the overlap between (non)equivalent orbitals.

Note that there is no net flux perpendicular to the two dimensional plane. But the TRS is broken, because for certain closed paths involving the hopping term $t_1\sigma_2$, for the electron moving between two nonequivalent orbitals there is a gain of a phase $\pm\pi/2$. However for each path with a phase gain of $\pi/2$ there is one with $-\pi/2$ and therefore there is no net magnetic flux over the entire cell. Such a system realizes a IQHE in the absence of absence of an external magnetic field. Therefore it realizes a Chern insulator in the same class with the Haldane model [23].

1.4 Large Chern phases in the Haldane model

The first theorized Chern insulator is the Haldane model. It consists of a simple tight-binding model for spinless electrons on a hexagonal lattice.

The model can be understood as an underlying NN (nearest-neighbor) graphene with additional mass terms that gap the system. First there is an on-site energy $\pm M$ on the two nonequivalent atoms in the unit cell, A and B. This term breaks inversion symmetry and creates a gap. Secondly, there are N2 (next-nearest-neighbor) hoppings where an electron gains a phase ϕ. This term breaks TRS and is also called the Haldane mass term. The Hamiltonian of the system reads

$$H = \sum_m M_m c_m^\dagger c_m + \sum_{\langle m,n\rangle} t_1 c_m^\dagger c_n + \sum_{\langle\langle m,n\rangle\rangle} e^{i\phi_{mn}} t_2 c_m^\dagger c_n. \tag{1.45}$$

The sum runs over all the sites on the hexagonal lattice, and $\langle \ldots \rangle$ represent nearest neighbors and $\langle\langle \ldots \rangle\rangle$ next-nearest neighbors. The hopping integrals are denoted by t_j. The index of the hopping integral signifies the order of the (non)equivalent neighbors. The phase for a clockwise hopping from n to m is $\phi_{mn} = \phi$ and, $-\phi$, for anticlockwise hopping. The on-site energy is $M_m = M$, when m denotes an A atom, and $-M$, in case of a B atom.

Due to the mass terms (M and t_2), the system is generally a band insulator. Note that throughout the chapter, a system is considered an insulator if its bands can be flattened such that the Fermi surface rests in the gap (and not as usually, i.e. if the Fermi energy is between the conductance and valence band). The essential feature of the model rests in the fact that there is no net magnetic flux per unit cell. Therefore such a model can be envisaged in zero external magnetic field. However, one can find paths in real space where the electron gains a phase.

Even though there is no net magnetic field, Haldane showed that there are Chern numbers that index the insulating phases of the Hamiltonian. When the system is implemented on a finite geometry, there will be charge transported on the edge channels. More precisely there will be a quantized conductance that is proportional to the Chern number $\mathcal{C}$. The conductivity is given similarly to the integer quantum Hall effect by $\sigma_H = e^2/h \times \mathcal{C}$. In this way, the model is a realization of a Hall effect without an external magnetic field.

Although it was only a theoretical model, its importance for the evolution of the subject of topological insulators cannot be understated. The first proposal for QSHE in graphene is inspired directly from the Haldane model [4, 52]. The spin-orbit interaction opens a gap in graphene and each spin realizes a copy Haldane with opposite Chern number. Therefore it was predicted that the gapped graphene could host chiral and spin resolved edge states.

Returning from QSH insulator to the original Haldane model, note that the maximum Chern number is $|\mathcal{C}| = 1$, and thus there can be at most one edge state. In contrast,

in the IQHE, one can increase the number of edge states by filling more Landau levels. Then a natural way to increase the edge conductance in the Haldane model, would be to create a multi-band system from a stack of two dimensional Haldane models, such that the edge states of every layer have the same chirality.

However, there is an alternative route to augment the number of possible edge channels. The system can be decomposed in a gapless model and a mass term. Generally the band touchings of the gapless model are Dirac fermions. Then a necessary condition to have a Chern number $|\mathcal{C}| = n$ is to have $2n$ Dirac points. The Chern number will be determined entirely from the chirality of the Dirac fermions and the sign of the mass term that gaps them.

The Haldane model is a particularly interesting platform on which to test this idea because it is decomposed in an underlying graphene model and a mass term that contains the phase ϕ dependence.

First subsection focuses on the study of a graphene-like model with distant-neighbor-hopping integrals included. The solution for all Dirac points are studied up to N7 (next$\times$6-nearest-neighbor-hopping) graphene. Their evolution in parameter space has particular points that are called super-mergings where all Dirac points meet to create a band touching with higher than linear dispersion relation. These are unstable points that are characterized however by a small topological charge.

Second subsection considers gapping the Dirac fermions by the mass term. This will have the effect of creating topological insulating phases with large Chern number. It is equivalent to say that more edge channels can be created for the finite system. At the topological transitions between the phases the system becomes metallic and the exchange in Chern number can be seen in the number of Dirac fermions that are formed.[53]

1.4.1 Distant-neighbor hopping in graphene

To analyze the topological properties of the model it is advantageous to go in momentum space where the topological index is readily defined. The two-band Bloch Hamiltonian is developed in a basis of Pauli matrices σ in the AB site space

$$H = \sum_{\mu=0}^{3} h_\mu \sigma_\mu. \tag{1.46}$$

For addressing the topological properties, one can throw away the term $h_0\sigma_0$ that breaks particle-hole symmetry and shifts (topologically) trivially the bands. Let us also choose the Bravais lattice vectors $\mathbf{a}_1$ and $\mathbf{a}_2$, with $\mathbf{a}_1 = \big(\frac{\sqrt{3}}{2}, \frac{3}{2}\big)a$ and $\mathbf{a}_2 = \big(-\frac{\sqrt{3}}{2}, \frac{3}{2}\big)a$; a is the lattice constant and it is set to one in the following. Then the Hamiltonian reads

$$\begin{aligned} H = {} & t_1[1 + \cos(\mathbf{k}\cdot\mathbf{a}_1) + \cos(\mathbf{k}\cdot\mathbf{a}_2)]\sigma_1 + t_1[\sin(\mathbf{k}\cdot\mathbf{a}_1) + \sin(\mathbf{k}\cdot\mathbf{a}_2)]\sigma_2 \\ & + [M - 2t_2\sin\phi[\sin(\mathbf{k}\cdot\mathbf{a}_2) - \sin(\mathbf{k}\cdot\mathbf{a}_1) + \sin(\mathbf{k}\cdot(\mathbf{a}_1 - \mathbf{a}_2))]\sigma_3. \end{aligned} \tag{1.47}$$

hopping	physical distance	chemical distance	neighbors	g_n
t_1	1	1	3	$1+e^{-i\mathbf{k}\cdot\mathbf{a}_1}+e^{-i\mathbf{k}\cdot\mathbf{a}_2}$
t_3	2	2	3	$2\cos(\mathbf{a}_1-\mathbf{a}_2)+e^{-i\mathbf{k}\cdot(\mathbf{a}_1+\mathbf{a}_2)}$
t_4	$\sqrt{7}$	2	6	$e^{i\mathbf{k}\cdot\mathbf{a}_1}+e^{i\mathbf{k}\cdot\mathbf{a}_2}+e^{-2i\mathbf{k}\cdot\mathbf{a}_1}+e^{-2i\mathbf{k}\cdot\mathbf{a}_2}+e^{i\mathbf{k}\cdot(\mathbf{a}_1-2\mathbf{a}_2)}+e^{i\mathbf{k}\cdot(\mathbf{a}_2-2\mathbf{a}_1)}$
t_7	$\sqrt{13}$	3	6	$\cos(2\mathbf{k}\cdot(\mathbf{a}_1-\mathbf{a}_2))+e^{-i\mathbf{k}\cdot\mathbf{a}_1}\cos(2\mathbf{k}\cdot\mathbf{a}_2)+e^{-i\mathbf{k}\cdot\mathbf{a}_2}\cos(2\mathbf{k}\cdot\mathbf{a}_1)$

Table 1.3: Hopping terms between AB atoms. The physical distance is counted in units of lattice constant a. The chemical distance is the smallest number of bonds passed when hopping between two sites. In the column "neighbors" it is counted the number of sites situated at the same physical distance from the central site.

The underlying graphene-like model contains only the $h_1(\mathbf{k})$ and $h_2(\mathbf{k})$ terms. The Dirac points of the model are obtained from the zeros of the function $f(\mathbf{k}) = h_1(\mathbf{k})\sigma_1 - ih_2(\mathbf{k})\sigma_2$. The Dirac points are positioned in the BZ at $\mathbf{K}^{(\prime)} = (\pm\frac{4\pi}{3\sqrt{3}}, 0)$. The interest is to keep the system two-band and to simultaneously increase the number of Dirac points. The claim is that this can be realized by including distant-neighbor-hopping terms.

Let us generalize the graphene model by including Nn (next$\times(n-1)$ nearest neighbor) hopping terms. The AA and BB terms will contribute only to the identity term $h_0\sigma_0$. Because they will not have an impact on the topological index, they are dropped out from the Hamiltonian. By contrast, the hopping between different sites, AB, contributes to $h_1(\mathbf{k})$ and $h_2(\mathbf{k})$ terms.

The Hamiltonian reads

$$H = \begin{pmatrix} 0 & f(\mathbf{k}) \\ f^*(\mathbf{k}) & 0 \end{pmatrix} \tag{1.48}$$

with

$$f(\mathbf{k}) = \sum_n t_n g_n(\mathbf{k}). \tag{1.49}$$

The contributions g_n from the distant-neighbor hoppings are tabulated to first orders in Tab. 1.3. Here are treated cases up to N7 graphene for which one can obtain fairly straightforward analytical solutions for the Dirac points. Therefore the only hopping terms that appear in f are t_1, t_3, t_4 and t_7. In the following the hopping integrals are considered in units of t_1, such that there are 3 free parameters left for determining the position of Dirac points.

To determine the position of the zeroes, one can keep on the high symmetry line between $\mathbf{K}$ and $\mathbf{K}'$. Under the TRS of the model and C_3 symmetry of the Γ point, all the other solutions readily follow. One of the lines $\mathbf{KK}'$ lies at $k_y = 0$. Then the equation $f(\mathbf{k}) = 0$ depends only on the parameter k_x. If $\cos(\sqrt{3}k_x/2)$ is denoted by x, it follows that the band touchings are given by the equation

$$(1+2x)(8t_7x^3 + 4t_4x^2 + 2(t_3 - 4t_7)x + 1 - t_3 - 2t_4 + 2t_7) = 0. \tag{1.50}$$

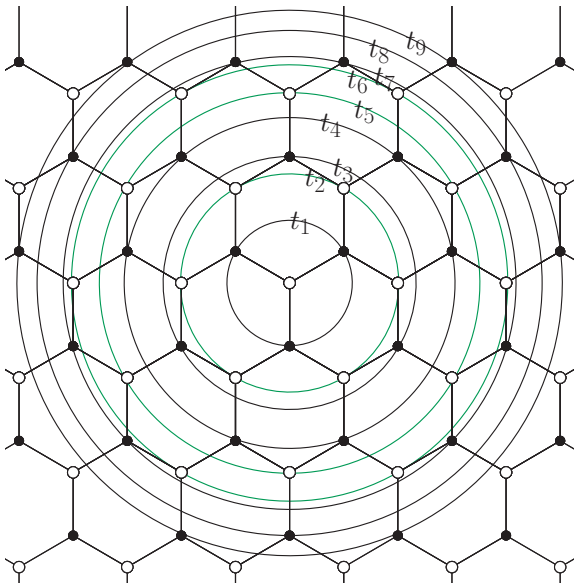

Fig. 1.7: The possible hoppings in graphene N9 model. From a central B atom, the neighbors are arranged in concentric circles. Hopping integrals between distant sites is denoted by t_i where i grows with the distance to the neighbor.

Eq. (1.50) has always a solution at $x = -1/2$. It corresponds to the regular **K** and **K**′ points in the NN graphene. This solution due to the symmetry of the hexagonal lattice is general and exists for any distant-neighbor-hopping model as long as it respects the original symmetries of the lattice. Therefore there will always be band touchings at these points in the graphene-like model.

If all solutions are real and distinct, then they correspond to Dirac points. However, if a solution has a multiplicity higher than one, then they describe points with nonlinear dispersion. In fact one can think of them as mergings of Dirac fermions. They will pose some conceptual problem for our method as the chirality

$$\chi(\boldsymbol{\kappa}) = \mathrm{sgn}(\partial_{k_x}\mathbf{h} \times \partial_{k_y}\mathbf{h})_3\big|_{\boldsymbol{\kappa}}, \tag{1.51}$$

is not defined at the merging points. These are points where the first derivatives vanish and $\chi = \mathrm{sgn}(0)$ is not well-defined. However the topological charge of the merging points is just the sum of the chiralities for the Dirac points that are converging to it. This fast calculation of charge associated to a band touching will be referred to as the sum rule [48].

Note that equation (1.50) has the number of free parameters equal to the order of the equation. This indicates that there might be a solution maximally degenerate. This unique point in parameter space is called a super-merging.

Let us suppose for the moment that all solutions are distinct, such that they represent Dirac points. The spectrum is symmetric under rotations with $2\pi/3$ around the center Γ of the Brillouin zone. Therefore for each solution near one of the points, two

more follow around the central one. Under the TRS, a mirror triplet is sure to exist at the opposite corner of the BZ. In conclusion, each $x \neq -1/2$ solution carries 6 band touchings. Let us treat in detail the cases with more distant hoppings.

N3 Graphene

The N3 graphene was already investigated in Ref. [54]. Here the presence of a strong t_3 hopping integral was shown to produce three more *satellite* points "orbiting" around each regular Dirac point. Solving Eq. (1.50) gives a possible band touching near **K**:

$$\boldsymbol{\kappa} = \frac{2\sqrt{3}}{3} \arccos\left(\frac{t_3 - 1}{2t_3}\right) \times (1, 0). \tag{1.52}$$

The solution is real only when t_3 obeys

$$\frac{t_3 - 1}{2t_3} \in (-1, 1). \tag{1.53}$$

Then for a large hopping $t_3 \in (-\infty, -1) \cup (1/3, \infty)$, these satellites appear and move along the high-symmetry lines between the regular Dirac points with the variation of t_3. Due to the TRI (time reversal invariance) and C_3 symmetry of the spectrum it is enough to follow the motion of a single satellite Dirac point in the BZ. Choosing the one in Eq. (1.52), it is seen in Fig. 1.8 that when t_3 varies from $-\infty$ to -1 the satellite points appear at mid distance (point Σ) between **K**(**K**′) points and the center Γ of the BZ, and move to annihilate at Γ. When t_3 varies from $\frac{1}{3}$ to ∞, the satellite Dirac points appear at M point and vanish at Σ.

It is noteworthy that during the evolution of a satellite point, there is a particular value of t_3 for which the satellite points merge with the regular Dirac points at **K**(**K**′). At $t_3 = 1/2$, there are three Dirac points merging with the associated regular Dirac points to form a point with quadratic dispersion. A merging point, where all satellites collide into the central Dirac point, is called a super-merging. It will be shown that up to N7 graphene the super-merging is unique.

The remaining satellites can be obtained by applying rotations of $2\pi/3$ around **K** and **K**′. For example, there are two satellites around **K**, denoted for notation simplicity also by $\boldsymbol{\kappa}$

$$\boldsymbol{\kappa} = \arccos\left(\frac{t_3 - 1}{2t_3}\right) \times \left(-\frac{\sqrt{3}}{3}, \pm 1\right). \tag{1.54}$$

Under time-reversal symmetry there are additional Dirac points at $\boldsymbol{\kappa}' = -\boldsymbol{\kappa}$.

The chirality χ of a Dirac point placed at $\boldsymbol{k}$ on BZ is readily determined by computing the sign of the Jacobian

$$\chi(\boldsymbol{\kappa}) = \mathrm{sgn}(\partial_{k_x}\mathbf{h} \times \partial_{k_y}\mathbf{h})_3\big|_{\boldsymbol{\kappa}}. \tag{1.55}$$

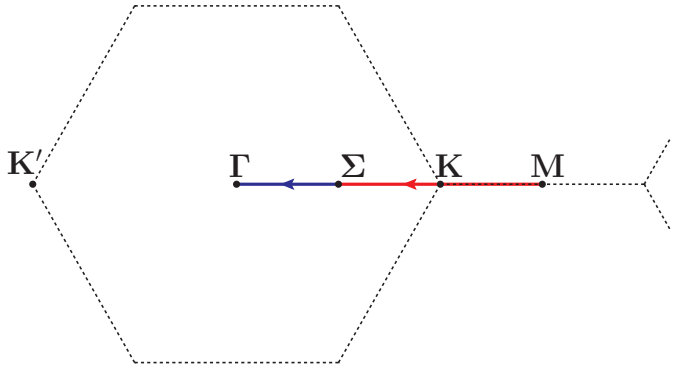

Fig. 1.8: In blue we represent the evolution of a satellite point in BZ, when t_3 varies from $-\infty$ to -1 and in red, when it varies from $1/3$ to ∞.

Dirac points	$\mathbf{K}$	$3 \times \boldsymbol{\kappa}$	$\mathbf{K}'$	$3 \times \boldsymbol{\kappa}'$
χ	1	-1	-1	1

Table 1.4: Chirality of the Dirac points in N3 graphene.

The symmetries of the system allow one to readily reduce the problem to that of finding the chirality of only two Dirac points: a regular one and a satellite Dirac point associated to it. If one is placed at $\boldsymbol{\kappa}$, then its time reversed partner exists at $-\boldsymbol{\kappa}$ and has opposite chirality. Satellite Dirac points that are obtained under a rotation by $2\pi/3$ around Γ share the same chirality.

As mentioned before, there are notable exceptions where formula (1.51) fails for t_3 tuned at the merging of satellite points at $\mathbf{K}^{(\prime)}$. This is because the merging point has a quadratic dispersion and the formula is undefined. However, near the merging point three satellite points of a given chirality converge to a regular Dirac point of opposite chirality. Such a scenario was treated before [47, 48] and was shown to yield a band touching point with quadratic dispersion in both directions. The chirality summation rule $\pm(1-3)$ is still applicable and indicates that the merging point at $\mathbb{K}^{(\prime)}$ is characterized by a chirality ± 2. Comparable cases are also encountered in bilayer graphene [47, 55, 56].

The topological charge -2 of the band touching at $\mathbf{K}$ can be equally read by expanding in small momenta (q_x, q_y) around the merging point

$$\mathbf{k} = \mathbf{K} + \mathbf{q}. \tag{1.56}$$

In this case, the function f in the effective Hamiltonian at in $\mathbf{K}$-valley is proportional to z^2, with $z = q_x + iq_y$. The power indicates a Berry phase of -2π picked by a fermion making one counter-clockwise revolution around the merging point $\mathbf{K}$. The other merging point is at $\mathbf{K}'$ and will have a topological charge 2.

graphene	Super-merging t_1	t_3	t_4	t_7	$f(\mathbf{K}+\mathbf{q})$	charge
NN	1	0	0	0	$\bar{z}$	1
N3	1	1/2	0	0	z^2	-2
N4	1	2/5	1/5	0	$z\bar{z}^2$	1
N7	1	7/12	1/4	1/12	$z^3\bar{z}$	-2

Table 1.5: Super-merging characteristics at **K**. The function f from the effective low-energy Hamiltonian $H_{\text{eff}} = \frac{1}{2} f\sigma_+ + \text{H.c.}$ is written as a function of small momenta $z = q_x + iq_y$ and up to a multiplicative constant which is neglected.

N4 Graphene

In the case of N4 graphene, there are two additional solutions possible at

$$x_\pm = -\frac{1}{4t_4}[t_3 \pm (t_3^2 + 8t_4^2 + 4t_3t_4 - 4t_4)^{1/2}]. \tag{1.57}$$

Therefore the maximum number of satellites around **K** can grow up to six. The dependence on two parameters makes it harder to find the existence conditions for the satellites. It is however easy to determine the parameters for which there is a super-merging solution. Imposing a triply degenerate solution, $x = -1/2$ in Eq. 1.50, it follows that the super-mergings develop at

$$t_3 = \frac{2}{5}, \qquad t_4 = \frac{1}{5}. \tag{1.58}$$

By perturbing the parameters around the super-merging points, one can see in Fig. 1.9 a regular Dirac point and the two triplets of satellites associated to it.

Expanding the Hamiltonian in small momenta **q** around **K** reveals that the super-merging has a cubic dispersion,

$$f_{\text{eff}}(\mathbf{K}+\mathbf{q}) \propto z\bar{z}^2. \tag{1.59}$$

Note that although the dispersion is cubic, the power counting gives a topological charge of one. This indicates that the Berry phase gained by an electron is only π. This is due to the fact that the super-merging is due to two sets of satellites with different chirality. Then the sum rule yields accordingly the chirality of the band touching at $\mathbb{K}$: $1 - 3 + 3 = 1$.

N7 Graphene and beyond

In N7 gaphene the position of the additional band touchings is given by a cubic equation. It is therefore harder to analyze the solution that follows. Though it easier to visualize it from the super-merging point, which can be determined from the condition that

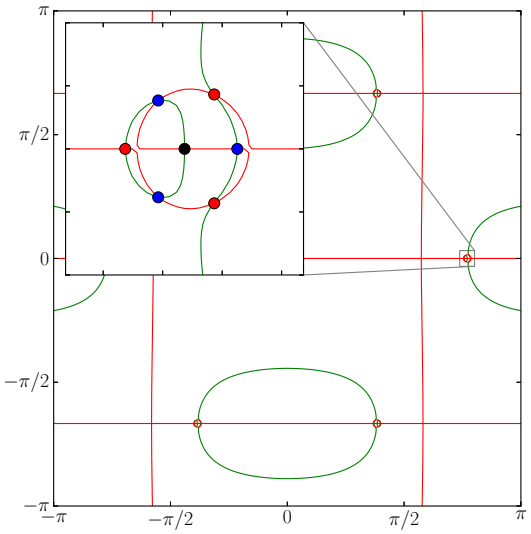

Fig. 1.9: The zero lines of h_1 (in green) and h_2 (in red) in N4 graphene. A small perturbation $(+0.001)$ of t_4 at the merging point $t_3 = 2/5$, $t_4 = 1/5$ creates 6 Dirac points around the stable Dirac points **K**. In the inset there is a zoom around **K**. The Dirac points are represented by full circles, •; there is a central **K** Dirac point in black, and 2 sets of satellite Dirac points, in blue and red.

$x = -1/2$ is four time degenerate solution to the equation (1.50). The super-merging is unique at

$$t_3 = \frac{7}{12}, \quad t_4 = \frac{1}{4}, \quad t_7 = \frac{1}{12}, \tag{1.60}$$

such that a perturbation will produce a maximum of 9 Dirac points around a regular Dirac point. The effective Hamiltonian shows now a quartic dispersion near **K**

$$f_{\text{eff}}(\mathbf{K}+\mathbf{q}) \propto z^3\bar{z}. \tag{1.61}$$

Again, although there is a high-order dispersion, the low topological charge is explained by the alternating chirality for the 3 sets of satellite Dirac points near the super-merging.

There are no longer unique super-merging points for graphene Nm, with $m > 7$. This is due to the fact that already band touchings in N8 graphene have an equation that remains cubic in x. Therefore there is no single unique choice of parameters for which the solution $x = -1/2$ has multiplicity four. Therefore, even if a more distant-neighbor hopping will add one order to the equation, the order of the equation will never match again the number of coefficients.

Factoring out the trivial solution at $x = -1/2$, the equation for Dirac points in N8 graphene reads

$$8(t_7+t_8)x^3 + 4(t_4-t_8)x^2 + 2(t_3-4t_7-3t_8)x + 1 - t_3 - 2t_4 + 2t_7 + 3t_8 = 0 \tag{1.62}$$

hopping	physical distance	chemical distance
t_2	$\sqrt{3}$	2
t_5	3	4
t_6	$2\sqrt{3}$	4

Table 1.6: First hopping integrals between equivalent sites.

There are still super-merging points possible, but they are no longer unique. Note that it is possible to have partial merging points where there are solutions with high multiplicity. Regardless, as the order of the polynomial grows and the space of parameters becomes larger, we conjecture that it will always be possible to find solutions that are all real and smaller than one in absolute value. That will lead to a multiplication of triplets of satellite Dirac points.

1.4.2 Phases of the Haldane model

The original Haldane model is built on the hexagonal lattice for NN graphene by adding N2 hopping t_2, such that when hopping is performed clockwise in the unit cell an electron gains a phase ϕ. It is enough to consider the mass term $h_3\sigma_3$ and throw away the identity term, which just breaks the particle-hole symmetry and shifts (topologically) trivially the bands.

The mass term, $h_3\sigma_3$, which breaks time reversal and inversion symmetry, reads

$$h_3 = M - 2t_2 \sin\phi[\sin(\mathbf{k}\cdot\mathbf{a}_2) - \sin(\mathbf{k}\cdot\mathbf{a}_1) + \sin(\mathbf{k}\cdot(\mathbf{a}_1 - \mathbf{a}_2))]. \tag{1.63}$$

When hopping between distant sites is allowed, the generalized mass term reads

$$\begin{aligned} h_3 = M - \sum_n 2t^{(n)} \sin(n\phi)[&\sin(n\mathbf{k}\cdot\mathbf{a}_2) - \sin(n\mathbf{k}\cdot\mathbf{a}_1) \\ &+ \sin(n\mathbf{k}\cdot(\mathbf{a}_1 - \mathbf{a}_2))], \end{aligned} \tag{1.64}$$

where n is an integer that indicates that hopping takes place between AA or BB sites situated at a distance of $n\sqrt{3}a$. Only the first two terms in this expression are considered in the following; they correspond to a maximal two-unit-cell hopping. The term containing the hopping integral t_5 multiplies the identity Pauli matrix and is neglected in the following. Interesting for the topology of the problems are hoppings along the links where the electrons gain the phase ϕ. The first two components of the mass term which have this property are the t_2 and t_6 terms.

Gapping $2n$ Dirac points can yield Chern number phases n. In the following subsections, cases where different mass term gaps the system are studied for different underlying graphene models.

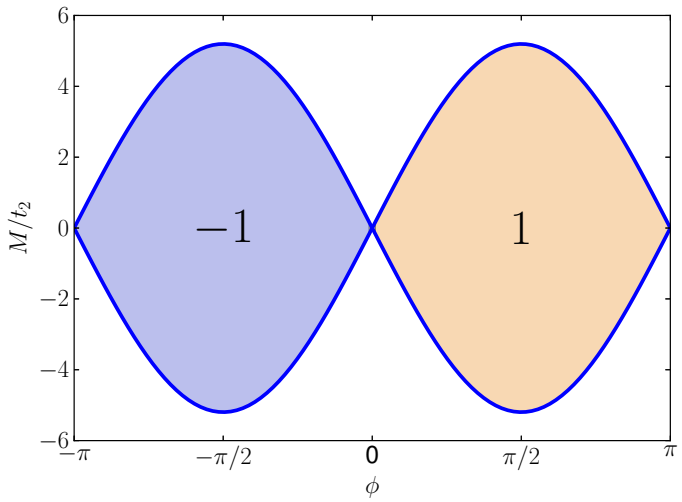

Fig. 1.10: Phase diagram for the Haldane Hamiltonian as a function of the on-site energy M, divided by the hopping integral t_2, and the flux ϕ. The topologically nontrivial insulating phases are color-identified and have the topological index denoted inside the respective regions. The topologically insulating regions, $\mathcal{C} = 0$, are white.

Haldane t_2 model

NN graphene with a hopping t_2 constitutes the original Haldane model. The phase diagram is obtained by observing that h_3 changes sign between the Dirac points ($\mathbf{K}^{(\prime)}$) of graphene. Therefore the Hamiltonian exhibits three topological phases; a trivial insulating phase and two $|\mathcal{C}| = \pm 1$ QAH phases. Eq. (1.30) yields in this case

$$\mathcal{C} = \frac{1}{2}(\mathrm{sgn}\mathcal{M}_+ - \mathrm{sgn}\mathcal{M}_-), \tag{1.65}$$

where $\mathcal{M}_\pm = M \mp 3\sqrt{3}t_2 \sin\phi$ is the mass term at $\mathbf{K}'$, and $\mathbf{K}$ respectively. The phase diagram is represented in Fig. 1.10. The lines $\mathcal{M}_\pm = 0$ represent topological transition lines where the bulk gap closes at least at one of the $\mathbf{K}$ and $\mathbf{K}'$ points.

Larger Chern phases become possible when the underlying model is N3 graphene. The mass term has the same sign for a regular Dirac point and its satellites, and opposite sign at the time reversed points. Therefore, when the satellites exist, the gapped phases will be indexed by Chern number, $|\mathcal{C}| = 2$.

Momentum $\boldsymbol{\kappa}^{(\prime)}$ locates any satellite point of $\mathbf{K}^{(\prime)}$ and, manifestly, the expression for $\chi(\boldsymbol{\kappa}^{(\prime)})$ holds in the range of existence of satellite points.

Let us define the mass at the regular Dirac points $\mathcal{M}_\pm = \mathcal{M}\big(\mp(\frac{4\pi}{3\sqrt{3}}, 0)\big)$. The mass at the satellite Dirac points is denoted by $m_{+(-)}$, if it is associated to the regular Dirac point $\mathbf{K}'$ ($\mathbf{K}$). Then it follows from Eq. (1.30) and Tab. 1.4 that

$$\mathcal{C} = \frac{1}{2}\Big[(\mathrm{sgn}\mathcal{M}_- - \mathrm{sgn}\mathcal{M}_+) - 3(\mathrm{sgn}m_- - \mathrm{sgn}m_+)\Big], \tag{1.66}$$

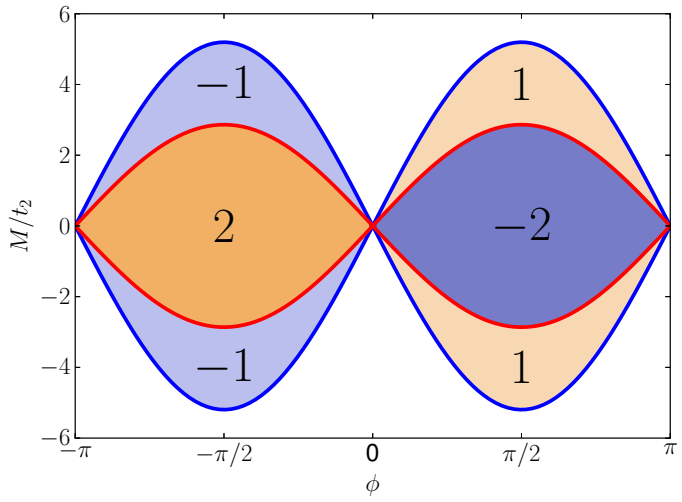

Fig. 1.11: Phase diagram for the N3 Haldane Hamiltonian. The hopping parameters are $t_2 = 1/3$ and $t_3 = 0.35$ in units of t_1.

where the mass of the Dirac points reads

$$\begin{aligned} \mathcal{M}_\pm &= M \mp 3\sqrt{3}t_2 \sin\phi, \\ m_\pm &= M \mp 2\frac{t_2}{t_3}(1+t_3)\sqrt{1-\left(\frac{1-t_3}{2t_3}\right)^2}\sin\phi. \end{aligned} \tag{1.67}$$

Eq. (1.66) yields the phase diagram for the system when all eight Dirac points are present. When there are no satellite Dirac points ($t_3 \in (-1, 1/3)$), the topology of the system is in fact identical to the original system $t_3 = 0$ and therefore it has the phase diagram represented in Fig. 1.10. When t_3 is varied to go outside the region $(-1, 1/3)$, two phases of higher Chern number develop around the $M = 0$ line. A typical phase diagram for the case where satellite Dirac points exist is represented in Fig. 1.11. For example, from Eqs. (1.67), it follows that at $M = 0$ a regular Dirac point and its satellites will have the same mass. Therefore the Chern number reduces to $\mathcal{C} = \mathrm{sgn}\mathcal{M}_+ - \mathrm{sgn}\mathcal{M}_-$. This yields topological phases indexed by ± 2. By increasing $|M|$, one crosses a transition line where the Haldane mass of all satellite points in the system becomes identical, while it remains different for the regular Dirac points. This transition is given by

$$m_\pm = 0. \tag{1.68}$$

This region extends up to the the last topological transition line given by $\mathcal{M}_\pm = 0$. In this region the Chern number reduces again to the original case ($t_3 = 0$) with $\mathcal{C} = 1/2(\mathrm{sgn}\mathcal{M}_- - \mathrm{sgn}\mathcal{M}_+)$. When M is increased even further, all Dirac points are gapped identically and therefore this is the topologically trivial region.

Note that the $\mathcal{C} = \pm 1$ phases completely vanish at the merging point $t_3 = 1/2$, and the phase $\mathcal{C} = \pm 2$ would have maximal area delimited by $M = \pm 3\sqrt{3}t_3 \sin\phi$. Then, at

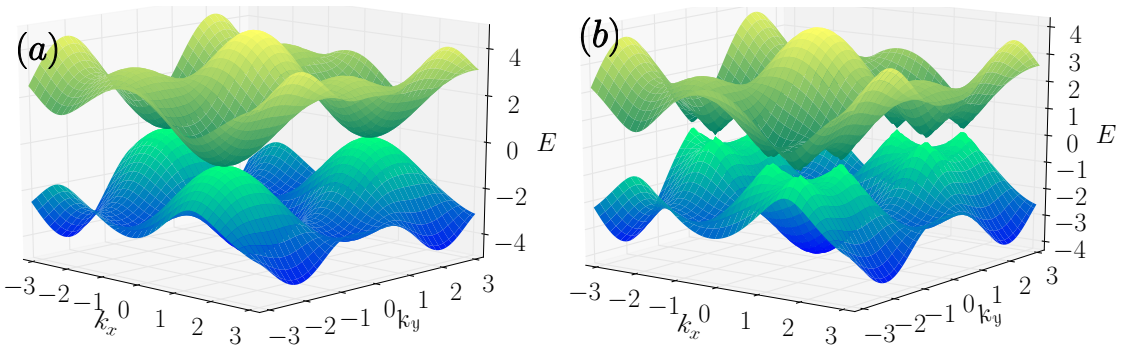

Fig. 1.12: Energy dispersion for the Haldane t_2 model on N3 graphene at a topological transition between two QAH phases (at $\phi = \pi/2$ and $t_2 = 1/3$). (a) Topological transition between $\mathcal{C} = -2$ and $\mathcal{C} = 0$ phases at the merging point between the regular $\mathbf{K}'$ and its three satellites $\boldsymbol{\kappa}'$ in N3 graphene. The energy dispersion in N3 Haldane shows a quadratic band touching at $\mathbf{K}'$ for $M = \sqrt{3}$, $t_3 = 0.5$. (b) Topological transition between $\mathcal{C} = 1$ and $\mathcal{C} = -2$ phases. Three Dirac cones form at the satellite points of $\mathbf{K}'$ for $t_3 = 0.35$ and $M \approx 0.95$, indicating a change of the Chern number by 3 units at the topological transition.

the topological transition from $|\mathcal{C}| = 2$ phase to the trivial insulator, there is a quadratic band touching that is represented in Fig. 1.12(a).

The phase diagram in N3 Haldane model (see Fig. 1.11) has the nice feature that it accommodates lines of transition where Chern number changes by 3 units. This is realized by the formation of three Dirac points at the topological transition. These band touchings come from the vanishing of the Haldane mass at the three satellite Dirac points previously found in N3 graphene. For example, let us take parameters $t_1 = 1$, $t_2 = 1/3$ and $t_2 = 0.35$ from the phase diagram in Fig. 1.11. Then fixing $\phi = \pi/2$, there are two transition points between $\mathcal{C} = -2$ and $\mathcal{C} = 1$ phases near $\mathbf{K}$ or $\mathbf{K}'$. In particular, near $\mathbf{K}'$, the Dirac points form at the satellites where $m_+ = 0$. The energy dispersion at the topological transition is illustrated in Fig. 1.12(b).

Similarly, one can take as underlying model the N4 graphene model which contains the t_3 hopping. In Fig. 1.13 are represent the QAH phases that can appear for a particular choice of parameters.

Haldane t_6 model

The existence of $2n$ Dirac points for a submodel containing only two sigma matrices allows in principle to build topological insulators with Chern phases $\mathcal{C} = n$. The N3 graphene model with eight Dirac points can present a large Chern number, $\mathcal{C} = \pm 4$. To actualize all possible topological phases it is sufficient to add a t_6 mass term. It has the effect to produce oscillations in the phase-dependent Haldane mass, such that the term changes sign between a regular graphene Dirac point and its satellites in N3 graphene. As expected, all phases are attainable under this modification of the Hamiltonian.

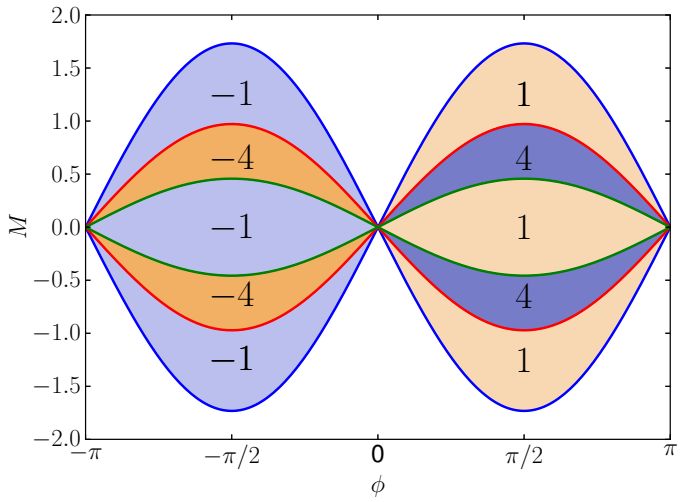

Fig. 1.13: Phase diagram showing the existence of 2 sets of satellite Dirac points. The parameters are $t_1 = 1, t_2 = 1/3\, t_3 = 0.59$ and $t_4 = 0.4$.

The mass term becomes

$$\begin{aligned} h_3 = M &- 2t_2 \sin\phi)[\sin(\mathbf{k}\cdot\mathbf{a}_2) - \sin(\mathbf{k}\cdot\mathbf{a}_1) + \sin(\mathbf{k}\cdot(\mathbf{a}_1 - \mathbf{a}_2))] \\ &- 2t_6 \sin(2\phi)[\sin(2\mathbf{k}\cdot\mathbf{a}_2) - \sin(2\mathbf{k}\cdot\mathbf{a}_1) + \sin(2\mathbf{k}\cdot(\mathbf{a}_1 - \mathbf{a}_2))]. \end{aligned} \tag{1.69}$$

The new phase diagram is computed by considering the mass term (1.69) at the eight N3 graphene Dirac points. Then the topological transition lines are given by the zeroes of the new mass terms, $\mathcal{M}'_\pm, m'_\pm$, expressed as a function of the previous mass terms from Eq. (1.67)

$$\begin{aligned} \mathcal{M}'_\pm &= \mathcal{M}_\pm \pm 3\sqrt{3}t_6 \sin 2\phi \\ m'_\pm &= m_\pm \mp 2t_6 \sin 2\phi(2\sin 2\kappa - \sin 4\kappa), \end{aligned} \tag{1.70}$$

where $\kappa = \arccos[(t_3 - 1)/(2t_3)]$ holds in the domain of existence for satellite Dirac points in N3 graphene.

The dependence of the mass term on $\sin 2\phi$ allows large Chern number phases, $|\mathcal{C}| = \pm 4$. Because the mass can now change sign not only between a regular Dirac point and its time-revered partner, but also between the regular one and its satellites (see Fig. 1.15). Therefore, when system parameters are varied, N6 Haldane model can present all Chern phases between -4 and 4. A phase diagram that illustrates this point is represented in Fig. 1.14(a).

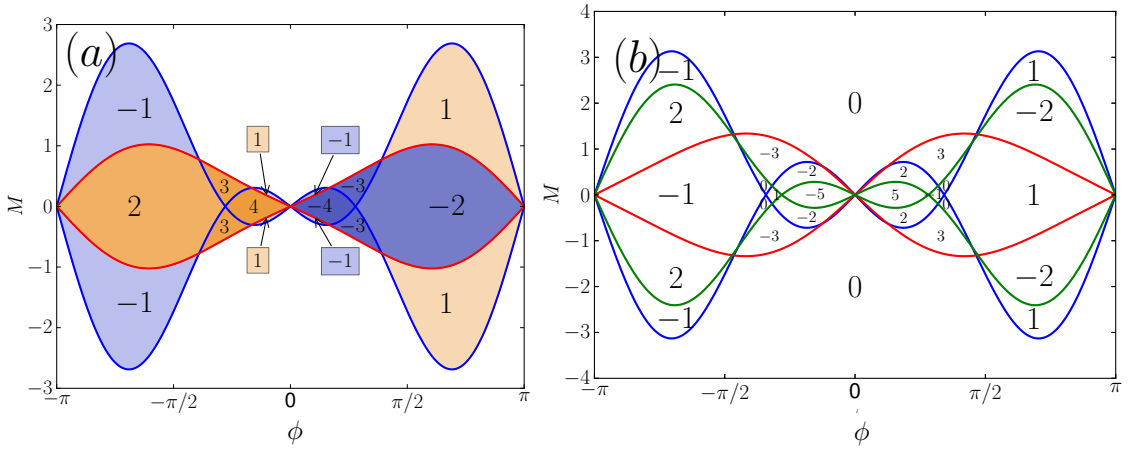

Fig. 1.14: (a) All QAH phases possible for N3 graphene become available in Haldane t_6 model. Phase diagram for the choice $t_1 = 1$, $t_2 = 1/3$, $t_3 = 0.35$, and $t_4 = 0.26$. (b) Haldane model from N4 graphene with a t_6 mass term. Hopping integrals are $t_1 = 1$, $t_2 = 1/3$, $t_3 = 0.43$, $t_4 = 0.3$, $t_6 = 0.35$ and $t_7 = 1/3$.

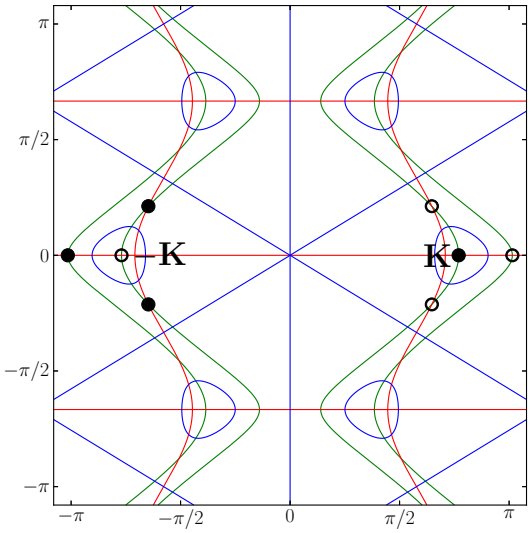

Fig. 1.15: A Dirac point that is represented by • (○) has chirality + (−). The colored lines represent lines of zeros for h_1 (green), h_2 (red), and the mass term h_3 (blue). The regular Dirac points placed at $\left(\pm\frac{4\pi}{3\sqrt{3}}, 0\right)$ are gapped by a Haldane mass that has opposite sign. Also the mass term changes sign between the regular Dirac point and its satellites. For parameters $t_1 = 1$, $t_2 = 1/3$, $t_3 = 0.35$, $t_6 = 0.26$, $M = 0$ and $\phi = \pi/8$ the phase is $\mathcal{C} = -4$.

Let us consider shortly the case of N4 and N7 graphene with t_6 mass term. There are two new free parameters t_4 and t_7. The parameters space becomes quite large to describe analytically the dynamics of the Dirac points and to track at the same time the sign of the

mass at the Dirac points. The general thesis remains however correct: larger and larger QAH phases become possible. In the case of N4 graphene there is a maximum of six Dirac points near a **K** point; for N7 graphene there are nine possible Dirac points. This indicates that with a proper mass term one can have the largest Chern phases $|\mathcal{C}| = 7$ (in N4 graphene) or $|\mathcal{C}| = 10$ (in N7 graphene). In Fig. 1.14(b), it is represented a case with large $\mathcal{C} = 5$ phases.

1.5 Discussion

The polynomial whose zeroes determines the position of the Dirac fermions becomes quickly of too high degree for analytical prehension. Nevertheless, what transpired here is that truly the topological phases with high Chern number can be indeed induced through addition of distant-neighbor hopping. As a side result, a model for graphene was studied and was shown that adding distant-neighbor hoppings increases the number of Dirac points. They move under a variation of parameters and there are unique super-merging points in parameter space where all additional Dirac points merge with the **K** and **K**′ from the regular graphene. They form points with a high-order energy dispersion. However, the absolute value of the topological charge associated to the super-merging never grows larger than two because the satellite points always come in triplets with opposite charges. Unfortunately the study is mostly academic and serves as a proof of principle. The degree of control required to realize the super-mergings and the presence of extreme distant-neighbor hopping remain rather problematic. However it would be possible to find multi-layer materials which are be mapped to two-band models with effective-long range hopping. These systems could use the methods developed in this chapter to analytically chart their topological phase diagram [37].

Chapter 2

Edge states in a Chern two insulator

The present chapter focuses on the toy model from Sec. 1.3. It was shown previously that this model supports topological phases with Chern number $|\mathcal{C}| = 2$. The phase diagram of the system was determined by considering only bulk properties. When the system is realized on a finite geometry, there will be edges where the system connects with a trivially gapped phase, here the vacuum. As a consequence there will be edge states equal in number to the Chern index [15].

The question posed here is what quantum number differentiates the two edge states that can appear in the model. Here it is shown through different numerical and analytical techniques that it is a valley number that demarcates the edge (Secs. 2.1 and 2.2). Moreover, the model is extended by adding spin degrees of freedom, such that it is converted in a time-reversal invariant $\mathbb{Z}_2$ insulator. The edge states from the $|\mathcal{C}| = 2$ phase are explicitly gapped by one-particle TRI perturbations (Sec. 2.3). This confirms that even Chern numbers produce trivial $\mathbb{Z}_2$ phases [52, 57, 58]. In the final Sec. 2.4, there are an infinite number of interfaces engineered between two alternating topological phases of the same Hamiltonian. It is possible to deduce the topological phase of overall model from knowledge of the Chern number of the constituent stripes.

The momentum space Hamiltonian of the model 1.41 reads

$$H = 2t_1 \cos(k_x)\sigma_1 + 2t_1 \cos(k_y)\sigma_2 + [m + 2t_2 \cos(k_x + k_y) + 2t_3(\sin(k_x) + \sin(k_y))]\sigma_3 \tag{2.1}$$

with a topological invariant given by

$$\mathcal{C} = \text{sgn}(-m - 2t_2) + \frac{1}{2}[\text{sgn}(m - 2t_2 + 4t_3) + \text{sgn}(m - 2t_2 - 4t_3)]. \tag{2.2}$$

The Hamiltonian (2.1) is implemented on a cylinder and, subsequently, edge states form at the bottom and top sides of the cylinder where the lattice terminates abruptly. The following sections investigate the edge state wave functions and their respective energy dispersion.

2.1 Numerical experiments

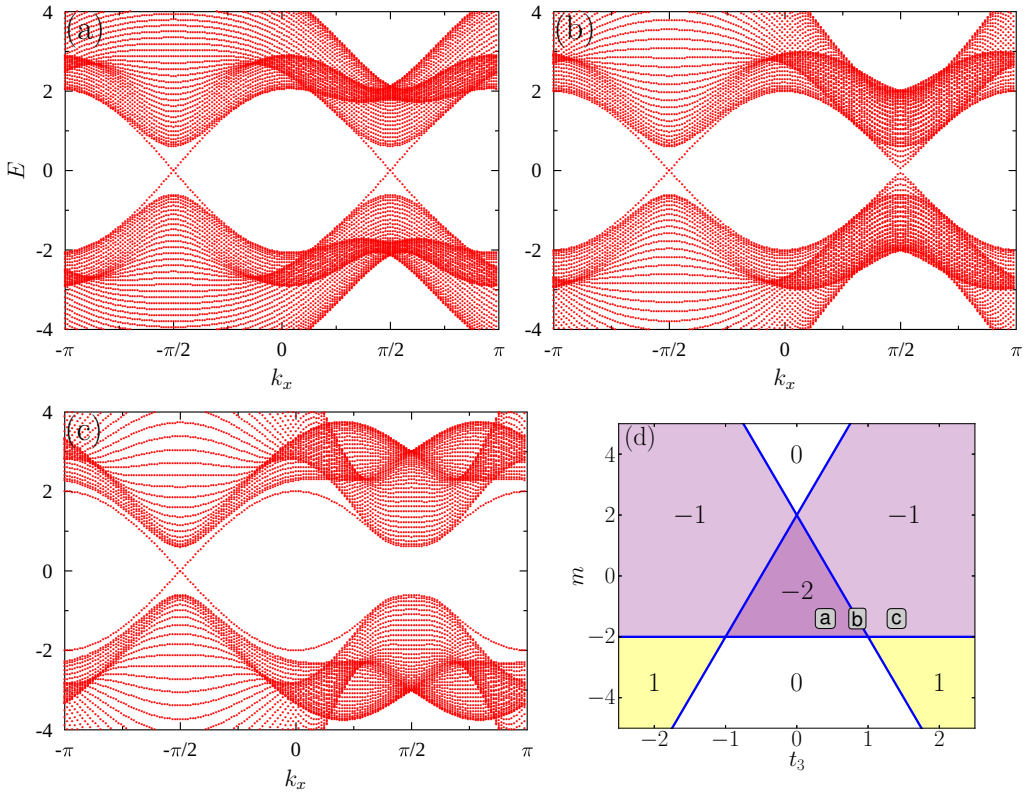

Fig. 2.1: Zig-zag edge energy dispersion when the bulk Hamiltonian is in different Chern phases. The simulation is done for the system on a cylinder with height of 40 sites and circumference of 180 sites. The number of edge states is $2 \times |\mathcal{C}|$ because there are two edges. Energy dispersions for (a) $t_3 = 0.4$ ($\mathcal{C} = -2$), (b) $t_3 = 0.85$ (topological phase transition at closing bulk gap), (c) $t_3 = 1.6$ ($\mathcal{C} = -1$). The other parameters are $t_1 = 1$, $t_2 = 1$, $m = -1.4$. (d) The representation of chosen points on the phase diagram.

The finite geometry chosen for the numerical study is a cylinder. It is constructed out of a patch of the lattice having the shape of a parallelogram with Bravais vectors $\mathbf{a}_1$ and $\mathbf{a}_2$ as edges. Subsequently the edges parallel to $\mathbf{a}_2$ are glued together to obtain the the final cylindrical shape. Because translational invariance is maintained in the direction parallel to $\mathbf{a}_1$, k_x remains a good quantum number. Therefore, one can fix k_x and consider the resulting one-dimensional problem. Let us write the one-particle solutions of the corresponding stationary Schrödinger equation as

$$|\psi(k_x, j)\rangle = \sum_{k_x} \psi_j(k_x) c^\dagger_{k_x,j} |0\rangle, \tag{2.3}$$

where j denotes the layers of sites in $\mathbf{a}_2$ direction, and ψ_j is a spinor due to the fact that there are two orbitals in the problem.

Then for a given quasi-momentum k_x, the Schrödinger equation reads

$$\Gamma_1\psi_j + \Gamma_2\psi_{j+1} + \Gamma_2^\dagger\psi_{j-1} = E\psi_j, \tag{2.4}$$

where

$$\begin{aligned}\Gamma_1 &= m\sigma_3 + 2t_1\cos(k_x)\sigma_1 + 2t_3\sin(k_x)\sigma_3,\\ \Gamma_2 &= t_1\sigma_2 + (t_2e^{ik_x} - it_3)\sigma_3.\end{aligned} \tag{2.5}$$

The cylinder has the edges at $j = 1$ and $j = L_y$. There are hard wall boundary conditions, to the effect that the amplitudes ψ_0, ψ_{L_y+1} must vanish. The energy dispersion as a function of k_x is obtained by numerically solving Eq. (2.4) for the given boundary conditions and for different choices of the parameters (see Fig. 2.1). In our numerical experiments the cylinder circumference is $L_x = 180$ sites and with height $L_y = 40$ sites. All the energies are measured in units of t_1.

The bulk-edge correspondence is illustrated by sampling several regions of the phase diagram in Fig. 1.5. In non-trivial topological regions, edge states appear around the ends of the cylinder. The number of edge states at a given end equals the absolute value of the Chern number. For example, three sets of parameter values along the constant $m = -1.4$ line are taken such that the transition between the $\mathcal{C} = -1$ and $\mathcal{C} = -2$ phases is explored (see Fig. 2.1(d)).

While the bulk remains insulating there are states crossing the gap. These are the edge states and their total number is $2 \times |\mathcal{C}|$ since the cylinder has two edges. Note that the edge states at zero energy, cross the gap at $k_x = \pm\pi/2$. At any topological transition the bulk closes at least in one of the special points $k_x = \pm\pi/2$. A transition changing the Chern number by two requires that the gap closes at both points, while for a change of one, only one Dirac cone forms.

2.2 Analytical solution

A greater insight into the model is gained by solving Eq. (2.4) analytically. In this way, the gapless states are clearly identified as edge states and their penetration length into the bulk is determined. The edge state dispersion law can be found either by directly solving the Schrödinger equation or indirectly by studying the bulk Hamiltonian through a method described in Ref. [59]. Both approaches are explored in the general setting of the model and are exemplified for a particular choice of parameters corresponding to the phase $\mathcal{C} = -2$.

2.2.1 Edge states from bulk Hamiltonian

As it was elegantly proved in Ref. [59], the condition of existence and edge state dispersion can, under certain provisions, be found from a simple analysis of bulk Bloch

Hamiltonians. The method developed by the authors applies when an infinite ribbon or a cylinder is cut out of the infinite 2D system. The direction of the cut must follow a Bravais lattice vector. In this case the momentum parallel to the cut $k_\parallel$ is conserved and the system splits into a set of 1D Hamiltonians describing the motion of the electron between the layers of sites parallel to the cut. The final prerequisite to apply the method is that there are only nearest-neighbor layer hopping terms. Eq. (2.4) shows that it is indeed the case in the present model with $k_\parallel = k_x$.

The key information about the edge states can be revealed by studying the curves traced by $\mathbf{h}$ as a function of $k_\perp$ with fixed $k_\parallel$. For the case with only nearest-neighbor layer hopping allowed, these curves are planar (actually they are ellipses). Therefore, $\mathbf{h}$ can be decomposed in two parts, $\mathbf{h}_\perp$ perpendicular to the ellipse plane and $\mathbf{h}_\parallel$ the in-plane component. Each component yields some important piece of information about the edge states. Namely, the edge state with a given $k_\parallel$ exists if and only if the ellipse traced by $h_\parallel$ encloses the projection of the origin onto the plane of the ellipse. The energy of the state is equal to $\pm|\mathbf{h}_\perp|$.

In the present case $k_\parallel = k_x$ and $k_\perp = k_y$. This yields

$$\mathbf{h}_\parallel = (0, 2t_1 \cos(k_y), 2t_2 \cos(k_x)\cos(k_y) + 2(t_3 - t_2 \sin(k_x))\sin(k_y) + m + 2t_3 \sin(k_x)). \tag{2.6}$$

For a fixed k_x, the equation (2.6) describes an ellipse parametrized by $k_y \in [0, 2\pi)$. The condition that the ellipse encloses the origin reads

$$|m + 2t_3 \sin(k_x)| < 2|t_3 - t_2 \sin(k_x)|. \tag{2.7}$$

This equation determines the range in k_x where edge states exist. The energy of the state is $\pm 2t_1 \cos(k_x)$.

Although the edge dispersion is determined, it still remains to resolve the wave-function for the edges states. Also the existence condition for $|\mathcal{C}| = 2$ phase must allow four edge states, and therefore it is left to find the extension in k_x for each edge solution separately. These limitations of the above method demand a more applied study of the edge states.

2.2.2 Edge states from the Schrödinger equation

The equation characterizing the wave function amplitudes for the edge states have the form of a recurrence relation. Then one can find a solution using the method of the generating functions. Here the solution follows closely the method used in Ref. [60]. It involves determining the energy dispersion by studying the poles of the generating function associated to the edge states. Subsequently, this is followed by constructing the eigenvectors of the Schrödinger equation yielding localized wave functions at two edges of the cylinder. It is shown that the solutions always cross at specific points in the BZ and, subsequently, can have an associated "valley" quantum number.

Let us write the Schrödinger equation for the edge states, complete with the boundary conditions. For the moment, assume that there is only one edge and the other one is pushed to infinity. That is enough to find the energy dispersion and "spinor" wave function for the edge states.

The Schroödinger equation from Eq. (2.4) with explicit boundary condition at the edge, $j = 1$, reads

$$\begin{aligned} 0 &= (\Gamma_1 - E)\psi_j + \Gamma_2\psi_{j+1} + \Gamma_2^\dagger\psi_{j-1}, \quad j > 1, \\ 0 &= (\Gamma_1 - E)\psi_1 + \Gamma_2\psi_2, \end{aligned} \tag{2.8}$$

where

$$\begin{aligned} \Gamma_1 &= m\sigma_3 + 2t_1\cos(k_x)\sigma_1 + 2t_3\sin(k_x)\sigma_3, \\ \Gamma_2 &= t_1\sigma_2 + (t_2e^{ik_x} - it_3)\sigma_3. \end{aligned} \tag{2.9}$$

Multiply the j^{th} equation by z^j, where z is a complex number. Summing the equations it follows that

$$\sum_{j=1}^{\infty} z^{j-1}[\Gamma_2^\dagger\psi_j + (\Gamma_1 - E)\psi_{j+1} + \Gamma_2\psi_{j+2}] = 0. \tag{2.10}$$

Let us introduce the generating function

$$G(z) = \sum_{j=1}^{\infty} z^{j-1}\psi_j. \tag{2.11}$$

Then using the boundary condition in Eq. (2.10), it follows that the Schrödinger equation reads

$$[z^2\Gamma_2 + z(\Gamma_1 - E) + \Gamma_2]G(z) = \Gamma_2^\dagger\psi_1. \tag{2.12}$$

Edge states exist only if its poles have all a modulus greater than one [60]. If all poles of the generating function have modulus less then one, then they correspond to wave function amplitudes that grow in the bulk. For an exponentially localized function at the edge, all poles must be greater than one.

The generating function is given by

$$G(z) = [z^2\Gamma_2 + z(\Gamma_1 - E) + \Gamma_2]^{-1}\Gamma_2^\dagger\psi_1. \tag{2.13}$$

Let us denote for convenience $\alpha = 2t_1\cos(k_x)$, $\beta = m + 2t_3\sin(k)$, $\gamma = t_2e^{ik_x} - it_3$ and $\Gamma_2\psi_1 = \binom{\phi_1}{\phi_2}$. The generating function reads

$$\begin{aligned} G(z) &= N(z)/D(z), \\ N(z) &= \begin{pmatrix} z^2(\gamma^*\phi_1 - it_1\phi_2) + z((E+\beta)\phi_1 + \alpha\phi_2) + \gamma\phi_1 - it_1\phi_2 \\ z^2(-\gamma^*\phi_1 + it_1\phi_2) + z((E-\beta)\phi_2 + \alpha\phi_1) - \gamma\phi_2 + it_1\phi_1 \end{pmatrix}. \end{aligned}$$

The denominator $D(z)$ is a polynomial of order four in z. Therefore it has four generally complex roots. It has the property that if z_1 is a solution, then also $1/z_1^*$ is a solution. Let us assume that $z_{1,2}$ are solutions with $|z_{1,2}| < 1$. Then a localized edge solution exists, if the roots $z_{1,2}$ are simplified with the roots of the numerator. That is equivalent to say that the two components of $N(z)$ are linearly dependent and both proportional to $(z - z_1)(z - z_2)$.

Therefore the coefficient of z^2 and z^0 are proportional, yielding the energy independent relation between the components

$$(\gamma^* - \gamma)(\phi_1^2 - \phi_2^2) = 0. \tag{2.14}$$

The solution $\gamma^* = \gamma$ is unacceptable because the Viète relations require

$$|z_1 z_2| = 1. \tag{2.15}$$

This goes against the premise that both have modulus smaller than one. Therefore it leaves to impose $\phi_1^2 = \phi_2^2$. Hence the edge states ψ_1 can be chosen to be proportional to eigenstates of σ_1

$$|x\pm\rangle = \frac{1}{\sqrt{2}} \begin{pmatrix} 1 \\ \pm 1 \end{pmatrix}. \tag{2.16}$$

The energy of the edge state can be determined by returning in $N(z)$ and applying again the linear dependence condition with the constraint that $\phi_1 = \pm\phi_2$. This yields the energy dispersion for edges localized at $j = 1$

$$E_\pm = \pm 2t_1 \cos(k_x), \quad \text{for } |x\pm\rangle. \tag{2.17}$$

Let us create another edge at $j = N$. The system is now a cylinder with bottom at $j = 1$ and top at $j = N$. There are hard wall boundary conditions for the wave functions, and hence there are vanishing amplitudes ψ_0 and ψ_{N+1}. The edge states localized at N will be similarly eigenstates of σ_1 with respective energies, $E_\pm = \pm 2t_1 \cos(kx)$. However, it remains to determine in the following the decay of the edge wave function in the bulk, and their extension in momentum space. The latter is addressed when assessing the existence conditions for the solutions. Because the number of edge solutions depends on the Chern phase, there are solutions that must vanish when model parameters are varied.

To construct the edge wave function use the Ansatz

$$\psi_j = z^j |x\pm\rangle. \tag{2.18}$$

Note that the equation in the bulk of the cylinder reads

$$[z^2\Gamma_2 + z(\Gamma_1 - E_\pm) + \Gamma_2^\dagger]|x\pm\rangle = \begin{pmatrix} 0 \\ 0 \end{pmatrix} \tag{2.19}$$

For the $|x+\rangle$, and, respectively, $|x-\rangle$ it follows that

$$z^2(\mp it_1 + t_2 e^{ik_x} - it_3) + z[m + 2t_3 \sin(k_x)] + (\mp it_1 + t_2 e^{-ik_x} + it_3) = 0. \quad (2.20)$$

Note that if z_1 and z_2 are solutions for the equation corresponding to eigenstates $|x+\rangle$, then $1/z_1^*$ and $1/z_2^*$ are solutions for the equation corresponding to $|x-\rangle$.

Then at each edge there can be at most two solutions one corresponding to $|x+\rangle$ and one to $|x-\rangle$. However to construct the wave function solution is necessary to apply the boundary condition. This is exemplified in the following for a solution corresponding to $|x+\rangle$ that is localized at the bottom edge, $j = 1$.

Because there are two eigenmodes $z_{1,2}$ associated to a "spinor", the wave function reads

$$\psi_j = (c_1 z_1^j + c_2 z^j)|x+\rangle, \quad (2.21)$$

where $c_{1,2}$ are coefficients. The boundary condition, $\psi_0^T = (0, 0)$, constrains the coefficients $c_+ := c_2 = -c_1$. The coefficients $c_{+,-}$ correspond to $|x\pm\rangle$ eigenstates. They are fixed by applying boundary conditions at the edges of the cylinder, but they are not of concern here.

Thus if there is an edge state solution, its form and energy are

$$\begin{aligned} \psi_j^{+b(t)} &= c_+(z_1^j - z_2^j)|x+\rangle, & E &= 2t_1 \cos(k_x), \\ \psi_j^{-b(t)} &= c_-(z_1^{*-j} - z_2^{*-j})|x-\rangle, & E &= -2t_1 \cos(k_x), \end{aligned} \quad (2.22)$$

where the index $b\,(t)$ denotes an edge state localized near the bottom (top) of the cylinder. The eigenmodes are determined from the quadratic Eq. (2.20)

$$z_{1,2} = \frac{-b \pm \sqrt{b^2 - 4ac}}{2a}, \quad (2.23)$$

with

$$\begin{aligned} a &= -it_1 + t_2 e^{ik_x} - it_3, \\ b &= m + 2t_3 \sin(k_x), \\ c &= -it_1 + t_2 e^{-ik_x} + it_3. \end{aligned} \quad (2.24)$$

It is manifest that the model can have zero, one or two solutions at an edge. For concreteness, let us examine the states localized at cylinder's bottom ($j = 1$). If the eigenmodes $|z_{1,2}| = 1$, then the solutions (2.22) describe extended bulk solutions. There are no edge solutions, if for any k_x,

$$\begin{aligned} &|z_1| < 1 < |z_2|, \quad \text{or} \\ &|z_2| < 1 < |z_1|. \end{aligned} \quad (2.25)$$

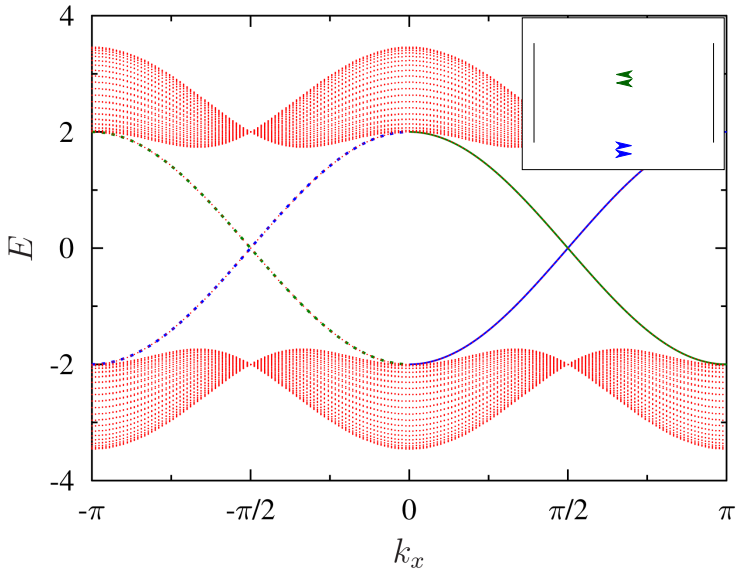

Fig. 2.2: Energy spectrum as a function of momentum k_x on a cylindrical geometry (height 40 sites and circumference 180 sites). Two edge states located near $j = 1$ are represented in blue, and two at $j = 40$ in green. The position and chirality of the edges is schematically represented in the inset.

In this case all solutions (2.22) diverge for $j > 1$. Manifestly, the same conclusions apply to the top edge.

Edge solutions can exist when both z_1 and z_2 are simultaneously smaller or greater than one. Note however that it is not possible to encounter a localized solution ψ^{+b} and ψ^{-b} in the same range of k_x. This is because if one is localized, then the other one has diverging eigenmodes z. This indicates that if $\psi^{\pm b}$ is a localized solution in a given k_x range, then $\psi^{\mp t}$ is a localized top solution.

Hence there are a maximum of two wave function solutions for a given edge. For $\mathcal{C} = 1$, only one of the solutions $\psi^{\pm b}$ holds in the BZ and the other is diverging away from the edge. For $\mathcal{C} = 2$, both solutions $\psi^{\pm b}$ are possible in distinct ranges of k_x.

Note that the energy dispersion always crosses the zero energy at $k_x = \pm\pi/2$. At a given edge, if there are two solutions, then they are associated either to $k_x = \pi/2$ or $k_x = -\pi/2$. This answers the question: what quantum number distinguishes the edge state solutions for $|\mathcal{C}| = 2$? Any edge state can be indexed a "valley" quantum number $\pm\mathbf{K}$ corresponding to a zero crossing at $\pm\pi/2$.

The existence conditions and the respective valid edge wave functions are given by the following inequalities:

$$\begin{aligned} &|z_1| < 1, |z_2| < 1, && \psi_j^{+b} \text{ and } \psi_j^{-t}, \\ &|z_1| > 1, |z_2| > 1, && \psi_j^{-b} \text{ and } \psi_j^{+t}. \end{aligned} \tag{2.26}$$

Let us illustrate the above results for a special point $t_1 = 1, t_2 = 1, t_3 = 0, m = 0$

of the phase diagram in Fig. 1.5. This point corresponds to the "center" of the $\mathcal{C} = -2$ phase and is characterized by the largest gap and flattest bands for the spectrum of the bulk states. One can expect two edge states at either end of the cylinder. The eigenmodes z are determined from Eq. (2.20)

$$z_{1,2} = \pm i \frac{\sqrt{(-i + e^{ik_x})(-i + e^{-ik_x})}}{-i + e^{ik_x}}. \tag{2.27}$$

The penetration length for the edge states is given by

$$\begin{aligned} \xi &= -1/\ln(|z_{1,2}|), \\ &= \frac{4}{\ln[1 + \sin(k_x)] - \ln[1 - \sin(k_x)]}. \end{aligned} \tag{2.28}$$

In this case the edge states have maximal extension and cover the entire BZ, because the existence condition (2.26) is always respected except at points $k_x = 0$ and $k_x = \pi$. At these particular points the edge states enter the bulk.

The above arguments allow to readily obtain the four edge state solutions in the $\mathcal{C} = -2$ phase for $t_1 = t_2 = 1$ and $m = t_3 = 0$. The wave functions and the respective energies read

$$\begin{aligned} \psi_j^{-\mathbf{K}b} &= c_+(1 - (-1)^j)\rho_1^j |x+\rangle, & E &= 2\cos(k_x), & k_x &\in (-\pi, 0), \\ \psi_j^{\mathbf{K}b} &= c_-(1 - (-1)^j)\rho_1^{*-j} |x-\rangle, & E &= -2\cos(k_x) & k_x &\in (0, \pi), \\ \psi_j^{\mathbf{K}t} &= c_+(1 - (-1)^j)\rho_1^j |x+\rangle, & E &= 2\cos(k_x), & k_x &\in (0, \pi), \\ \psi_j^{-\mathbf{K}t} &= c_-(1 - (-1)^j)\rho_1^{*-j} |x-\rangle, & E &= -2\cos(k_x), & k_x &\in (-\pi, 0). \end{aligned} \tag{2.29}$$

The indices t and b indicate whether the edge states live close to the top ($j = L_y$) or the bottom ($j = 1$) part of the cylinder. The index $\pm\mathbf{K}$ designates edges states crossing the zero energy at $\pm\pi/2$ or, equivalently in this case, whether the solutions extended in the right, respectively left, half of the ($[-\pi, \pi]$) BZ. The coefficients $c_\pm$ are normalization coefficients which are not of interest here. The edge states' energy dispersion (2.29) are plotted in Fig. 2.2 together with the numerical solution in order to show their perfect agreement.

2.3 Extension: Edges in a $\mathbb{Z}_2$ insulator

The class A topological insulator that was constructed in the previous subsections can be easily transformed into a $\mathbb{Z}_2$ topological insulator in the symplectic class AII by imposing time-reversal symmetry (see Tab. 1). In the following, spin degrees of freedom are added and a QSH model is created from two copies of the $\mathbb{Z}$ insulator. The object of the present subsection is to follow the fate of the two chiral edge sates obtained at the interface of $|\mathcal{C}| = 2$ phases with the vacuum. Crucially, these states are not robust with respect to arbitrary one-particle, time-reversal invariant perturbations.

The most straightforward route to create the $\mathbb{Z}_2$ insulator is the one taken in Ref. [4]. A TRI model is constructed from a $\mathbb{Z}$ insulator model and its time-reversal copy, with opposite Chern number. If there are no terms coupling the two models, then any edge state predicted from one of the models will have a partner with opposite chirality from the other one. Let us add spin flavor and ensure that the spin s_3 Pauli matrix commutes with the Hamiltonian. Each of the spinless $\mathbb{Z}$ model, now represents a polarized spin up, respectively down model, and each edge state is spin polarized.

Suppose that the spin up component is described by Eq. (1.41), while the spin down one represents its time reversed copy. This yields the following 4-band Hamiltonian:

$$\begin{aligned} H(\mathbf{k}) = {} & 2t_1 \cos(k_x)\sigma_1 + 2t_1 \cos(k_y)\sigma_2 s_3 \\ & + [m + 2t_2 \cos(k_x + k_y)]\sigma_3 + 2t_3[\sin(k_x) + \sin(k_y)]\sigma_3 s_3, \end{aligned} \tag{2.30}$$

where s Pauli matrices represent electronic spin, and σ, the orbital degrees of freedom.

Because the spin Hamiltonian is created from two copies of the spinless Hamiltonian, with no spin mixing terms, the conditions for the energy gap are not changed. That means the previously found insulating phases remain insulating for the four-band model.

On a cylindrical geometry, there are edge states forming around the edges of the cylinder. Because there are no spin mixing terms, the energy spectrum is trivially obtained by "doubling" the spectra already found for the spinless Hamiltonian. More precisely it is obtained from the union of the spinless (now spin up) Hamiltonian spectrum and its reflection about $k_x = 0$ under TRS. Therefore the number of edge states will also double such that each original edge state will get a Kramers partner.

Although every previously nontrivial Chern phase will show edge states in the spinful model, not all of them are robust. Indeed, the QSH insulator constructed from of the spinless model with $|\mathcal{C}| = 2$ allows one-particle TRI perturbations that destroys the edge states [6, 61].

A small TRI perturbation gaps the edge states at the crossing point $\mathbf{k}_x = \pm\pi/2$. Hence it is sufficient to analyze the system near the crossings to find such a perturbation. The low-lying edge states are described by an effective Hamiltonian, obtained by linearizing the solutions (2.29) near crossings $k_x = \pm\pi/2$. At a given edge, for the phase with $|\mathcal{C}| = 2$, this yields:

$$\begin{aligned} H_{\text{eff}}(q_x) = {} & \Psi^\dagger_{\mathbf{K}R\uparrow} v q_x \Psi_{\mathbf{K}R\uparrow} + \Psi^\dagger_{-\mathbf{K}R\uparrow} v q_x \Psi_{-\mathbf{K}R\uparrow} \\ & - \Psi^\dagger_{-\mathbf{K}L\downarrow} v q_x \Psi_{-\mathbf{K}L\downarrow} - \Psi^\dagger_{\mathbf{K}L\downarrow} v q_x \Psi_{\mathbf{K}L\downarrow}, \end{aligned} \tag{2.31}$$

where Fermi velocity reads $v = 2t_1$. The indices of the fermionic creation and annihilation operators $\Psi^\dagger$ and Ψ describe the valley ($\pm\mathbf{K}$), the direction of motion (L or R) and that of spin ($\uparrow$ or $\downarrow$). Note also that the first two terms in H_{eff} describe the dynamics of spin up electrons, and therefore correspond to the original 2-band Hamiltonian, while the spin down terms stem from of time reversal operator $\mathfrak{T}$; $\mathfrak{T}\Psi_{\mathbf{K}R\uparrow}\mathfrak{T}^{-1} = \Psi_{-\mathbf{K}L\downarrow}$. The locking between the direction of the spin and that of motion means that H_{eff} describes a helical liquid [61].

The edge states above are not robust because one can create the following one-particle, TRI, local perturbation that will gap the edge helical liquid in Eq. (2.31) (local meaning there is no inter-edge scattering)

$$\Psi^{\dagger}_{\mathbf{K}R\uparrow}\Psi_{\mathbf{K}L\downarrow} - \Psi^{\dagger}_{-\mathbf{K}R\uparrow}\Psi_{-\mathbf{K}L\downarrow} + \text{H.c.}. \tag{2.32}$$

It is possible to build many perturbations at the tight-binding level yielding the above form at low energy. It is noteworthy to observe that they all break the spin s_3 symmetry. An example of TRS perturbation in the tight-binding formulation is

$$t_4 \sin(k_x)\sigma_3 s_1. \tag{2.33}$$

For the phases with $|\mathcal{C}| = \pm 1$ no one-particle, local, TRI perturbation can result in backscattering of the edge states. The above example agrees with the statement that models with an even number of Kramers pairs of edge states are $\mathbb{Z}_2$-trivial [62].

2.4 Extension: Stripes of a $\mathbb{Z}$ insulator

There are still ways in which the Chern number computed analytically for a two-band model continues to be useful in multiband systems. Among the more simple ones is the "striped" topological insulator explored in the following.

Generally when two insulating phases with different Chern number are put in contact, there are edge modes that form between the phases. Consider now that one creates stripes from the same system with width of the order of the length of the unit cell. There are only two type of stripes, differentiated by parameter values (m, t_i). A new 2D system is constructed by alternating the two stripes, thus creating interfaces everywhere in the volume.

The natural supposition would be that if the parameters are associated with different Chern phases then there are edge states forming everywhere in the model. This turns out to be correct; the system becomes metallic with transport everywhere in the bulk in the direction of the edges. Let us study in more detail how the phases can be determined from an analysis of the phase diagram for each stripe Hamiltonian separately.

The model $|\mathcal{C}| = 2$ insulator in Eq. (1.41) is considered again. To simplify the problem, eliminate the $|\mathcal{C}| = 1$ phase by forcing $t_3 = 0$. Then the Hamiltonian reads

$$H = 2t_1 \cos(k_x)\sigma_1 + 2t_1 \cos(k_y)\sigma_2 + [m + 2t_2 \cos(k_x + k_y) + 2t_3(\sin(k_x) + \sin(k_y))]\sigma_3. \tag{2.34}$$

The Chern number that indexes the insulating phases reads

$$\mathcal{C} = \text{sgn}[-m - 2t_2] + \text{sgn}[m - 2t_2]. \tag{2.35}$$

In order to create the stripes, an alternating value for t_2 is introduced between two adjacent unit cells. In Fig. 2.3 are represented two of the cells and the striped model

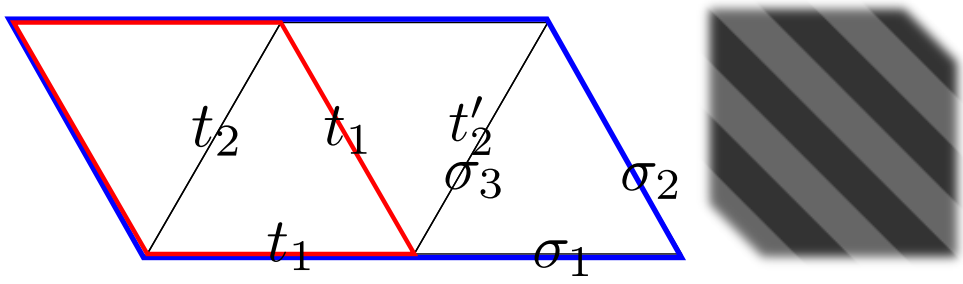

Fig. 2.3: The stripe model with alternating t_2 and t_2' hopping term. The red contour indicates the original unit cell. After the addition of t_2', the unit cell doubles its volume to the blue contour. The two orbitals with different on-site energy $\pm m$ are not represented; the Pauli matrices σ indicate the hopping integrals between orbitals along the three directions in the model.

which is obtained by repeating to infinity the pattern. The change is equivalent to doubling the size of the unit cell, which now contains t_2 and t_2' hopping terms. Hence in the stripe model there are four orbitals in the unit cell. A new set of of Pauli matrices τ are introduced to denote a "cell" degree of freedom.

Then the new Hamiltonian in momentum space reads

$$\begin{aligned} H = {} & 2t_1 \cos\left(\frac{k_x}{2}\right)\sigma_1\tau_1 + 2t_1\cos(k_y)\sigma_2\tau_1 \\ & + \left[m + (t_2 + t_2')\cos\left(\frac{k_x}{2} + k_y\right)\right]\sigma_3\tau_0 + (t_2 - t_2')\cos\left(\frac{k_x}{2} + k_y\right)\sigma_3\tau_3. \end{aligned} \tag{2.36}$$

Therefore the energy dispersion reads

$$E = a^2 + b^2 + c^2 \pm 2\sqrt{(a^2 + b^2)c^2}, \tag{2.37}$$

with

$$\begin{aligned} & a = 2t_1\sqrt{\cos^2(k_x/2) + \cos^2(k_y)}, \qquad b = m + (t_2 + t_2')\cos(k_x/2 + ky), \\ & c = (t_2 - t_2')\cos^2(k_x/2 + k_y)). \end{aligned} \tag{2.38}$$

Note that because the unit cell is doubled, the Brillouin zone shrinks by a factor of two. However, here k_x was rescaled such it continues to run from π to $-\pi$. Due to the folding of the BZ there are trivial solutions where the energy goes to zero, i.e. $(k_x, k_y) \in \{(0, \pm\pi/2), (\pi, \pm\pi/2)\}$. These points correspond to the edges of the metallic region. They correspond to $m = \pm 2t_2$ and $m = \pm 2t_2'$. But this lines in parameter space correspond exactly to the topological transitions between the topological phases for the

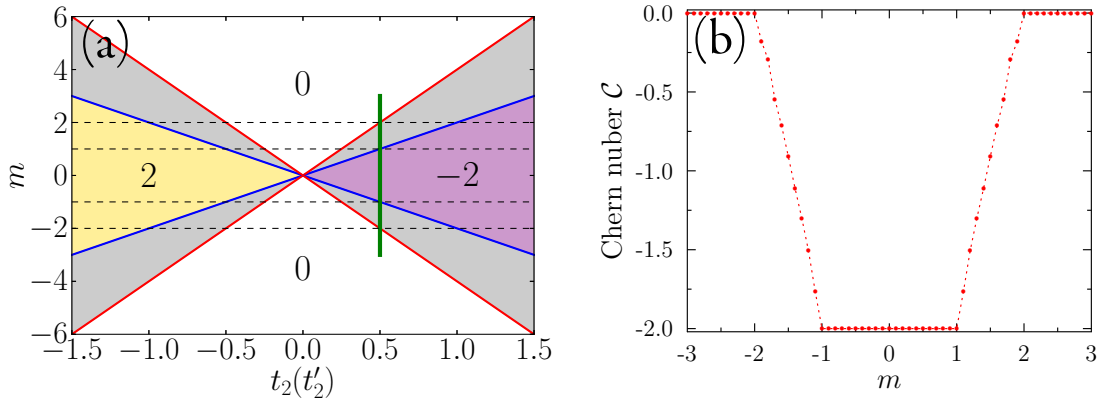

Fig. 2.4: (a) Superimposed phase diagram for each of the two stripe-Hamiltonian (one with t_2, the other with t_2') gives the complete phase diagram for the system. The Chern numbers index the (non)trivial phases according to Eq. 2.35. In grey is represented the metallic phase, where Chern number is exchanged at every stripe edge in the model. (b) Numerical Chern number calculation for the green line on the phase diagram (a), with $(t_2 = 0.5, t_2' = 1)$ and m varying in $[-3, 3]$. When the line crosses the metallic phase the Chern number is not defined; here this is seen as $\mathcal{C}$ taking fractional values between the well-defined $\mathcal{C} = 0$ and $\mathcal{C} = -2$ phases.

bulk Hamiltonian corresponding to the two stripes (see Eq. (2.35)). This solution indicates that, in order to determine the phase diagram of the model, it suffices to know the phase diagram for the two submodels.

When the two stripes are in the same connected topological phase, then no edge state are expected to appear between them. Therefore the overall system stays in the same gapped topological phase. Nevertheless, for disconnected phases described by the same index (for example, separated by a different phase), edge states might appear, rendering the system metallic. In every case where a Chern number is exchanged at the interface, edge channels will form, rendering the system metallic. Then the phase diagram can can be seen by superposing the phase diagrams for the submodels (see Fig. 2.4(a))

The above result is first tested by numerically computing the energy spectrum. This confirms the presence of metallic phases in the exact window predicted by the superposition argument that brought the diagram in Fig. 2.4(a). A more discerning investigation involves computing the Chern number for different parameters of the Hamiltonian.

At half-filling, there are two occupied (indexed by n) and two unoccupied bands (indexed by n'). Then the Chern number is determined numerically [17, 41]

$$\mathcal{C} = \frac{1}{2\pi} \int_{\mathrm{BZ}} d^2\mathbf{k}\, \Omega_{xy}(\mathbf{k}), \tag{2.39}$$

in terms of Berry curvature, Ω_{xy}, for the occupied bands

$$\Omega_{xy}(\mathbf{k}) = -2 \sum_{n \text{ occ.}} \sum_{n' \text{ unocc.}} \frac{\text{Im}[(v_x)_{nn'}(v_y)_{n'n}]}{(E_n - E_{n'})^2}, \tag{2.40}$$

where $(v_x)_{nn'}$ is expectation value of the velocity operator between one occupied and one unoccupied band

$$(v_x)_{nn'} = \langle n|\nabla_{k_x} H|n'\rangle. \tag{2.41}$$

For example, t_2 and t_2' are fixed, and m is varied in Fig. 2.4(b) to yield the expected values for the Chern number. Note that the Chern number is not well-defined in the metallic region. This is reflected in spurious fractional values between well-defined integer values (in the Fig. 2.4(b), $\mathcal{C} = 0$ and $\mathcal{C} = -2$).

In conclusion, the four-band model phases can be entirely determined from the original two-band model. This is not a surprise as the striped topological insulators is obtained from doubling the original model. In the case of the $\mathbb{Z}_2$ insulator, the doubling of the model kept all the gaps in the original model. However, in the striped topological insulators, if a edge state forms between two stripes as a consequence of disconnected topological phases, then the entire 2D model becomes metallic.

2.5 Discussion

The analytical methods in studying the edge states in topological insulators need further development. The encompassing generality in the description of bulk phases contrasts the short-sightedness of edge state investigations. For example, both methods used to compute the edge state solution took advantage of the fact that the 1D Schrödinger equation that describes the system connects only near-neighbor sites in the direction transverse to the edge. This is an artifact of the specific way in which the edge was cut. An open question remains how to adequately describe *generic* edge states in topological insulators. The decomposition effected in Chap. 1 of two-band models into gapless system plus a mass term gives hope that this could be used to describe such generic states. In perspective, it would take an extension of methods developed to study general edge states in graphene [63, 64] by considering now the role of the mass term.

A final word of caution is in order. Edge states can also exist between zones with identical Chern number. For example, in topologically *trivial* gapped graphene, edge states form at a domain wall due to a change in the on-site energy [65, 66]. The same effect was observed in simulations carried in Sec. 2.4, and led to the apparition of metallic phases when the stripes are created out of disconnected topological phases with the same Chern number. This surprising effect needs further investigation to check the robustness of the edge states. Moreover it adds a new level of difficulty in describing the physics of the edge states, because it drastically amends the rule of thumb that equals the number of edge solutions to the variation of the Chern number across an interface.

Part II

Majorana fermions

Chapter 3

Introduction

This introductory chapter contains a primer to Majorana fermions. First they are presented as real solutions to the Dirac equation. Secondly they emerge as quasiparticles in different condensed matter realizations. Among these, two one-dimensional systems are particularly relevant in the context of this thesis and therefore are presented in more detail: the Kitaev model [67] and the spin-coupled semiconducting wire supporting Majorana fermions in proximity of an s-wave superconductor [24, 25]. Finally, the chapter also includes a presentation of the concept of Majorana polarization as an order parameter to describe a topological transition.

3.1 Majorana fermion primer

3.1.1 Dirac equation and the Majorana condition

A fermionic particle that is its own antiparticle is a Majorana fermion [68]. For a solution, Ψ, to the Dirac equation, it is possible to define the antiparticle solution, Ψ_c, obtained under the charge conjugation operation. When the two are equal, they correspond to a Majorana particle.

Let us detail the charge conjugation operation by following Ref. [69]. The three-dimensional Dirac equation for a spin-$1/2$ particle in the presence of an electromagnetic field A_μ reads

$$(i\Gamma^\mu(\partial_\mu - ieA_\mu) - m)\Psi = 0. \tag{3.1}$$

The Greek indices run over the spatial $(1, 2, 3)$ and temporal (0) components, while the Roman indices run only over the spatial ones. The Γs are the 4×4 Dirac matrices and are conventionally chosen as

$$\Gamma_0 = \sigma_0 \otimes \tau_3, \quad \Gamma^j = i\sigma_j \otimes \tau_2, \tag{3.2}$$

where σ and τ are the usual 2×2 Pauli matrices. The Γ matrices obey the Clifford algebra

$$\{\Gamma^\mu, \Gamma^\nu\} = 2\eta_{\mu\nu}, \tag{3.3}$$

with $\eta_{\mu\nu}$ the Minkowski metric tensor, diag$(1, -1, -1, -1)$.

The charge conjugate solution Ψ_c will obey the same Dirac equation (3.1), but with opposite charge $-e$. That allows one to define the charge conjugation operator $\mathfrak{C}$, that yields the equation

$$\begin{aligned}\mathfrak{C}(i\Gamma^\mu(\partial_\mu - ieA_\mu) - m)\Psi &= (i\Gamma^\mu(\partial_\mu + ieA_\mu) - m)\mathfrak{C}\Psi, \\ &= 0,\end{aligned} \tag{3.4}$$

where $\mathfrak{C}\Psi = \Psi_c$. Note that the operator $\mathfrak{C}$ is anti-unitary and therefore must contain the complex conjugation operator K. It must also contain the only imaginary Γ matrix such that $[\mathfrak{C}, i\Gamma^\mu] = 0$. Hence the charge conjugation operator can be represented up to a global phase by

$$\mathfrak{C} = \Gamma^2 K. \tag{3.5}$$

Let us now consider the fulfilled Majorana condition, that a particle is identical to its antiparticle

$$\Psi_c \equiv \mathfrak{C}\Psi = \Psi. \tag{3.6}$$

Crucially this condition is Lorentz invariant and it is therefore valid in any reference frame [70]. Moreover, it is immediate from equation (3.1) that only a neutral spin-$1/2$ fermion can obey the condition, $e = 0$. Therefore both Ψ and Ψ_c are solutions to the same Dirac equation

$$(i\Gamma^\mu\partial_\mu - m)\Psi_{(c)} = 0. \tag{3.7}$$

The original Dirac spinor Ψ is a complex four-component spinor. Hence it is described by eight free real parameters. Under the Majorana condition four are fixed. For example, if the Dirac spinor is written as $\Psi^T = (\phi^T, \chi^T)$, with ϕ and χ two-component spinors, then the under Majorana condition

$$\Psi = \begin{pmatrix} \phi \\ \sigma_2\phi^* \end{pmatrix}. \tag{3.8}$$

Because ϕ is generally complex, a Majorana fermion has only four real components. Under a unitary transformation one can obtain purely real Majorana fermions, where each of its four components is real. This happens in a Majorana representation, where all the Γ matrices, not only Γ^2, are imaginary. Here the charge conjugation becomes complex conjugation and Majorana condition emerges as a strict reality condition

$$\Psi = \Psi^*. \tag{3.9}$$

A possible choice for a Majorana basis is

$$\Gamma^0 = \sigma_2 \otimes \tau_1, \quad \Gamma^1 = i\sigma_3 \otimes \tau_0, \quad \Gamma^2 = -i\sigma_2 \otimes \tau_2, \quad \Gamma^3 = -i\sigma_1 \otimes \tau_0, \tag{3.10}$$

with Γs that continue to obey the Clifford algebra.

Although Majorana particles are theoretically valid solutions to the Dirac equation, they have never been found among the fundamental particle. To this moment the neutrino remains an open possibility as a massive Majorana particle.

3.1.2 Particle-hole symmetry

In recent years, the idea of a Majorana fermion was resurrected in the context of condensed matter where it could be realized as a quasiparticle in a superconductor [71]. Intuitively it is natural to search in a superconductor because quasiparticle excitations contain both particle and hole degrees of freedom. A hole is simply the "antiparticle" of an electron.

In the language of creation and annihilation operators, the charge conjugation operation discussed previously is simply the operation of taking the Hermitian conjugate. That follows because creating an electron is identical to destroying a hole with opposite momentum.

At mean field level, the Hamiltonian for a superconductor in the second quantification reads [13]

$$H = \frac{1}{2} C^\dagger \mathcal{H} C, \tag{3.11}$$

with $C^\dagger = (\underline{c}^\dagger, \underline{c})$ and $\underline{c}$ is a row (or column, depending on context) vector comprising the annihilation operators at all the lattice sites in a superconductor, eventually with a spin index ($c_\uparrow$ or $c_\downarrow$). The "first-quantized" Bogoliubov-de Gennes Hamiltonian reads

$$\mathcal{H} = \begin{pmatrix} \mathcal{H}_0 & \Delta \\ \Delta^\dagger & -\mathcal{H}_0^* \end{pmatrix}, \tag{3.12}$$

where Δ is the matrix containing the superconducting order parameters. The action of the charge conjugation transformation is to convert a particle into a hole and vice versa

$$\mathfrak{C} c \mathfrak{C}^{-1} = c^\dagger. \tag{3.13}$$

The Hamiltonian exhibits the charge conjugation symmetry

$$[\mathfrak{C}, H] = 0. \tag{3.14}$$

Together with the Hermiticity of $\mathcal{H}$, it is sufficient to determine the consequences of charge conjugation symmetry on the BdG Hamiltonian,

$$\mathfrak{C} \mathcal{H} \mathfrak{C}^{-1} = \tau_1 \mathcal{H} \tau_1 = -\mathcal{H}^*, \tag{3.15}$$

where τ are the usual Pauli matrices acting in particle-hole space. This allows to define a particle-hole symmetry represented by an anti-unitary operator $\mathfrak{C}'$ that anticommutes with the Hamiltonian. Note that it is not a proper symmetry, due to the anticommutation

$$\{\mathfrak{C}', \mathcal{H}\} = 0, \quad \text{with } \mathfrak{C}' = \tau_1 K, \tag{3.16}$$

and K the complex conjugation operator. The consequence of this property is that any eigenstate of the BdG Hamiltonian has a particle-hole conjugate with opposite energy. That is, the presence of the PHS immediately reflects itself as redundancy in the solutions to the BdG equations. For example, take the Schrödinger equation

$$\mathcal{H}\Psi = E\Psi, \quad \Psi^T = (u^T, v^T), \tag{3.17}$$

where u (v) stands for the particle (hole) component of the wave function. The solutions describe the quasiparticles excitations above the BCS ground state. Then if (u^T, v^T) is the solution with energy E, then $(v^\dagger, u^\dagger)$ is the particle-hole conjugate with energy $-E$. In contrast, a quasiparticle solution is a Majorana fermion if it is equal to its own particle-hole conjugate (anti-quasiparticle), *at the same energy*. This implies that a Majorana fermion can be realized only at zero energy.

A solution to the mean-field equation can also be represented by a quasiparticle creation operator

$$\gamma_E^\dagger = \sum_j u_{j,E} c_j^\dagger + v_{j,E} c_j, \tag{3.18}$$

where j runs over all the sites (orbitals, and spins) in the superconductor. Then the particle-hole and Majorana conditions can also be concisely expressed as

$$\gamma_E = \begin{cases} \gamma_{-E}^\dagger, & \text{PHS condition,} \\ \gamma_E^\dagger, & \text{Majorana condition.} \end{cases} \tag{3.19}$$

Trivially both conditions are satisfied at zero energy for $u_{j,0} = v_{j,0}^*$.

It is not always possible to impose the Majorana conditions for the zero modes in superconductors. In a spin-singlet superconductor, an excitation has the structure [72]

$$\gamma_\alpha^\dagger = \sum_j u_{j,\alpha} c_{j,\alpha}^\dagger + v_{j,-\alpha} c_{j,-\alpha}, \tag{3.20}$$

where α is a spin index $\uparrow$ / $\downarrow$. Now j runs only over the site and orbital degrees of freedom. The Majorana condition reads $\gamma_\alpha^\dagger = \gamma_\alpha$, and the quasiparticle and the anti-quasiparticle contain different electron and hole creation operators. Hence, no matter the value of the coherence factors $(u_{j\alpha}, v_{j\alpha})$, it is not possible to create a Majorana fermion.

In conclusion, a spin-singlet superconductor does not allow naturally the formation of Majorana fermions. Nevertheless, there are ways to create Majorana fermions using spin-singlet superconductivity in concert with different ingredients that will be enumerated afterwards. However up to now, the presence of superconductivity stands out as a necessary condition for finding Majorana fermions in condensed matter. The mechanism involves always finding a quasiparticle that is its own antiparticle.

By inverting the relation (3.20), one can express the regular creation and annihilation operators in terms of Majorana fermions. This decomposition is generally available and resembles the representation of a complex number using two real numbers, its imaginary and real parts. Throughout this thesis the following representation of a creation operator is used

$$c^\dagger = \frac{e^{i\theta/2}}{\sqrt{2}}(\gamma_1 - i\gamma_2), \tag{3.21}$$

where the angle θ is an arbitrary degree of freedom in defining the Majorana fermions. Therefore the Majorana fermions obey the Clifford algebra

$$\{\gamma_A, \gamma_B\} = \delta_{A,B}, \tag{3.22}$$

where $\delta_{A,B}$ is the Kronecker symbol and A, B are Majorana indices, 1 or 2. Moreover, unlike complex fermions, Majoranas do not square to zero, but $\gamma_{1,2}^2 = \frac{1}{2}$.

Let us couple two Majorana fermions, γ_1 and γ_2. Working in the basis of the eigenstates of γ_1 and γ_2, the coupling $2i\gamma_1\gamma_2$ will act as a Pauli σ_2 matrix with eigenvalues ± 1 [73]. The occupation number of the fermionic operator created from the Majoranas then reads

$$c^\dagger c = \frac{1}{2} + i\gamma_1\gamma_2. \tag{3.23}$$

Therefore the occupation number $c^\dagger c$ is either 0 or 1. In the limit of a very weak coupling ε between the Majorana fermions (for example they can be located far away), they can still create a nonlocal fermionic state that is either full or empty. For vanishing coupling, $\varepsilon \to 0$, the ground state is effectively degenerate, and it costs ε to fill or empty the fermionic state. Therefore if the system contains $N\gamma_1$ and $N\gamma_2$ Majoranas, the ground state degeneracy will then be 2^N. Systems with such a highly degenerate state were proposed in Ref. [71], where the Majorana fermions are trapped in vortex cores of 2D $p+ip$ superconductor. Moreover, interchanging the Majorana fermions through a continuous adiabatic process generates a different ground state wave function that depends on the precise trajectory taken by the vortices. This dependence on the topology of paths taken by the vortices indicates the non-Abelian character of the ground state.

One of the main interest in finding Majorana fermions lies in using the highly degenerate ground state to store information. Then computations can be realized on it by taking advantage of its non-Abelian character and the protection of Majorana fermions. The catalog of operations on the ground state form a representation of the braid group [74]. The goal of this research is to finally realize a topological quantum computer [73].

3.2 Condensed matter realizations

3.2.1 Overview

The reader is referred to excellent reviews that provide a good panorama of the research on Majorana fermions in condensed matter systems [75, 76]. Here it suffices to mention a few milestone in the evolution of the field.

As seen before, in condensed matter physics Majorana fermions can be realized as quasiparticles in spinless or triplet-pairing superconductors. They are possible as zero energy excitations in systems with particle-hole symmetry.

Naturally they were first proposed in 2D $p + ip$ superconductors [71], where they could be realized as bound modes in the vortices of the superconductor. A 1D variation was soon after treated by Kitaev [67], where Majorana states in a spinless tight-binding model appear as bound states at the ends of the wire. Different proposals followed these two paths: boundary states in p-wave superconductors or Caroli-de Gennes-Matricon states [77], where the Majorana fermion appear when a a magnetic flux penetrates a type II p-wave superconductor. Other materials in which Majorana fermions are thought to appear are 2D electron gases in the fractional Hall regime at $5/2$ filling factor [78], and two-dimensional strontium ruthenate, Sr_2RuO_4 [79] (and [80] for experiments). They were also proposed to form in p-superfluids in ultracold atom gases [81, 82]

The problem with the 2D p-wave superconductors is that they are rare materials. Moreover, for the case of Majorana states bound to vortices, there are more excited states within the bulk gap rendering fragile the protection of the zero modes [76].

A revolution of the field came when it was realized that one can replace the p-wave superconductors with s-wave superconductors and one can have an effective p-wave superconducting pairing mediated through s-wave pairing. The first example was proposed in Ref. [83]. There Majorana end states appear in a 2D topological insulator deposited on an ordinary s-wave superconductor. The chiral edge states in the topological insulator can be coupled through the s-wave pairing such that inside the gap one can have a pair of Fermi points (or more precisely an odd number in half the BZ) and an effective p-wave pairing. Numerous proposals have followed which are using topological insulators and superconductors as a basic setup for creating Majorana excitations [84, 85]. Some of the experiments following the theoretical proposals are reported in Ref. [86].

Nevertheless, topological insulators remain exotic materials. More recently, proposals have emerged where topological insulators are replaced by regular semiconducting wires with a strong-spin orbit coupling under a magnetic field [24, 25, 87]. They are one of the main subjects of the thesis and they will be described in more detail in the next sections. Several articles expanded on this direction, in semiconducting quantum wells [88], or in multiband spin-orbit coupled wires [89, 90]. Experiments in these directions were pursued by several groups [91, 92]. There are also variations to these systems which dispense with the spin-orbit coupling [93, 94].

Let us finally note the prediction of Majorana fermions in non-centrosymmetric su-

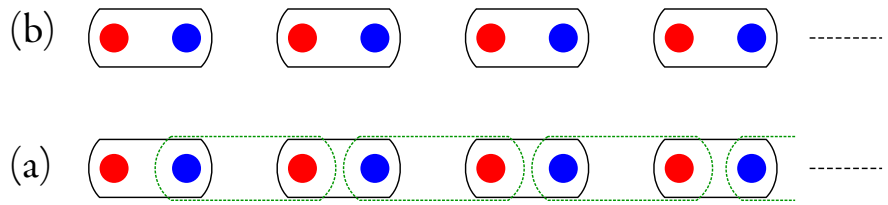

Fig. 3.1: Two topological phases of the Kitaev model. The red and blue denote two Majorana fermions that compose a regular complex fermion, represented in black. (a) Trivial phase where the Majoranas are coupled inside each site. (b) Nontrivial phase where Majorana in adjacent sites hybridize to form a complex electron. Unpaired zero modes are left at the end of the wire.

perconductors [95, 96] and or in ultracold atomic gases with s-wave superconductivity [97].

For the detection of the Majorana modes the principal directions are: interferometry [98, 99], measuring nonlocal tunneling [100, 101], fractional Josephson effect [67, 102], the detection of zero bias conductance peak [103, 104], etc.

3.2.2 Kitaev model

The present thesis is limited to the study of phenomena related to Majorana fermions arising in one dimensional systems. The following Kitaev model inescapably arises as a paradigm for 1D systems supporting Majorana fermions. Therefore it is worthy to probe it in more detail.

The model was proposed in Ref. [67] and it is captured by the tight-binding Hamiltonian

$$H = \sum_{j=1}^{N} (1/2 - c_j^\dagger c_j)\mu + (-t c_j^\dagger c_{j+1} + \Delta c_j c_{j+1} + \text{H.c.}), \tag{3.24}$$

where j runs over all the sites N of a *finite* lattice. It is a 1D toy model describing spinless electrons that experience a superconducting pairing Δ, treated at the mean-field level; μ is the chemical potential and t is the hopping strength. It was argued that such system can present Majorana, zero energy states bound at the two ends of the wire. This work was motivated by the search of a qubit that is protected with respect to perturbations. The qubit is formed by the two entangled Majorana states. Nevertheless, the interest in the following will be centered on the conditions and the description of the topological phase.

The Majorana fermions exist as quasiparticle excitations and that explains the need for superconductivity. The system is spinless, yielding essentially a p-wave superconductor, with the quasiparticles γ obeying the reality (Majorana) condition $\gamma = \gamma^\dagger$. Moreover the system has a bulk gap that protects eventual zero energy modes.

Through a gauge transformation, the phase of the superconducting parameter can be absorbed in the definition of the creation and annihilation operators. For $\Delta = |\Delta|e^{i\varphi}$ the complex superconducting, the new operators are chosen such that

$$c_j e^{i\varphi/2} \to c_j. \tag{3.25}$$

Then, without loss of generality, Δ is chosen here to be a real positive quantity.

Any fermionic Hamiltonian supports a rewriting in terms of Majorana fermions:

$$\begin{aligned}\gamma_1 &= \frac{1}{\sqrt{2}}(c^\dagger + c),\\ \gamma_2 &= \frac{i}{\sqrt{2}}(c^\dagger - c).\end{aligned} \tag{3.26}$$

Thus any complex fermion is formally split into two Majorana fermions.

Then the Hamiltonian has the form

$$H = i\sum_{j=1}^{N} \mu\gamma_2^j\gamma_1^j + \left[(\Delta - t)\gamma_1^j\gamma_2^{j+1} + (\Delta + t)\gamma_2^j\gamma_1^{j+1}\right]. \tag{3.27}$$

The resulting tight-binding Hamiltonian can present bound states that consist in having a zero mode Majorana fermion trapped at each edge. For example, a limit case follows for $\mu = 0$ and $\Delta = t$, when the Hamiltonian reduces to

$$H = 2it\sum_{j=1}^{N} \gamma_2^j\gamma_1^{j+1}, \tag{3.28}$$

and Majorana fermions are coupled only between neighboring sites. Then two unpaired Majorana fermions remain at the ends of the chain, γ_1^1 and γ_2^N (see Fig. 3.1(b)). They are completely localized at the extremity sites and have zero energy as they are decoupled from the Hamiltonian. However there will be a residual interaction between the end modes, rapidly decreasing with the length aN of the wire $O(e^{-aN/\xi})$, where ξ is the superconducting coherence length and $a = 1$, the lattice constant. Note that in the absence of the hopping t and the superconducting pairings Δ, the Hamiltonian couples only Majoranas on the same site. This latter limit case represents a trivially gapped system, an atomic insulator.

The zero modes, protected by the bulk gap and the PHS, subsist at zero energy when parameters begin to vary from the values set above. They will start to extend, but they will remain Majorana fermions. The topological phase can be empirically tracked by knowing where the bulk gap closes in parameter space and if there are such exotic bound states in between two bulk closings.

The topological phase was characterized by a $\mathbb{Z}_2$ topological invariant denoted by $\mathcal{M}$ in Ref. [67]. If the wire supports Majorana fermions, then $\mathcal{M} = -1$, and, if the system is in a trivial gapped phase, then $\mathcal{M} = 1$. When the bulk gap closes, $\mathcal{M}$ is undefined.

Any free fermionic Hamiltonian can be written in the basis of Majorana fermions as

$$H = \frac{i}{2}\sum_{m,n} A_{m,n}\gamma_1^m\gamma_2^n, \tag{3.29}$$

where A is a real, anti-symmetric matrix (due to the anticommutation of Majorana fermions). The way to characterize the topological properties of the system involves (anti)-periodizing the system in a ring form. Then the topological invariant was shown [67] to be given by

$$\mathcal{M}(\mathcal{H}) = \text{sgn}(\text{Pf}[A^p]\text{Pf}[A^a]), \tag{3.30}$$

where $A^{p,a}$ represents the system with periodic, respectively antiperiodic, boundary conditions and Pf denotes the Pfaffian of the matrix.

There is an alternative way to characterize the topology of the system. Note that the system is time-reversal invariant in the class of chiral one-dimensional BDI systems (see Tab. 1). As such, the system equally supports a characterization by a winding number w.

The system is made infinite such that there is translational invariance. Hence momentum k remains a good quantum number. The Hamiltonian is Fourier transformed in momentum space, so that in the basis $C_k^\dagger = (c_k^\dagger, c_{-k})$ it reads

$$H = \frac{1}{2}\sum_k C_k^\dagger \mathcal{H} C_k. \tag{3.31}$$

The BdG Hamiltonian without the constant $\sum_j \mu/2$ takes the form

$$\mathcal{H} = \begin{pmatrix} -\mu - 2t\cos k & -2i\Delta\sin k \\ 2i\Delta\sin k & \mu + 2t\cos k \end{pmatrix}. \tag{3.32}$$

The bulk energy dispersion reads

$$E_\pm = \pm\sqrt{(\mu + 2t\cos k)^2 + 4|\Delta|^2\sin^2 k}. \tag{3.33}$$

Therefore the bulk gap closes for $k = 0$ and $\mu = -2t$, or $k = \pi$ and $\mu = 2t$.

The Hamiltonian can be expanded in a basis of particle-hole Pauli matrices τ

$$\mathcal{H} = h_2\tau_2 + h_3\tau_3, \tag{3.34}$$

with $h_2 = 2\Delta\sin k$ and $h_3 = -\mu - 2t\cos k$. Note that the system obeys the TRS, represented by the operator of complex conjugation K and the chiral symmetry, represented by the operator τ_1. Also note that the unit vector Hamiltonian, $\hat{\mathbf{h}}$, is a mapping

from the one dimensional torus T^1 to the circle S^1. Therefore the behavior of $\mathbf{h}$ can be characterized by a winding number w (see also Sec. 6.1.2)

$$\begin{aligned} w &= -\frac{1}{2}\sum_{k\in\{0,\pi\}} \text{sgn}[h_3\partial_k h_2], \\ &= \frac{1}{2}(\text{sgn}[2t-\mu]+\text{sgn}[2t+\mu]), \end{aligned} \tag{3.35}$$

where the sum was performed over the nodes of the dispersion ($k=0$ and $k=\pi$). The winding number is either zero, for $|\mu|>2|t|$, and there are no edge states inside the gap, or one, for $|\mu|<2|t|$, and it is a Majorana bound state inside the gap.

This allows to relate the winding number to the $\mathcal{M}$ topological index:

$$\mathcal{M} = \begin{cases} -1, & |\mu|<2|t|, \\ 1, & |\mu|>2|t|, \end{cases} \tag{3.36}$$

where $\mathcal{M}=1$ denotes that the trivial strong-pairing phase and $\mathcal{M}=-1$, the weak-pairing phase (the topological phase) [76].

Note that because the system is described by a $\mathbb{Z}$ invariant, it could sustain multiple Majorana modes at a given edge. The fact that there there are only two topological phases is entirely due to the fact that it involves only nearest-neighbor couplings. Chap. 6 treats an extension of the Kitaev model in the BDI class, with distant-neighbor couplings, which exemplifies a case with winding number higher that one, $|w|=2$ and two Majorana modes at a given edge.

A different evaluation of the topological invariant $\mathcal{M}$ is given by [24, 67]

$$\mathcal{M} = (-1)^{\nu(\pi)-\nu(0)}, \tag{3.37}$$

where $\nu(k)$ is the number of negative eigenvalues of $\mathcal{H}$ at the k point. Here $[0,\pi]$ is half the BZ and then $\nu(\pi)-\nu(0)$ is the number (mod 2) of Fermi points in half-BZ. This definition relies on the existence of the PHS symmetry that ensures that the other half of the BZ has the same number of Fermi points.

Therefore the conditions to have Majorana fermions in the system are, up to now: having a spinless or spin-triplet superconductor, a bulk gap, and an odd number of Fermi points in half the BZ.

3.2.3 1D spin-coupled semiconducting wire in proximity to an s-wave superconductor

The Kitaev toy model needs to be implemented in a more realistic setting. Among different proposals a special attention is given in the present thesis to one which uses a 1D spin-coupled semiconducting wire in the proximity to an s-wave superconductor and under the effect of a magnetic field to realize Majorana end modes [24, 25]. Such model

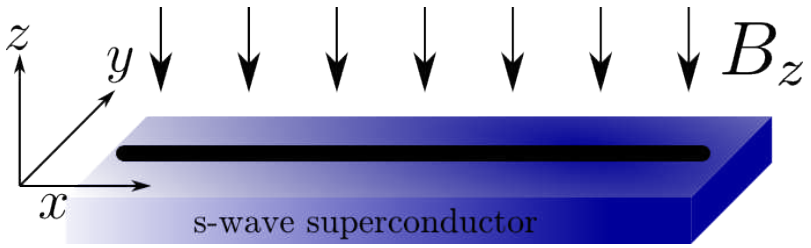

Fig. 3.2: Schematic setup for a 1D system supporting Majorana fermions. Semiconducting wire (black) with strong spin-orbit coupling deposited on a s-wave superconductor (blue). A magnetic field B_z acts in z direction, perpendicular to the wire.

has received a lot of attention in the experimental community due to the use of the simplest ingredients. Instead unconventional superconductors, it needs the more available s-wave singlet superconductors. Moreover, by using semiconductors, instead of topological insulators, it can take advantage of the tremendous experimental know-how in the fabrication and manipulation of semiconducting wires.

The race to experimentally discover Majorana fermions was purportedly ended when a zero-bias conductance signature was detected in a superconductor-normal system that is based on the aforementioned model [91]. However, recent doubts have been raised, claiming that a robust zero-bias signature can be due to the presence of disorder [105, 106] or Kondo resonances [107].

In the present section, the system and its phases will be presented more on a phenomenological level. The next chapter treats a direct extension of the model when a Dresselhaus spin-orbit coupling is included. That will be the place for a more detailed analytical and numerical treatment.

The system is described by the Hamiltonian (see also [108])

$$H = \int dx \left[\psi^\dagger \left(\frac{p^2}{2m} - \mu + \alpha p \sigma_2 + B_z \sigma_3 \right) \psi + (\Delta \psi_\uparrow \psi_\downarrow + \text{H.c.}) \right], \tag{3.38}$$

where σ are the Pauli spin matrices. This Hamiltonian models a 1D semiconducting wire extended in the x-direction at chemical potential μ (see Fig. 3.3). The wire experiences a proximity effect due to the presence of the s-wave superconductor. These leads to superconducting correlations inside the wire, which are expressed at mean-field level by the presence of the superconducting parameter Δ. There is also Rashba spin-orbit coupling α which tends to align the spins in the y-direction. Finally there is a magnetic field B_z perpendicular to the spin-orbit field. All these elements are necessary to reproduce at low energy the Kitaev model. First it is necessary to lift the spin degeneracy to allow for the possibility of an odd number of Fermi points. Let us see how this happens by studying the bulk energy dispersion.

Due to the presence of the anomalous pairings $\psi_\uparrow \psi_\downarrow$ one can write the Hamiltonian

in a BdG form

$$H = \frac{1}{2}\int \Psi^\dagger \mathcal{H} \Psi dx, \quad \Psi^\dagger = (\psi_\uparrow^\dagger, \psi_\downarrow^\dagger, \psi_\downarrow, -\psi_\uparrow),$$
$$\mathcal{H} = \left(\frac{p^2}{2m} - \mu + \alpha p \sigma_2\right)\tau_3 + B_z\sigma_3 - \Delta\tau_1, \tag{3.39}$$

where τ are the Pauli matrices in particle-hole space. By squaring twice the Hamiltonian $\mathcal{H}$ it follows that the bulk energy reads

$$E^2 = \xi_p^2 + \alpha^2 p^2 + B_z^2 + \Delta^2 \pm 2(\xi_p^2\alpha^2 p^2 + \xi_p^2 B_z^2 + \Delta^2 B_z^2)^{1/2}, \tag{3.40}$$

with $\xi_p = p^2/2m - \mu$. Due to the particle-hole symmetry, any state at energy E has a counterpart at $-E$. Also any state with momentum p has a counterpart with the same energy and opposite momentum. Because of this redundancy, it suffices to analyze the first quadrant ($E > 0$ and $p > 0$) of the dispersion in Eq. (3.40). Without loss of generality μ can be set to zero in the following.

For vanishing magnetic field and superconducting correlations, $B_z = \Delta = 0$, the spin y states $|y\pm\rangle$ are good eigenstates of the system. Hence the spin-orbit coupling yields two shifted parabolas for the dispersion for the two spins (see Fig. 3.3(a)). However the system still needs to be gapped. The superconducting gap is not sufficient to generate Majorana fermions. This is because the system remains time-reversal invariant and therefore the gaps at $p = 0$ and $p = p_F$ (Fermi momentum) are identical. Then for every energy, there will be an even number of Fermi points for $p \in [0, \infty)$. Therefore it is necessary to break the time reversal invariance by adding a magnetic field B_z, which gaps the system at $p = 0$ (see Fig. 3.3(b)).

Note that there are two gaps in the system. One at Fermi momentum, which is proportional to the induced gap $\Delta(p_F) \propto \Delta$, and a gap at $p = 0$, $\Delta(0) = B_z - \sqrt{(\mu^2 + \Delta^2)}$. Crucially the gap at $p = 0$ can change its sign. When the Zeeman energy dominates the superconducting gap, the gap at $p = 0$ and the gap at p_F are of of opposite type. This is the condition for the presence of Majorana fermions

$$B_z^2 > \mu^2 + \Delta^2. \tag{3.41}$$

The above condition is obtained rigorously from an analysis of topological invariants in the next chapter. It suffices to say that if $|\Delta| < |B_z|$ there is a range of μ for which the system is in the topological phase. This quantity can be changed by gating and one wishes to have a window as large as possible in the chemical potential. However the Zeeman field cannot be increased *ad lib* as it tends to destroy the Cooper pairs by polarizing the electrons in z-direction. Moreover, the breaking of the time reversal symmetry makes the system susceptible to disorder, which in turn can close the bulk gap [109]. A large SOC is needed to combat the effect of the magnetic field by enforcing the anti-alignment of electron spin with opposite momentum. However, the downside is that a large SOC suppresses the electron mobility [76, 110].

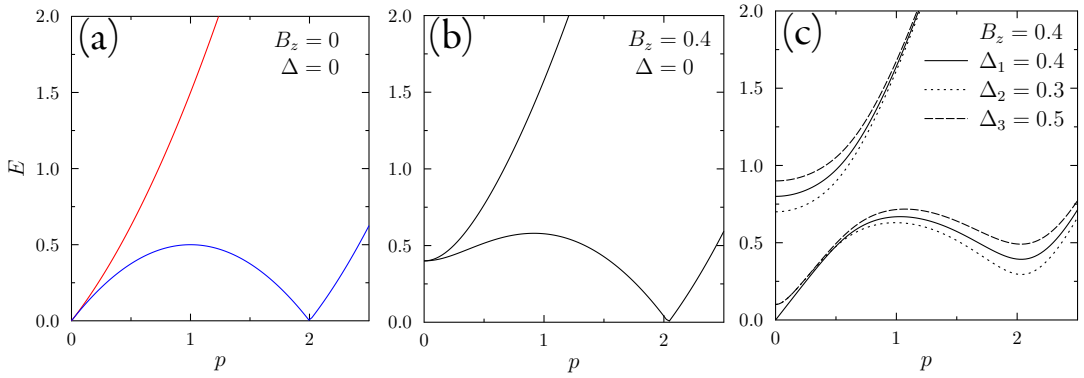

Fig. 3.3: A representation of the energy dispersion in the first quadrant for different values of magnetic field B_z and induced superconducting gap Δ. The mass m and the Rashba SOC α are set to 1, the chemical potential $\mu = 0$. (a) Shifted parabolas due to the SOC. The energy eigenstates have a clear spin direction: blue $\uparrow$ and red $\downarrow$. (b) Nonvanishing magnetic field opens a gap at momentum $p = 0$ allowing the possibility of an odd number of Fermi points. (c) Topological transition at $p = 0$ between two gapped phases, $\Delta = 0.3$ nontrivial, $\Delta = 0.5$ trivial, through closing of the gap when $B_z = \sqrt{\Delta^2 + \mu^2}$, corresponding to $\Delta = 0.4$.

Finally, it is necessary to clarify how can an s-wave superconducting pairing Δ mediate p-superconductivity. For that one works in the window provided by the topological condition in Eq. (3.41) [24]. Assuming that the superconducting parameter Δ is very small in comparison to B_z, one can diagonalize the Hamiltonian (3.38) to yield energy

$$E_\pm = \xi_p \pm \sqrt{B_z^2 + \alpha^2 p^2}, \tag{3.42}$$

and the two eigenvectors are

$$\psi_\pm = \frac{1}{N_\pm} \begin{pmatrix} B_z \pm \sqrt{B_z^2 + \alpha^2 p^2} \\ i\alpha p \end{pmatrix}, \tag{3.43}$$

where $N_\pm$ are chosen to normalize the spinors. The Fermi energy is between the two bands. Then the Hamiltonian with the superconducting pairing term can be projected on the lower band, and then one has access to the physics at the Fermi momentum. The Hamiltonian projected on the occupied band reads

$$\begin{aligned} H &= \int dp\, E_-\psi_-(p)\psi_-(p) + \big[\Delta_-(p)\psi_-(p)\psi_-(-p) + \text{H.c.}\big], \\ \Delta_-(p) &= \frac{i\alpha p\Delta}{2\sqrt{B_z^2 + \alpha^2 p^2}}. \end{aligned} \tag{3.44}$$

The effective pairing is an odd function in the momentum p, pairing particles in the same band with opposite momentum. Thus one has effective p-wave symmetry for spinless electrons induced through an s-wave superconducting pairing.

3.3 Majorana polarization

This final introductory section advances the notion of Majorana polarization [111]. The concept tries to answer the need for a *local* order parameter that can adequately describe the topological transition from a trivial gapped phase to a Majorana supporting gapped state. It will be used in the next chapters as a means to identify zero modes in spinful topological superconductors as Majorana states.

In short, the Majorana polarization amounts to having a measure of the degree of anomalous triplet pairing in the system. As it was shown in the previous sections, this unconventional pairing can be effectively produced even in semiconducting systems in proximity to a spin-singlet superconductor. Here superconductivity is treated only at the mean field level. If at the Fermi energy the system is effectively a triplet superconductor and there are zero modes protected by a bulk gap, then they are Majorana fermions. In this sense, Majorana polarization is an necessary (but not sufficient) condition for having Majorana fermions.

The Hamiltonian for a spinful 1D superconductor (or in proximity to a superconductor) is given by

$$H = \frac{1}{2}\int dx \Psi^\dagger \mathcal{H} \Psi, \quad \Psi^\dagger(x) = (\psi_\uparrow^\dagger(x), \psi_\downarrow^\dagger(x), \psi_\downarrow(x), -\psi_\uparrow(x)), \tag{3.45}$$

where $\psi_\alpha^\dagger$ is a creation operator for an electron with spin α. The Bogolibov-de Gennes equation at a particular point in a 1D system reads

$$\mathcal{H}\Phi(x) = E\Phi(x), \quad \Phi^\dagger = (u_\uparrow, u_\downarrow, v_\downarrow, v_\uparrow)^* \tag{3.46}$$

with u, v amplitudes for the electron, respectively hole, components of the wave function.

The BdG equation is a matrix equation where there are four degrees of freedom: spin $\uparrow, \downarrow$, particle and hole. Generally there are four eigenvectors and eigenvalues solutions to Eq. (3.46).

In this particular basis the PHS operator, which anticommutes with the Hamiltonian, is represented by $\sigma_2\tau_2 K$. Throughout σ are the Pauli matrices in the spin space and τ in the particle-hole space. Under the action of the particle-hole operator the wavefunction transforms as

$$\sigma_2\tau_2\Phi^*(E) = \Phi(-E). \tag{3.47}$$

Then the Majorana condition reads

$$\sigma_2\tau_2\Phi^*(E) = \Phi(E). \tag{3.48}$$

One can compute locally the overlap between any eigenvector and its particle hole conjugate at the *same* energy to see how close the wave function respects the Majorana condition. However, the particle hole operator is defined up to a phase which is not easily

determined in practical situations. Hence the focus is on the real part of the overlap $\Phi^T\sigma_2\tau_2 e^{-i\theta}\Phi^*$, which is generally a complex number. Let us consider this quantity as a vector that can be decomposed on the "Majorana" x-axis ($\theta = 0$) and y-axis ($\theta = \pi/2$). Then to identify the Majorana fermions one can take the real and imaginary parts of the overlap as polarizations along the two axis. The Majorana x- and y-polarizations are defined as

$$\begin{aligned} P_{M_x}(x) &= \mathrm{Re}[\Phi^T(x)\sigma_2\tau_2\Phi^*(x)], \\ P_{M_y}(x) &= \mathrm{Im}[\Phi^T(x)\sigma_2\tau_2\Phi^*(x)]. \end{aligned} \tag{3.49}$$

The Majorana polarization vector is then defined as the absolute value of the Majorana polarization vector

$$P_M(x) = |(P_{M_x}, P_{M_y})|. \tag{3.50}$$

Here the normalization from a Majorana solution is conventionally chosen such that the overlap integrated over the region where the zero mode is extended reads

$$\int dx P_M(x) = \frac{1}{2}, \tag{3.51}$$

which echoes the particular squaring of a Majorana fermion, $\gamma^2 = \frac{1}{2}$.

Explicitly, in terms of the wave function components, the Majorana polarization components are

$$\begin{aligned} P_{M_x} &= 2\mathrm{Re}[u_\downarrow v_\downarrow^* - u_\uparrow v_\uparrow^*], \\ P_{M_y} &= 2\mathrm{Im}[u_\downarrow v_\downarrow^* - u_\uparrow v_\uparrow^*]. \end{aligned} \tag{3.52}$$

Note that the definitions involve pairing of electrons and holes with the same spin, indicating a spin-triplet pairing in the model. Then a different way to think about the Majorana polarization is to see it as a measure of spin-triplet pairing in the model. Note that it is possible to have non-zero Majorana polarization, but a Majorana fermion exists only when its Majorana density integrates to $1/2$ (see Eq. 3.51) In the 1D spinful system that will happen at zero energy.

It is well suited to compare the Majorana polarization with usual operators used to investigate the local structure of wave function. Let us neglect for the moment the hole degrees of freedom. Then one can define familiar concepts as the local electronic density of states operator $\hat{\rho}(x)$ and the local spin polarization operator $\hat{\mathbf{S}}(x)$ at a given energy E as

$$\hat{\rho}(x, E) = \sum_{n=1}^{4} \Psi_n^\dagger(x) \left(\sigma_0 \otimes \frac{\tau_0 + \tau_3}{2} \right) \Psi_n(x) \delta(E - E_n), \tag{3.53}$$

and

$$\hat{\mathbf{S}}(x, E) = \sum_{n=1}^{4} \Psi_n^\dagger(x) \left(\boldsymbol{\sigma} \otimes \frac{\tau_0 + \tau_3}{2} \right) \Psi_n(x) \delta(E - E_n) \tag{3.54}$$

where n indexes the eigenvalue and the respective eigenfunction. Note that $\hat{\mathbf{S}}$ has a vector structure with components in x, y and z-spin direction.

In analogy the Majorana polarization operators can be defined from Eq. (3.52)

$$\hat{P}_{M_x}(x, E) = \sum_n \Psi_n^\dagger(x)\sigma_2 \otimes \tau_2 \Psi_n(x)\delta(E - E_n), \tag{3.55}$$

$$\hat{P}_{M_y}(x, E) = \sum_n \Psi_n^\dagger(x)\sigma_2 \otimes \tau_1 \Psi_n(x)\delta(E - E_n). \tag{3.56}$$

Note again that an electron (or hole) will always have zero Majorana polarization. Eq. (3.52) shows that the same is the case with wave functions with spin-singlet pairing of the type $(u_\uparrow, 0, v_\downarrow, 0)$. This brings more support to the idea that Majorana polarization measures a degree of spin-triplet pairing in the system.

Majorana polarization and density are not physical quantities that one can measure, but they can be used to give a picture of Majorana excitations at zero energy. Two zero modes with opposite Majorana polarizations provide a clear illustration to the fact that they are modes that can be "combined" to form a Majorana unpolarized electron (or hole). Two Majorana modes with the same polarization can coexist nearby, but tend to hybridize and form regular electronic states if their polarization is opposite. A rotation of Majorana polarization might be due to the variation of physical parameters as spin-obit coupling or the superconducting phase. These cases can pose a problem as the angle of rotation can be locally dependent and difficult to interpret. Then the absolute value of the polarization vector, the Majorana density (3.50) would be more suited to identify a wave function as Majorana.

Chapter 4

Topological semiconducting wire with Rashba and Dresselhaus spin-orbit coupling

This chapter reconsiders the 1D spin-orbit coupled semiconducting wire from Ref. [24, 25] with an additional Dresselhaus spin-orbit interaction. The wire supports Majorana modes that present a particular spin texture. The electronic degrees of freedom of the Majorana fermions have a transverse polarization to the magnetic field that is entirely determined by the direction of the spin-orbit coupling vector. They are always opposite at the two ends of the semiconducting wire. Already Majorana modes for two dimensional spin-triplet topological superconductors has been shown to exhibit an Ising-like spin density that may allow their detection via coupling to a magnetic impurity [112, 113]. In the same vein it is suggested that the spin texture in the 1D superconductor might be detected in a spin-polarized scanning tunneling microscopy experiment.

Furthermore, the Majorana polarization defined in Sec. 3.3 is shown to be a good order parameter to describe the topological transition in the model.

4.1 Model Hamiltonian

Let us consider a semiconducting wire oriented along the x-direction, and in proximity to an s-wave superconductor. Due to bulk inversion asymmetry, semiconducting wires can exhibit along with the Rashba SO interaction analyzed in Refs. [25, 87, 108], a Dresselhaus SO interaction [114].

In the present case, Dresselhaus SOI to first order in momentum p in the x-direction along the wire takes the form $\beta p\sigma_1$. The coupling β can be of the same order of magnitude with the Rashba SOC (~ 0.1 eV Å) [115]. The Hamiltonian describing the system reads

$$H = \int dx \left[\psi^\dagger \left(\frac{p^2}{2m} - \mu + \alpha p\sigma_2 + \beta p\sigma_1 + B_z\sigma_3 \right) \psi + (\Delta\psi_\uparrow\psi_\downarrow + \text{H.c.}) \right]. \quad (4.1)$$

The Pauli matrices σ represent spin. The identity matrices and the spin index for the fermionic field are implied when absent. The chemical potential is denoted by μ, B_z is the Zeeman field, Δ is the induced superconducting pairing and α (β) characterizes the magnitude of the Rashba (Dresselhaus) SO interaction.

Let us consider for the moment a purely real superconducting parameter Δ. Due to the presence of superconducting correlations, the Hamiltonian can be equally casted in a Bogoliubov-de Gennes form

$$\begin{aligned} H &= \frac{1}{2}\int dx \Psi^\dagger \mathcal{H} \Psi, \quad \Psi^\dagger = (\psi_\uparrow^\dagger, \psi_\downarrow^\dagger, \psi_\downarrow, -\psi_\uparrow), \\ \mathcal{H} &= \left(\frac{p^2}{2m} - \mu + \alpha p \sigma_2 + \beta p \sigma_1\right)\tau_3 + B_z\sigma_3 - \Delta\tau_1. \end{aligned} \tag{4.2}$$

Pauli matrices τ act in the particle-hole space. The products of Pauli matrices that live in different spaces should be understood as a tensor products. The BdG representation is particularly useful as it allows diagonalization of the Hamiltonian in a basis of quasiparticle excitations.

The spin-orbit interaction tends to orient the spins in (x, y) plane with an in-plane direction $\mathbf{n}_{xy}$, while the magnetic field remains perpendicular to the plane. Both Dresselhaus and Rashba SOI tend to split the energy bands for states with opposite spins $|\mathbf{n}_{xy}+\rangle$ and $|\mathbf{n}_{xy}-\rangle$. For vanishing B_z and Δ, $|\mathbf{n}_{xy}\pm\rangle$ are good eigenstates of the Hamiltonian

$$\mathcal{H}|\mathbf{n}_{xy}\pm\rangle = \xi_p \pm \sqrt{\alpha^2+\beta^2}p|\mathbf{n}_{xy}\pm\rangle, \tag{4.3}$$

where $\xi_p = \frac{p^2}{2m} - \mu$.

The magnetic field has the effect to open a gap at zero momentum. When the Fermi energy is in this gap the system becomes effectively "spinless". Finally, when superconducting proximity effect is considered, and close to Fermi energy, the system can be mapped to the Kitaev model. The s-wave pairing Δ has the effect of opening gaps at Fermi momentum and to mediate p-wave pairing for the spinless model.

The presence of the Dresselhaus term only trivially modifies the spectrum for the translation invariant system [25]. The energy obtained by squaring twice the BdG Hamiltonian reads

$$E^2 = \xi_p^2 + (\alpha^2+\beta^2)p^2 + B_z^2 + \Delta^2 \pm 2[\xi_p^2(\alpha^2+\beta^2)p^2 + \xi_p^2 B_z^2 + \Delta^2 B_z^2]^{1/2}. \tag{4.4}$$

A numerical analysis requires implementing the BdG Hamiltonian in Eq. (4.2) on a lattice. Throughout the section, the lattice constant a and $\hbar$ are set to 1. The quantities can be expressed in energy units of $t = \frac{1}{m}$. The usual substitutions

$$\int dx \to L\sum_j, \quad \psi(x) \to \frac{1}{\sqrt{L}}c_j, \quad \partial_x\psi(x) \to \frac{c_{j+1}-c_{j-1}}{2\sqrt{L}}, \tag{4.5}$$

where L is the size of the system, allow to write the direct space lattice BdG Hamiltonian:

$$H = \sum_j C_j^\dagger[(t-\mu)\tau_3 + B_z\sigma_3 - \Delta\tau_1]C_j - \frac{1}{2}\Big[C_j^\dagger(t + i\alpha\sigma_2 + i\beta\sigma_1)\tau_3 C_{j+1} + \text{H.c.}\Big],$$
$$C_j = (c_{j\uparrow}^\dagger, c_{j\downarrow}^\dagger, c_{j\downarrow}, -c_{j\uparrow}). \tag{4.6}$$

The lattice Hamiltonian reproduces the continuum Hamiltonian at low energy.

4.2 Topological invariant

The computation of the topological invariant can be carried out exactly in the case of the lattice Hamiltonian. The calculation will show that the topological condition is not influenced by the Dresselhaus SOC β.

Any one-particle fermionic Hamiltonian supports a representation in a Majorana basis [67]. Let us consider on-site real quasiparticle excitation operators (the Majoranas)

$$\gamma_{1,\alpha}^{(j)} = \frac{1}{\sqrt{2}}(c_{j,\alpha} + c_{j,\alpha}^\dagger),$$
$$\gamma_{2,\alpha}^{(j)} = \frac{1}{i\sqrt{2}}(c_{j,\alpha} - c_{j,\alpha}^\dagger). \tag{4.7}$$

The Majorana fermions obey the anti-commutation relation

$$\{\gamma_{A\alpha}^{(i)}, \gamma_{B\beta}^{(j)}\} = \delta_{ij}\delta_{\alpha\beta}\delta_{AB}, \tag{4.8}$$

where, (i,j), (α,β), and (A,B) are site, spin, and respectively Majorana indices. Then in the Majorana basis $\Gamma_j^T = \left(\gamma_{1\uparrow}^{(j)}, \gamma_{2\uparrow}^{(j)}, \gamma_{1\downarrow}^{(j)}, \gamma_{2\downarrow}^{(j)}\right)$ the lattice version of Hamiltonian (4.1) is written

$$H = \sum_j (t-\mu) + \frac{i}{2}\sum_{i,j}\Gamma_i^T A_{ij}\Gamma_j \tag{4.9}$$

where A_{ij} is an anti-symmetric real matrix. The constant term does not affect the Hamiltonian topology and can be neglected. The matrix A_{ij} encodes only on-site and nearest-neighbor hopping terms. Therefore one can express the Hamiltonian in a small number of 4×4 block matrices, $A(i-j)$, which contain only spin and Majorana indices. Note that due to anti-symmetry

$$A(i-j) = -A(j-i)^T. \tag{4.10}$$

Then, without the constant term, the Hamiltonian reads

$$\begin{aligned} H &= \frac{i}{2}\sum_j [\Gamma_j^T A(0)\Gamma_j + 2\Gamma_{j+1}^T A(1)\Gamma_j], \\ A(0) &= is_2((t-\mu) + B_z\sigma_3) + i\Delta s_1\sigma_2, \\ A(1) &= -\frac{1}{2}[s_2(it + \alpha\sigma_2) - i\beta\sigma_1]. \end{aligned} \tag{4.11}$$

The Pauli matrices s are pseudo-spin matrices representing the Majorana $(1, 2)$ degree of freedom. Note that the matrices $A(0)$ and $A(1)$ are real.

If H has a gap, then one can determine if zero-energy Majorana fermions live at the edge of the 1D system by computing a topological index. A. Kitaev has proved [67] that they can exist only when the Majorana number $\mathcal{M}$ is negative

$$\mathcal{M}(H) = \text{sgn}(\text{Pf}[\tilde{A}(0)])(\text{Pf}[\tilde{A}(\pi)]). \tag{4.12}$$

Here $\tilde{A}$ is the Fourier transform of A_{ij} computed at two exceptional points 0 and π in the BZ. In the present case, with only on-site and NN terms

$$A(0/\pi) = A(0) \pm [A(1) - A^T(1)]. \tag{4.13}$$

Note that both spin-orbit coupling terms are symmetric in Majorana and spin indices, and therefore they drop out from the topological index.

Then the topological invariant reads

$$\mathcal{M}(H) = \text{sgn}(\mu^2 - B_z^2 + |\Delta|^2)\text{sgn}((2t-\mu)^2 - B_z^2 + |\Delta|^2). \tag{4.14}$$

The conditions for the existence of the topological phase supporting Majorana fermions are unaffected by the Dresselhaus SO interactions. As expected from the experimental considerations, the bandwidth t is much larger than the other parameters of the system, (Δ, B_z, α). Hence the second term is always positive, and thus a topological phase continues to exist for

$$B_z^2 > \Delta^2 + \mu^2. \tag{4.15}$$

It is interesting to note however that Majorana bound states can exist even in the absence of the Rashba term, when only Dresselhaus SO interactions are present. Dresselhaus term has a similar effect as the Rashba term in removing the spin degeneracy of the energy bands.

4.3 Majorana wave function solutions

To directly see the effect of the Dresselhaus SOC it is opportune to study the wave functions for the Majorana fermions. It has been shown that Majorana bound states can

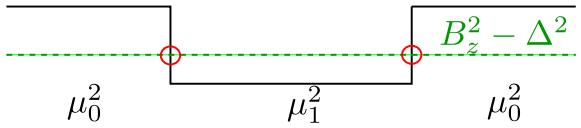

Fig. 4.1: Majorana fermions, represented in red, form at the interface with the topologically trivial states when the chemical potential creates a domain wall.

arise at the interface between trivial and topological regions of a one-dimensional wire by considering for example a position-dependent chemical potential [25]. Similarly, a model wire is divided here in three regions with variable chemical potential. The chemical potential can be changed through gating such that it takes the value μ_1 in the central region $[0, L]$ and μ_0 outside

$$\begin{aligned} &\mu_1^2 < B_z^2 - \Delta^2, \quad x \in [0, L], \\ &\mu_0^2 > B_z^2 - \Delta^2, \quad x \notin [0, L]. \end{aligned} \tag{4.16}$$

Hence a topological region is formed in the central region and Majorana fermions are expected at the boundary with the outer, trivially gapped regions.

The infinite system exhibits gaps at $p = 0$ and a superconducting gap at the Fermi momentum $p_F \neq 0$. The gap at zero momentum is $\Delta - \sqrt{B_z^2 - \mu^2}$, while the gap at p_F is the induced superconducting gap Δ. To solve the system analytically, one assumes that chemical potentials $\mu_{1,2}$ are chosen such that the gap at $p = 0$ is much smaller than the superconducting gap. Equivalently, if the induced gap Δ is close in magnitude to the Zeeman energy, it is necessary only a small change in the chemical potential to switch a region from a trivially gapped phase to a topologically nontrivial phase. Hence the low energy solutions can be obtained by linearizing the BdG Hamiltonian (4.2) in p.

$$\mathcal{H} = (\alpha p\sigma_2 + \beta p\sigma_1)\tau_3 + B_z\sigma_3 - \Delta\tau_1 - \sum_{j\in\{0,1\}} \mu_j[\theta\big(x(2j-1)\big) + \theta\big((x-L)(2j-1)\big)]\tau_3, \tag{4.17}$$

where θ is the Heaviside step function.

The Majorana wave function is determined by searching for zero energy solutions bound to the ends of the topological region. If the length of the topological region is very large, $L \gg 1$, the localized Majorana states are found independently at the two ends. They have the form of four component spinors, and the amplitude of the wave function must decay away from the interface. For example, the Ansatz for the localized function at $x = 0$ is $\psi_{0,1} \propto e^{\pm k_{0,1}x}$, with wave vectors $k_{0,1} > 0$ and $0, 1$, denoting the left (topologically trivial), respectively, the right (topologically nontrivial) side of the interface.

The allowed wave vectors for the complete system are obtained by solving for the

zero energy eigenvalues at each interface

$$k_j^{\pm} = \frac{\Delta \pm \sqrt{B_z^2 - \mu_j^2}}{\sqrt{\alpha^2 + \beta^2}}, \quad j \in \{0, 1\}. \tag{4.18}$$

The complete solutions are formed by matching the wave functions across each interface. Near the interfaces, $x = 0, L$ the wave functions are given by

$$\psi(x \sim 0) = \begin{cases} \kappa \mathbf{u}_1(\mu_1) e^{k_1^- x}, & x > 0, \\ \frac{\kappa}{2}\left[(1 + \frac{\tan\phi_1}{\tan\phi_0})\mathbf{u}_1(\mu_0)e^{k_0^- x} + (1 - \frac{\tan\phi_1}{\tan\phi_0})\mathbf{u}_2(\mu_0)e^{k_0^+ x}\right], & x < 0, \end{cases} \tag{4.19}$$

and

$$\psi(x \sim L) = \begin{cases} \kappa \mathbf{u}_3(\mu_1) e^{-k_1^-(x-L)}, & x < L, \\ \frac{\kappa}{2}\left[(1 + \frac{\tan\phi_1}{\tan\phi_0})\mathbf{u}_3(\mu_0)e^{-k_0^-(x-L)} + (1 - \frac{\tan\phi_1}{\tan\phi_0})\mathbf{u}_4(\mu_0)e^{-k_0^+(x-L)}\right], & x > L. \end{cases} \tag{4.20}$$

The spin-orbit vector is

$$e^{i\vartheta} = \frac{(\alpha + i\beta)}{\sqrt{\alpha^2 + \beta^2}} \tag{4.21}$$

and the angles ϕ_j are defined as

$$e^{i\phi_j} = \frac{1}{\sqrt{2}}\Big(\sqrt{1 + \mu_j/B_z} + i\sqrt{1 - \mu_j/B_z}\Big). \tag{4.22}$$

The Majorana eigenvectors are given by

$$\begin{aligned} \mathbf{u}_1(\mu_j)^T &= (\cos\phi_j e^{i\vartheta}, -\sin\phi_j, \sin\phi_j e^{i\vartheta}, \cos\phi_j), \\ \mathbf{u}_2(\mu_j)^T &= (\cos\phi_j e^{i\vartheta}, \sin\phi_j, -\sin\phi_j e^{i\vartheta}, \cos\phi_j), \\ \mathbf{u}_3(\mu_j)^T &= -(\cos\phi_j e^{i\vartheta}, \sin\phi_j, \sin\phi_j e^{i\vartheta}, -\cos\phi_j), \\ \mathbf{u}_4(\mu_j)^T &= (-\cos\phi_j e^{i\vartheta}, \sin\phi_j, \sin\phi_j e^{i\vartheta}, \cos\phi_j). \end{aligned} \tag{4.23}$$

Note that the obtained wave functions are indeed Majorana fermions respecting the reality condition through the phase choice $(\vartheta + \pi)/2$ for the complex coefficient κ. The magnitude of κ is determined from the normalization conditions of the wave functions and is of the order of $(\sqrt{B_z^2 - \mu_1^2} - \Delta/\sqrt{\alpha^2 + \beta^2})^{1/2}$.

The wave functions allow one to compute the spin polarization of the Majorana wave function and read directly the influence of the Dresselhaus SOC. The spin polarization

is recorded here only for the electronic degrees of freedom in the Majorana wave function. It is computed by taking the zero energy expectation value

$$\mathbf{s}(x) = \psi^\dagger(x)\left(\boldsymbol{\sigma} \otimes \frac{\tau_3 + \tau_0}{2}\right)\psi(x). \tag{4.24}$$

For the Majorana wave functions from Eqs. (4.19) and (4.20) exactly at the interface, $x = 0, L$, it follows that

$$\begin{aligned}\mathbf{s}(0) &= \frac{|\kappa|^2}{2}\Big(-\sin(2\phi_1)\cos\vartheta, \sin(2\phi_1)\sin\vartheta, \cos(2\phi_1)\Big),\\ \mathbf{s}(L) &= \frac{|\kappa|^2}{2}\Big(\sin(2\phi_1)\cos\vartheta, -\sin(2\phi_1)\sin\vartheta, \cos(2\phi_1)\Big).\end{aligned} \tag{4.25}$$

The above results show that the wave functions have the same spin polarization in z-direction, which is due to the action of the Zeeman field B_z. However, they have equal in magnitude, but opposite transverse spin polarizations. In fact, the direction of the spin polarization at both interfaces is given entirely by the relative weight of the Rashba and Dresselhaus SOC

$$\frac{s_2}{s_1} = -\frac{\beta}{\alpha}. \tag{4.26}$$

The Majorana polarization vectors for the Majorana wave functions are also readily available, $\mathbf{P}_M = (P_{M_x}, P_{M_y})$

$$\mathbf{P}_M(0) = -\mathbf{P}_M(L) = -|\kappa|^2(\cos\vartheta, \sin\vartheta\cos(2\phi_1)). \tag{4.27}$$

They are also opposite for the two end Majorana fermions. This arguably allows us to call the two modes as "different" Majoranas. When the two modes are brought together, they form a regular fermion with zero Majorana polarization.

For fixed parameters μ, Δ and B_z, P_{M_x} is proportional to s_1, while P_{M_y} is proportional to s_2. Thus, when only Rashba/Dresselhaus SOC is present, the total transverse spin polarization is proportional to the Majorana polarization, with a proportionality constant which depends on the chemical potential potential and the applied Zeeman field. When both components of the SOC are present, the Majorana polarization and the transverse spin polarization vectors are no longer collinear.

Eq. (4.26) indicates that the local spin density for the Majorana electronic degrees of freedom should rotate in transverse direction under the influence of the Dresselhaus term. It is important to stress that there is no transverse polarization of the system. This statement remains true if one considers the entire Majorana function or if one puts together an electron from its "fractionalized" components at the two ends.

4.4 Numerical study

The numerical study supports the analytical study undertaken in the previous section. The model BdG Hamiltonian is given in Eq. (4.6), and is implemented in a 100-site system.

As mentioned before, the spin-orbit couplings for the physical system can be expected to be of order 0.1 eV Å ($\hbar = 1$) or $\alpha \sim \beta \sim 10^4$ m/s. Hence the spin-orbit coupling energy, $m\alpha^2$, is of the order 1 K. The Zeeman energy can be of the order ~ 100 K, while the superconducting proximity effect can create gaps of order $\Delta \sim 1 - 10$ K. The hopping strength $t = \frac{\hbar^2}{ma^2}$ is of the order of the bandwidth $\sim 10^4$ K [76, 108, 115]. In the numerical simulations, the lattice constant a and the reduced Planck constant $\hbar$ are dimensionless and equal to one, $a = \hbar = 1$. All the physical quantities are measured in units of the hopping strength $t = 1$. Due to finite size effects on the 100-site system, it is hard to visualize the physics of the Majorana system for small B_z and Δ with respect to the hopping strength t. Therefore, B_z, Δ, α are artificially enhanced in the following, while maintaining them smaller than t. The reference values for the rest of the simulations are $\Delta = 0.3, B_z = 0.4, \alpha = 0.2$ and $\mu = 0$, and any deviation from these values is explicitly noted.

Exact diagonalization of BdG Hamiltonian in Eq. (4.6) provides the local density of states, and the local spin-polarized density of states along the x, y, and z directions. For example the local (site n) electronic i-spin polarization density at a given energy E is defined here as

$$\boldsymbol{s}_n(E) = \sum_{j=1}^{4N} \Psi_n^{\dagger(j)} \left(\boldsymbol{\sigma} \otimes \frac{\tau_0 + \tau_z}{2} \right) \Psi_n^{(j)} \delta(E - E_j), \tag{4.28}$$

where N is the number of sites in the system, E_j is the j^{th} eigenvalue of H and $\Psi_n^{(j)}$ is the site n component of the j^{th} eigenvector, $\Psi_n^{\dagger\,(j)} = (u_{n\uparrow}^{(j)}, u_{n\downarrow}^{(j)}, v_{n\downarrow}^{(j)}, v_{n\uparrow}^{(j)})$. Similarly, it is possible to compute the local Majorana polarizations as a lattice version of Eqs. (3.52)

$$P_{M_x,n} = \sum_{j=1}^{4N} 2\mathrm{Re}[u_{n\downarrow}^{(j)} v_{n\downarrow}^{*(j)} - u_{n\uparrow}^{(j)} v_{n\uparrow}^{*(j)}] \delta(E - E_j). \tag{4.29}$$

The Dirac delta functions are implemented as Gaussians of width $\sim 10^{-4} \hbar v_F / a$.

The x and z components of the spin polarization, as well as the Majorana polarization, in a system without Dresselhaus SOC, are represented in Fig. 4.2. The analytical solution correctly predicts that there is no y-spin polarization, while the zero bound states have opposite electronic x-spin polarization at the two ends. Due to the Zeeman magnetic field, both end modes are identically z-spin polarized. The zero-energy Majorana wavefunctions are extended over a small number of edge sites, and exhibit strongly damped spatial oscillations.

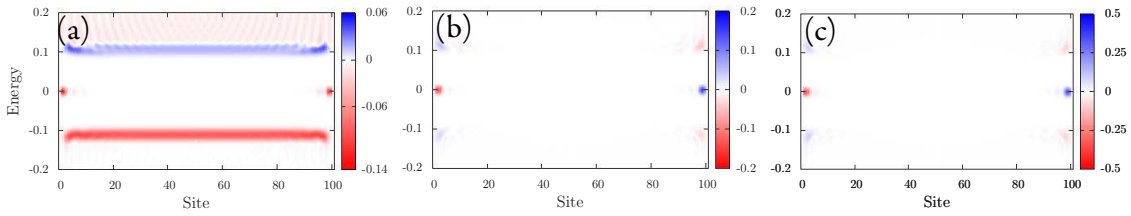

Fig. 4.2: The spin polarization along (a) the z and (b) x directions, and (c) the Majorana polarization P_{M_x}, as a function of energy and position, $\Delta = 0.3$, $B_z = 0.4$, $\alpha = 0.2$, $\beta = 0$ and $\mu = 0$.

Note that the analytical result in Eq. (4.25) predicts that the z-polarization vanishes for $\mu_1 = 0$,

$$\cos(2\phi_1) = 0. \tag{4.30}$$

This is not the case seen in the numerical simulations, where there is a appreciable z-spin polarization of Majorana modes (see Fig. 4.2(a)). However the analytic result was obtained by neglecting the kinetic term in the Hamiltonian from Eq. 4.1. To leading order, the quadratic term contributes with an effective μ

$$\langle p^2 \rangle \approx O((\Delta - B_z)^2), \tag{4.31}$$

which creates a *negative* effective potential in qualitative accord with the numerical results. Moreover, this effective chemical potential is responsible for the spatial (quickly damped) oscillations of the spin polarization observed numerically. Although these oscillations are not captured by the continuum limit calculations, for any site i the ratio $s_{2,i}/s_{1,i}$ depends only on the spin-orbit couplings in agreement with Eq. (4.25).

Fig. 4.3 exemplifies the case where only Dresselhaus SOC is present. The local density of states reveals that zero modes bound at the ends of the wire continue to be present (see Fig. 4.3(a)). Majorana and spin polarization support the analytical findings. The modes are entirely polarized on the y-direction, i.e. orthogonal to the case $\alpha \neq 0$ and $\beta = 0$. For example, a plot of the Majorana polarization P_{M_y} identifies the zero modes as Majorana states in Fig. 4.3(b).

The numerical results for the Majorana polarization presented in Fig. 4.2 also follow closely Eq. (4.27). The values of the Majorana polarization are always opposite at the two ends of the wire. When the Dresselhaus term is non-vanishing, the modes gain a P_{M_y} component. Without Dresselhaus SOC, P_{M_x} is proportional in this case to the x-spin polarization. However, in general there is a crucial difference from the spin-polarization. The Majorana polarization vector rotates in the transverse direction from site to site. When both the Rashba and Dresselhaus SOC components are present, the Majorana polarization in Eq. (4.27) depends on the $\cos(2\phi_1)$ and, subsequently, the ratio P_{M_y}/P_{M_x} can vary on the end sites over which the Majorana mode is extended, in contrast to the spin case. The precession of Majorana polarization makes it more favorable to register

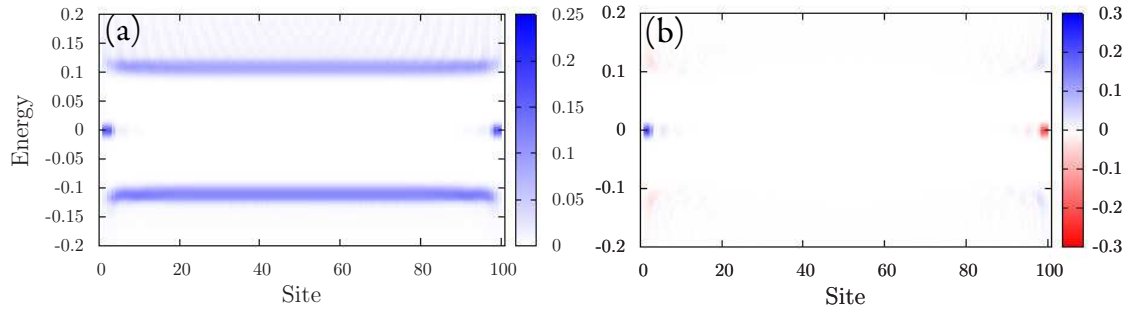

Fig. 4.3: (a) Local density of states and (b) Majorana polarization P_{M_y} at $\Delta = 0.3$, $B_z = 0.4$, $\mu = 0$, $\alpha = 0$, and $\beta = 0.2$. Majorana bound states are present at the ends of a wire containing only Dresselhaus SOC.

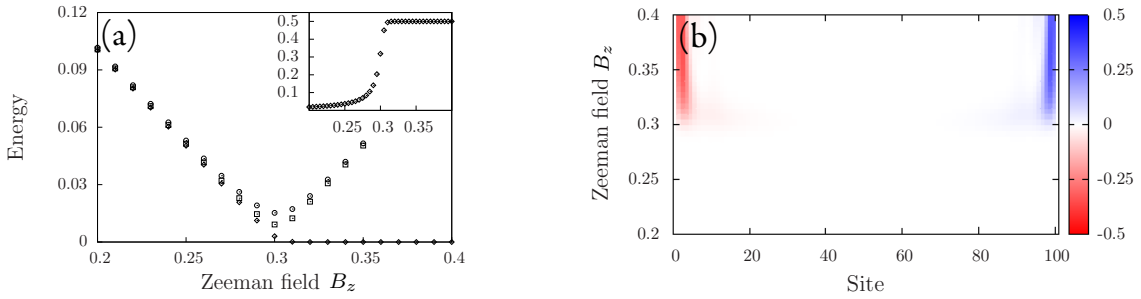

Fig. 4.4: (a) Lowest-energy eigenvalues and the half-wire integral of the Majorana polarization P_{M_x} (inset) as a function of B_z. (b) Majorana polarization P_{M_x} of the lowest-energy state as a function of position and B_z. Parameters: $\Delta = 0.3$, $\mu = 0$, $\beta = 0$, and $\alpha = 0.2$

the Majorana polarization density (3.50) and prove that it is 0.5 for a zero energy mode bound at the wire extremities.

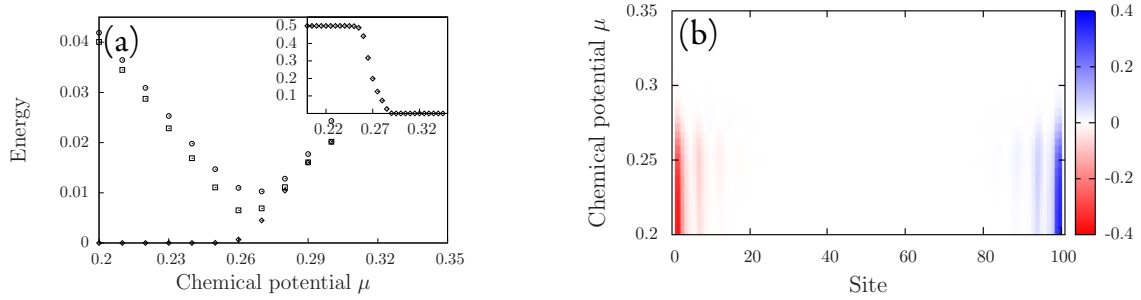

Fig. 4.5: (a) The lowest-energy eigenvalues and the half-wire Majorana polarization P_{M_x} integral (inset) are plotted as a function of μ. In the second panel the Majorana polarization P_{M_x} of the lowest-energy state is plotted as a function of position and μ. The parameters considered are $\Delta = 0.3$, $B_z = 0.4$, $\alpha = 0.2$, and $\beta = 0$.

In the following, the claim that Majorana polarization is a good order parameter to

characterize the topological transition receives more numerical support. This is done by varying each of the parameters (Δ, B_z, μ) to drive the system in a trivial phase. In Fig. 4.4(a), B_z is varied and it is shown that the system becomes trivially gapped (no Majorana bound states) for $B_z \leq \Delta$. The inset describes the dependence of the half-wire integral of the Majorana polarization for one of the lowest-energy states as a function of B_z (an integral of 0.5 is equivalent to a "full" Majorana state). The Majorana polarization decreases smoothly to zero below the critical value of B_z. The same phenomenon can be observed in Fig. 4.4(b), where the spatial distribution of the Majorana polarization is plotted as a function of B_z. The transition becomes sharper for an increasing system size. The same qualitative features are obtained when Δ and μ are varied across the topological transition. For example, the variation of the chemical potential is represented in Fig. 4.5.

Discussion

The present chapter has shown that the Majorana polarization (and density) is a good local order parameter to identify the topological transition at $B_z^2 = \Delta^2 + \mu^2$. Furthermore, it was shown that there is a spin texture in the transverse plane to the magnetic field and it depends on the relative strength of Dresselhaus and Rashba spin-orbit coupling. The electronic degrees of freedom of the Majorana wave function at the two ends of the wire are polarized in opposite directions on the transverse plane. This could be in principle detected through a contact to an impurity [112, 113]. However it is necessary to detail such claim. How is it possible to have access only to the electronic part of the wave function?

Note that the system remains spin unpolarized at zero energy, and that could be realized only if there is a compensation for the spin polarizations at the two extremities of the wire. Then the explanation for the registered spin-texture must invoke a conservation of the polarization in the transverse direction. However, it remains in perspective to understand in more detail the physical reasons for this particular spin-texture.

Chapter 5

Extended Majorana states in Josephson junctions

The one-dimensional topological superconductor supporting Majorana fermions was shown in the previous chapters to admit a pertinent implementation in a heterostructure constructed from a spin-orbit coupled semiconducting wire in proximity to an s-wave superconductor. Detection schemes of Majorana fermions often require building on this basic structure. In particular, for transport measurements, the heterostructure can be connected to a normal metal region, thus forming a "superconductor"-normal metal (SN) junction. They were recently investigated experimentally in Ref. [91] and a zero-bias conductance peak thought to be associated with Majorana fermions [103, 104, 116–118] was detected through tunneling spectroscopy. A different system can be constructed by coupling two topological superconductors through a normal metal such that Majorana fermions form in the normal region. The presence of Majorana fermions in these "superconductor"-normal metal-"superconductor" (SNS) junctions gives rise to a fractional Josephson current with a 4π periodicity [67, 102, 119–121].

In the present chapter, several models for one-dimensional SN and SNS junctions are investigated numerically. The interest lies in following the behavior of the Majorana states in these new geometries. The essential property acquired by the Majorana fermions due to the coupling to a normal metal is that they can become extended states (see Sec. 5.1 and Refs. [76, 118, 122, 123]) In the case of the SNS junction, this has the particular effect that the normal region supports two extended Majoranas (see Sec. 5.3). This happens only at a phase difference π between the two superconductors; otherwise the Majorana states hybridize and form Andreev bound states at higher energies. The two extended Majorana fermions are recognized by reading a total integrated Majorana polarization of one over the normal region. Finally, in Sec. 5.4.2, the formation of Majorana fermions is studied in linear and ring geometries under a uniform superconducting phase gradient.[**?**] The ring geometry is of particular interest as the twisting of the phase allows the formation zero energy bound states in a normal region, similar to the regular

Fig. 5.1: Schematic representations of (a) superconductor-normal and (b) superconductor-normal-superconductor junctions. They are created by having the spin-orbit coupled semiconducting wire added on top of an s-wave superconductor (S). A perpendicular magnetic field B_z acts on the wire.

SNS junction.

5.1 Superconductor-normal junctions

Let us consider first the SN junction that is schematically represented in Fig. 5.1(a). The system consists of a spin-orbit coupled semiconducting wire in proximity to an s-wave superconductor. However, the wire sits only partially on the superconductor. Therefore it is assumed that the superconducting proximity effect does not affect the entire wire. This is modeled by having a constant induced gap Δ only on N sites. A variation considered subsequently is that of a decaying induced gap, which can be associated to a penetration length of Cooper pairs in the normal region.

The Hamiltonian of the system is an amendment to the model in Eq. (4.6) with chemical potential μ, induced gap Δ, magnetic field B_z and only the Rashba spin-orbit coupling α

$$H = \sum_{j=1}^{L} C_j^\dagger[(t-\mu)\tau_3 + B_z\sigma_3 - \Delta\tau_1\theta(N-j)]C_j - \frac{1}{2}\left[C_j^\dagger(t+i\alpha\sigma_2)\tau_3 C_{j+1} + \text{H.c.}\right],$$
$$C_j = (c_{j\uparrow}^\dagger, c_{j\downarrow}^\dagger, c_{j\downarrow}, -c_{j\uparrow}), \tag{5.1}$$

where L is the total number of sites in the system and N, the sites with induced gap. In numerical simulations, the system size L is 100 sites and N is 80 sites. Hence the normal region extends over the last 20 sites. Unless explicitly specified, the model parameters are chosen the same as in Sec. 4.4, $B_z = 0.4$, $\Delta = 0.3$, $\alpha = 0.2$ and $\mu = 0$, thus placing the system under the topological condition (3.41). The lattice constant a and the reduced Planck constant $\hbar$ are set to one; all parameters are expressed in units where the hopping strength is one, $t = 1$. In contrast to Sec. 4.4, the delta-function entering the definition of LDOS and Majorana polarization are implemented as Gaussians of width $\sim 10^{-5}\hbar v_F/a$.

The condition to have a Majorana fermions remains the same as the one in Eq. (3.41)

$$B_z^2 > \Delta^2 + \mu^2. \tag{5.2}$$

The crucial difference is that the right Majorana fermion from the topological superconductor extend uniformly over all sites of the normal region. The integrated Ma-

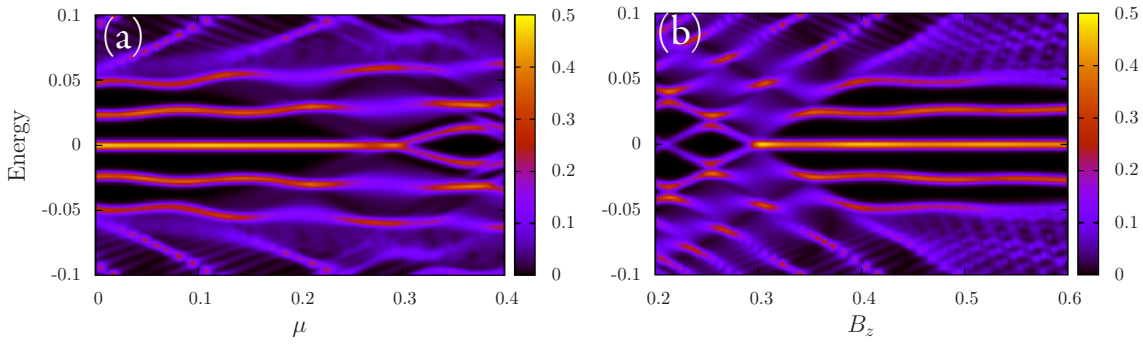

Fig. 5.2: Resperesentation of the Majorana density as a function of (a) the chemical potential μ and (b) the magnetic field B_z. The topological transition where the Majorana fermion states disappear at $\mu_c \simeq 0.26$ and $B_z = 0.3$.

jorana density (3.50) (for lattice version (4.29)) over the normal region is represented in Fig. 5.2. The fact that it yields the $1/2$ indicates that there is exactly one Majorana fermion extended over the normal region. Furthermore, the topological condition is verified by varying the parameters of the system. Fig. 5.2(a) exemplifies the variation of the chemical potential μ, while Fig. 5.2(b), the variation of the magnetic field B_z. In both cases the topological transition takes place at the values predicted from Eq. (3.41); when the other parameters are fixed, the critical chemical potential is $\mu_c \simeq 0.26$ and the critical Zeeman field is $(B_z)_c = 0.3$.

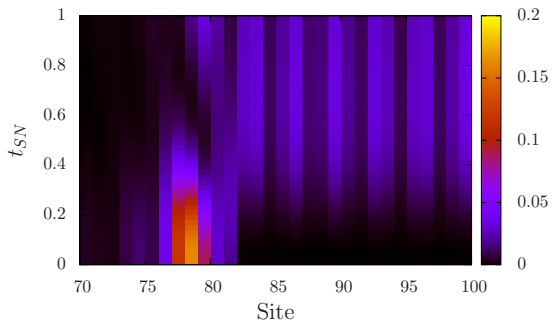

Fig. 5.3: Representation of the zero-energy LDOS dependence on the hopping strength t_{SN} between the superconducting and normal region. A localized Majorana fermion extends in the normal region when increasing coupling to the bulk value $t = 1$.

The extended nature of the Majorana fermions can be visualized by varying smoothly the coupling t_{SN} between the normal and superconducting region. When the coupling is very weak, the superconducting region is effectively connected on the right side to a trivial insulator. Hence Majorana fermions remain localized at the end of the superconducting region. However, increasing the coupling t_{SN} leads to extended zero energy modes. This situation is illustrated in Fig. 5.3 by recording the zero-energy local density of states in the normal region as a function of t_{SN}.

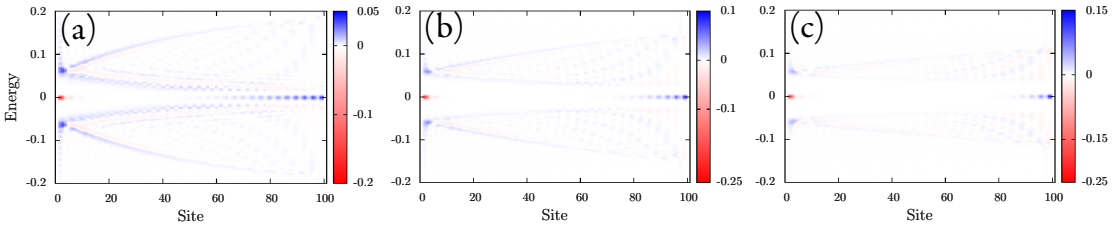

Fig. 5.4: Low-energy Majorana x-polarization illustrates the increasing localization of right Majorana fermions with the growth of the superconducting region by ramping up the penetration length ξ_p. (a) $\xi_p = 50$, (b) $\xi_p = 100$, (c) $\xi_p = 200$.

Let us finally consider a smooth decay of the superconducting gap into the normal region. For a small penetration length ξ_p of Cooper pairs into the normal region, the system supports, as before, extended Majorana fermions. When the penetration length becomes large, the topological superconducting region is prolonged into the normal region. Therefore the Majorana fermions become more and more localized with the diminishing normal region. In Fig. 5.4 is presented a limit case of the above situation. The wire is connected to a p-wave superconductor only at its left edge and Cooper pairs enter into the wire by proximity effect. In the same basis as before, the Hamiltonian that models the wire reads

$$H = \sum_{j=1}^{L} C_j^\dagger [(t-\mu)\tau_3 + B_z\sigma_3 - \Delta e^{-j/\xi_p}]C_j - \frac{1}{2}\left[C_j^\dagger (t + i\alpha\sigma_2)\tau_3 C_{j+1} + \text{H.c.}\right]. \quad (5.3)$$

Fig. 5.4 illustrates cases with an increasing penetration length. Note that the penetration length can be seen as an estimate of the size of the topological superconducting region in the wire. As the penetration length grows, the normal region diminishes and the Majorana fermions become more and more localized on the right side. Note again that Majorana fermions at the two ends of the wire have opposite Majorana x-polarization, but the extension of the right Majorana does not weigh on the fact that the integral Majorana polarization in the normal region yields $1/2$. Hence the "normal region" hosts a single Majorana fermion of variable extension.

The following sections are mostly centered on the exploration of Majorana fermions in SNS junctions. The presence of Majoranas in the normal region is crucially displayed in the fractional Josephson effect. The essential features of this particular phenomena are presented next.

5.2 Fractional Josephson effect

A Josephson junction is created by bringing into proximity two superconductors (see Fig. 5.5). Between them can either be a weak metallic link, or an insulating barrier. However, Cooper pairs can tunnel between the two superconductors. This gives rise

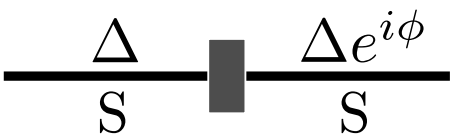

Fig. 5.5: Schematic picture of a Josephson junction. Without loss of generality, one can consider that the superconducting parameter has equal absolute value in the two superconductors. The left superconductor is conventionally considered real, while there is a superconducting phase ϕ in the right wire. In the middle there is an insulating barrier or a metallic region.

to the Josephson current, that depends on the phase difference between the superconductors. Here the focus is on the DC Josephson effect [124], in which there is no voltage difference across the junction and the phase between superconductors is considered fixed. This results in a direct current dependent on the phase difference ϕ

$$I_J \propto \sin(\phi). \tag{5.4}$$

The remarkable feature of the one dimensional systems supporting Majorana fermions is the presence of a *fractional* DC Josephson effect. The tunneling between the superconducting islands takes place by fusing Majorana fermions that are close on the left and right side of the junction [67, 102]. This leads to tunneling events involving single electrons instead of Cooper pairs. The resulting current-phase relation has the distinctive 4π-periodicity

$$I_J \propto \sin(\phi/2). \tag{5.5}$$

To understand this relation, consider a junction created using the Kitaev model [76, 121]. The junction is modeled by the Hamiltonian

$$H = H_L + H_R + H_T, \tag{5.6}$$

where H_L represents the Kitaev model (3.24) describing the left wire, with real superconducting order parameter, and, respectively, H_R, the Kitaev model for the right wire, with a generally complex superconducting parameter, having a phase ϕ, $\Delta \to \Delta e^{i\phi}$ (see Fig. 5.5). A short junction will have the tunneling Hamiltonian H_T given by

$$H_T = -\Gamma c_R^\dagger c_L + \text{H.c.}, \tag{5.7}$$

where Γ is the coupling between the superconducting islands. The operators $c_{R/L}^\dagger$ correspond to the fermion creation operators on the right and, respectively, on the left side of the junction.

Let us suppose that left and right wires are in a topological phase, $|\mu| < 2|t|$. Then for wires placed far away from each other, there are zero energy Majorana fermions pinned at the extremities of the two wires. When a junction is formed by bringing together the

two wires, the two end Majorana fermions can couple. Furthermore, at low energy, the physics is *entirely* determined by the two end Majoranas. This is because the wires are assumed long enough that the influence from opposite end Majorana fermions remains negligible. Moreover, all the other states are energetically separated from the Majorana fermions by the bulk superconducting gap.

To understand the physics of the Josephson junction it is sufficient to treat a limit case, when the Majorana fermions are completely localized at one extremity site (see Sec. 3.2.2) for $\mu = 0$ and $\Delta = t$. Then at low energy one uses Eqs. (3.26) to obtain

$$\begin{aligned} c_L &\to \frac{i}{\sqrt{2}}\gamma_2, \\ c_R &\to \frac{1}{\sqrt{2}}\gamma_1 e^{-i\phi/2}. \end{aligned} \tag{5.8}$$

Note that in the above low-energy substitution, the missing Majorana fermions from the decomposition of a complex fermion hybridize with the Majorana fermions from adjacent sites to create bulk states. Therefore the low-energy Hamiltonian of the junction reads

$$\begin{aligned} H_{\text{eff}} &= -i\Gamma \cos(\phi/2)\gamma_1\gamma_2, \\ &= -\frac{\Gamma}{2}\cos(\phi/2)(2c^\dagger c - 1). \end{aligned} \tag{5.9}$$

The second equality is obtained by using Eq. (3.23); the effective Hamiltonian was written as a function of the occupation number $c^\dagger c$ of the electronic state due to the fusion of the Majorana fermions γ_1 and γ_2.

As explained in Ref. [76], one notes that the occupation number is trivially a conserved quantity because it commutes with H_{eff}. Therefore an occupied state has energy $E = -\Gamma/2$ at $\phi = 0$ and goes to $E = \Gamma/2$ at $\phi = 2\pi$. The phase ϕ needs to increase by another 2π for a state to come back at the original energy. This is the 4π-periodicity of the energy spectrum characteristic to the fractional Josephson effect. As announced, the 4π-periodicity reflects itself also in the Josephson current

$$I_J \propto \frac{\partial\langle H_{\text{eff}}\rangle}{\partial\phi} = \frac{\Gamma}{2}\sin\left(\frac{\phi}{2}\right). \tag{5.10}$$

Note that at $\phi = \pi/2$ there are two degenerate zero energy states: the Majorana fermions. At this angle there is a pair of Majorana fermions trapped at the junction. Away from $\phi = \pi/2$, the energy states are lifted from zero and become Andreev bound states inside the superconducting gap. The rest of the chapter is devoted to various incarnations of the fractional Josephson effect in long junctions.

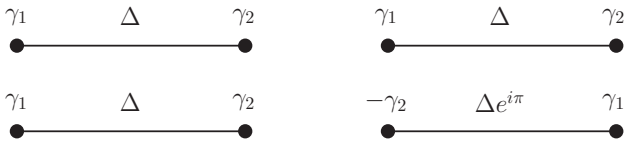

Fig. 5.6: A different view of fractional Josephson effect. An SNS junction is created by connecting two topological superconducting regions with Majorana fermions at extremities. The right region can have a complex phase. When the wires are connected through a metallic section, two central Majorana fermions extend inside and hybridize. However two central Majorana fermions are identical at $\phi = \pi$ and do not hybridize.

5.3 Superconductor-normal-superconductor junction

The SNS junction considered here is schematically presented in Fig. 5.1(b). The wire is placed on two s-wave superconducting islands. Due to the proximity effect, these two outer regions of the wire are mapped to topological superconductors. Conventionally, the left region has a real superconducting order parameter, while the right region has a complex superconducting order parameter with a phase ϕ. The central region of the wire does not experience the superconducting proximity effect and forms the normal region of the junction.

The main purpose of the chapter is to illustrate the Josephson effect in this geometry. Taken separately, each superconducting region supports Majorana fermions at its ends. When they are connected through the normal region, the two end Majorana fermions can become extended in the normal region. This phenomenon takes place at a phase difference $\phi = \pi$ between the superconducting islands. For different values, the two central Majorana fermions form extended Andreev states at energies lower than the bulk superconducting gap.

Here the Majorana polarization is used to illustrate the fact that Majorana fermions at the junction are of the same type for $\phi = \pi$. This suggests a different way to look at the Josephson effect. A rotation of the phase π in a superconducting region manifests itself as a change $\gamma_1 \to -\gamma_2$ and $\gamma_2 \to \gamma_1$. Therefore, at $\phi = \pi$, the two Majorana fermions at the junction are of same type and do not couple (see Fig. 5.6). For any other value in $[0, 2\pi]$ there is a hybridization into Andreev bound states. An analysis of the Majorana polarization captures this result, because a rotation with ϕ produces a rotation of the polarization vector (P_{M_x}, P_{M_y}). At $\phi = 0$ the vector has only a P_{M_x} component (see Chap. 4). A change of phase by π rotates the polarization vector by π. Hence at $\phi = \pi$ there are two zero modes with the same Majorana polarization in the junction, and, subsequently, the normal region will read a Majorana density of one.

In the numerical study, a $L = 100$ site system is considered. The model parameters are chosen as in the previous section. The induced superconducting parameter Δ is modeled as a Heaviside step function. If a smooth decay is considered instead, then only the extension of Majorana fermions in the normal region is affected. The Hamiltonian

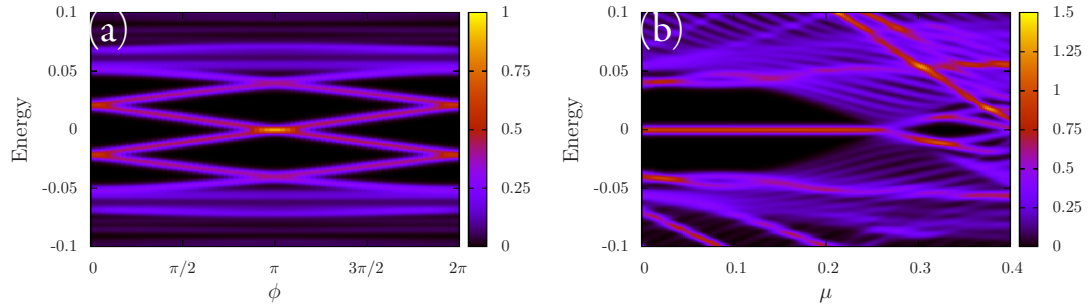

Fig. 5.7: (a) Majorana polarization density view of the fractional Josephson effect. At angle $\phi = \pi$ there are two Majorana fermions forming in the junction. (b) Density of states in the normal region at $\phi = \pi$. Robust Majorana modes are present in the junction with the variation of μ. The critical chemical potential where the Majorana modes are destroyed is predicted by the topological condition (3.41, $\mu_c \simeq 0.26$.

that models the system in Fig. 5.1(b) reads

$$H = \sum_{j=1}^{L} C_j^\dagger[(t-\mu)\tau_3 + B_z\sigma_3]C_j - \frac{1}{2}\left[C_j^\dagger(t + i\alpha\sigma_2)\tau_3 C_{j+1} + \text{H.c.}\right] - \sum_{j=1}^{N_1} C_j^\dagger \Delta C_j - \sum_{j=N_2}^{L} C_j^\dagger \Delta e^{i\phi} C_j, \tag{5.11}$$

where the normal region extends between N_1 and N_2. During the simulations the normal region has 20 sites, $N_1 = 40$ and $N_2 = 60$.

The physics of the fractional Josephson effect is verified by having a wire that respects the topological condition, $B_z^2 > \Delta^2 + \mu^2$. In Fig. 5.7(a) is represented the Majorana polarization density integrated over the normal region as a function of the superconducting phase. This illustrates two essential properties: there are two Majorana fermions in the junction (the density reaches the value one) and they exist only when the phase is equal to π. Additionally, the Majorana fermions that form at the junction are robust when changing the parameters of the model. This means that the topological condition for the existence of Majorana fermions remains valid. For example, in Fig. 5.7(b), the chemical potential μ is varied. Consequently, the Majorana fermions in the junction survive until reaching the critical chemical potential determined from the topological condition (3.41), $\mu_c \simeq 0.26$.

Finally, the Majorana polarization picture of the fractional Josephson effect is detailed in Fig. 5.8. For a zero phase difference between the superconducting islands, there are no Majorana fermions forming in the junction. Majorana fermions remain at the extremities of the wire because the system sits in a topological phase (3.41). The would-be Majorana states in the normal region hybridize and appear as Andreev bound states at

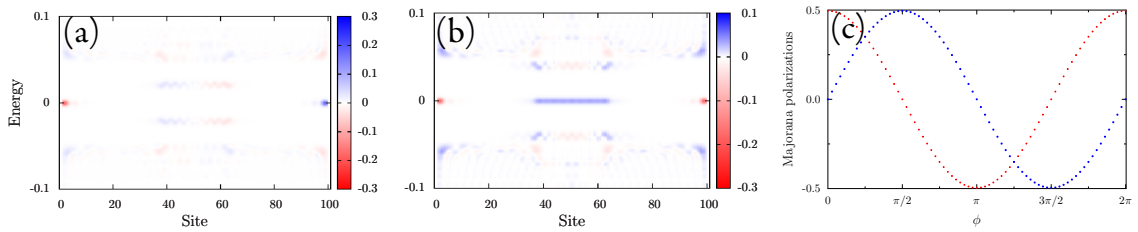

Fig. 5.8: Majorana x-polarization, P_{M_x}, at (a) $\phi = 0$ and at (b) $\phi = \pi$. The Majorana polarization rotates with the phase. At $\phi = \pi$ there are two extended Majorana fermion forming in the normal region. (c) Majorana polarization P_{M_x} (red) and P_{M_x} (blue) for the Majorana fermion trapped at the right extremity.

energies lower than the superconducting bulk gap (see Fig. 5.7(a)). When the phase varies from $\phi = 0$, the Majorana fermion at the right end of the wire responds by rotating its polarization vector. The Andreev states get gradually closer to zero energy as the phase approaches $\phi = \pi$ and additionally change their polarization. At $\phi = \pi$ the Andreev states fuse to create extended Majorana fermions with the same polarization (see Fig. 5.7(b)). Hence an integrated Majorana density of 1 (i.e. 2 Majorana fermions) is recorded in the normal region. In Fig. 5.7(c) is represented the rotation of the polarization vector for the right end Majorana fermion. It was checked in Ref. [122] that the Andreev bound states, when approaching zero energy, gradually gain a Majorana polarization to compensate the change in polarization of the right end zero-bound energy state.

5.4 Ring with a uniform phase gradient

This section develops the previous numerical study of the SNS junction to ring geometries as the one schematically illustrated in Fig. 5.9(a). The spin-coupled semiconducting wire is fashioned into a ring and placed flat on an s-wave superconductor. One section of the wire does not touch the superconductor and, considering that it does not experience the superconducting proximity effect, forms the "normal" region of the ring. The rest of the ring realizes a topological superconductor. Even if the the wire parameters are chosen such that it falls under the topological condition (3.41), there will be no Majorana fermions at the interface between the normal and superconducting region. This is because the would-be Majorana fermions forming at the two ends of the superconducting region communicate through the normal region and are lifted from zero energy. Nevertheless Majorana fermions could still form if the phase of the superconductor is allowed to vary along the wire.

In Ref. [125], it was shown that supercurrents in the bulk of the superconductor could be used in principle to manipulate the Majorana fermions. More precisely, it has been shown that a constant spatial gradient in the phase of the superconducting parameter can drive the system from a topological phase supporting Majorana fermions to a

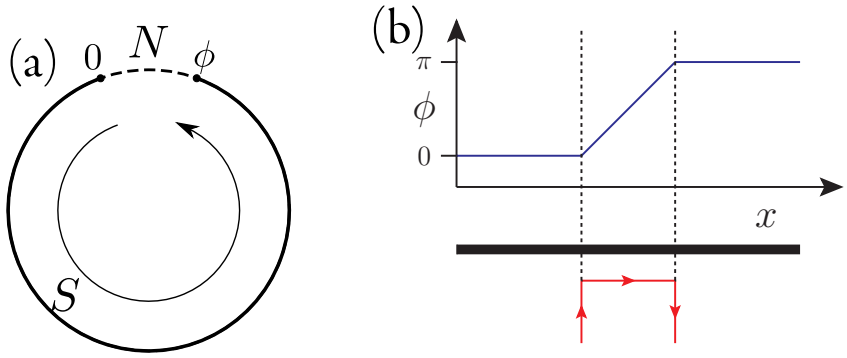

Fig. 5.9: (a) Ring geometry where a uniform phase gradient varies the phase of the induced superconducting parameter from 0 to ϕ in the superconducting region S. The normal region (N) in the wire is represented by a dashed line. (b) Variation of the superconducting phase in a topological SC wire: the phase ϕ is set to zero in the left region, and a constant gradient is considered to be induced in the central region by bulk supercurrents (in red) such as that the phase ϕ reaches a value of π in the left region of the wire.

trivial phase without zero-energy bound modes. This is the necessary ingredient to form Majorana fermions in the ring geometry.

Before tackling the ring geometry, it is instructive to investigate first the linear geometry in order to understand the action of the uniform superconducting phase gradient. This study was carried out in Ref. [125] and it is illustrated here in the context of a one-dimensional tight-binding model. The linear geometry is identical to the one treated in Sec. 3.2.3 with the essential adjustment that the superconducting phase is allow to twist along the wire via a uniform phase gradient. One can also fashion a tripartite system where the gradient acts only on the central region of the wire. A typical spatial dependence of the phase is presented in Fig. 5.9(b); there are two outer regions of constant phase, with a central region uniform experiencing a phase twist. The main interest lies in finding whether the uniform phase variation may give rise to similar physics to the one observed in the SNS junction. The question is if through the action of the phase gradient alone it is possible to bring the central region in a "normal phase". In the second subsection, the ring geometry with a uniform phase gradient in Fig. 5.9(b) is investigated in order to identify the Majorana fermions in the normal region.

5.4.1 Constant phase gradient in a wire

Consider the system present in the previous sections with the same model parameters. The system is composed of three parts with a central region that experiences the uniform phase gradient $\nabla\phi$ and is modeled by the Hamiltonian

$$H = \sum_{j=1}^{L} C_j^\dagger[(t-\mu)\tau_3 + B_z\sigma_3 - \Delta e^{-i\phi_j}]C_j - \frac{1}{2}\left[C_j^\dagger(t+i\alpha\sigma_2)\tau_3 C_{j+1} + \text{H.c.}\right]. \quad (5.12)$$

Note that the phase of the superconducting parameter, ϕ_j, is site-dependent. In the central region of the wire (between sites N_1 and N_2) there is a phase gradient $\nabla\phi$ which acts by increasing the phase, $\phi_j = \phi_{j-1} + \nabla\phi$.

Before launching into a numerical analysis of the tight-binding Hamiltonian in Eq. (5.12), it is worthy to consider the effect of the constant phase gradient on the topological invariant. It is not entirely surprising that the gradient of the superconducting parameter can make the system switch between a topological trivial and nontrivial phase. For a uniform gradient, this can be readily understood in the limit of an infinite wire. As shown in Ref. [125], the phase of the pairing term can be gauged away, with the effect of adding a gradient-dependent correction to the canonical momentum and of renormalizing the hopping parameter and the spin-orbit coupling. For an infinite tight-binding wire, the condition to have a topological phase, computed using the method presented in Sec. 4.2, yields

$$\left\{\left[\mu-\frac{t}{8}(\nabla\phi)^2\right]^2-\frac{\alpha^2(\nabla\phi)^2}{4}-V_z^2+|\Delta|^2\right\}\times\left\{\left[\mu-2t-\frac{t}{8}(\nabla\phi)^2\right]^2-\frac{\alpha^2(\nabla\phi)^2}{4}-V_z^2+|\Delta|^2\right\}<0. \tag{5.13}$$

When the bandwidth t is larger than the other parameters of the system, the second term of the product is always positive. Thus, for a zero chemical potential μ, the critical phase gradient is the exact lattice analogue of the continuum expression determined in Ref. [125]:

$$(\nabla\phi)_c = 2\sqrt{2}\left\{\left(\frac{\alpha}{t}\right)^2+\left[\frac{V_z^2-\Delta^2}{t^2}+\left(\frac{\alpha}{t}\right)^4\right]^{1/2}\right\}^{1/2}. \tag{5.14}$$

A phase gradient has a Cooper pair-breaking effect and can close the superconducting gap at the Fermi momentum. This leads to a second critical value for the phase gradient $(\nabla\phi)_{gl}$ above which the bulk gap closes and the system enters a gapless regime (see Fig. 5.10). Its exact value is determined by numerically studying the closing of the gap for an infinite system that experiences a uniform phase gradient $\nabla\phi$. The study is carried here on a momentum space Bogoliubov-de Gennes Hamiltonian

$$\begin{aligned} H &= \frac{1}{2}\sum_k C_k^\dagger \mathcal{H} C_k, \quad C_k = (c_{k\uparrow}^\dagger, c_{k\downarrow}^\dagger, c_{-k\downarrow}, c_{-k\uparrow}), \\ \mathcal{H} &= (t-\mu)\tau_3 + B_z\sigma_3 - |\Delta|\tau_1 \\ &\quad - [t\cos(k)+\alpha\sin(k)\sigma_2]\cos(\nabla\phi/2)\tau_3 - [t\sin(k)-\alpha\cos(k)\sigma_2]\sin(\nabla\phi/2). \end{aligned} \tag{5.15}$$

For the system parameters ($B_z = 0.4, \Delta = 0.3, \alpha = 0.2, \mu = 0$), the gradient for which the system enters the gapless phase is $(\nabla\phi)_{gl} \simeq 0.27$, while the topological condition determines a critical phase gradient $(\nabla\phi)_c \simeq 1.57$.

Let us denote the central region which experiences the uniform phase gradient as GR. The wire starts in a topological phase at zero gradient and hence it supports two Majorana fermions at its extremities. The question to be tested is whether new Majorana

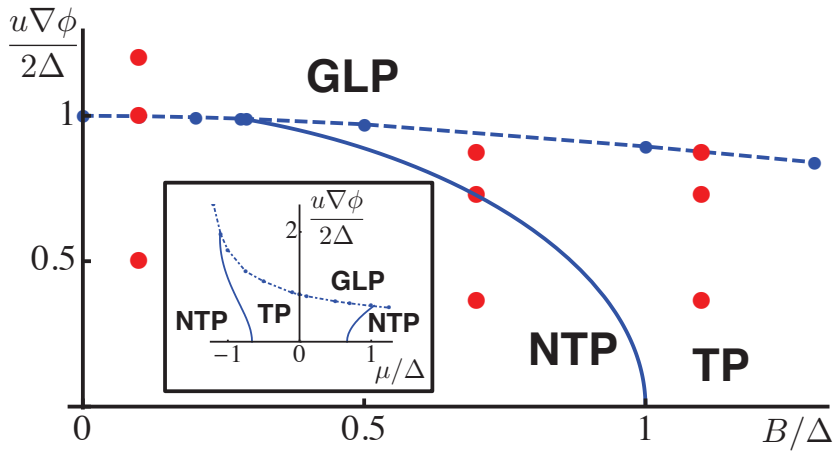

Fig. 5.10: Phase diagram of the spin-orbit coupled semiconducting wire in proximity to a superconductor, under a phase gradient $\nabla\phi$ (taken from Ref. [125]). B is the magnetic field (B_z), Δ the induced superconducting parameter, μ the chemical potential and u the spin-orbit coupling constant (α). The system presents gapped topological phases (TP) which support Majorana fermions and trivial phases without Majorana fermions. There are also gapless phases (GLP) (manifestly devoid of Majorana fermions). Central to the present study is the fact that starting from a topological phase (TP) at zero gradient it is impossible to enter a trivially gapped state through the action of the gradient alone; the gradient pushes the system into a gapless (nontopologial) phase.

fermions can form at the interface of the GR with the outer regions, or extended in the GR as in an SNS junction. Note that the above considerations allow us to eliminate the first possibility. Because $(\nabla\phi)_c > (\nabla\phi)_{gl}$, the system enters first a gapless regime, so there is no boundary to a trivially gapped phase at the edges of the GR. Inspecting the phase diagram in Fig. 5.10 indicates that this result is general in nature. *Always* an increasing phase gradient pushes the system from a topologically gapped phase to a gapless regime and therefore no localized Majorana bound states are expected.

If the transition takes place to a gapless phase, then it still remains open the possibility that Majorana fermions could form as extended states in GR. However the gradient has a particle-hole breaking effect[76, 125] and, moreover, losing the protection of the bulk gap leads to the destruction of Majorana fermions even for phase gradient values above $(\nabla\phi)_c$. In Fig. 5.11(a) the phase gradient over the 20 central sites is $\pi/20$, smaller than the $(\nabla\phi)_{gl}$ value and the GR remains topologically gapped. There is an unique topological phase in the system and hence there are only two Majorana states which form at the wire ends. Because of the relative phase $\phi = \pi$ between the two outer regions, the Majorana fermions have identical Majorana polarizations. Increasing the gradient has the effect to push the system in a gapless regime and to drastically diminish the gap to the first excited states in the GR, however no Majorana fermions form in the GR.

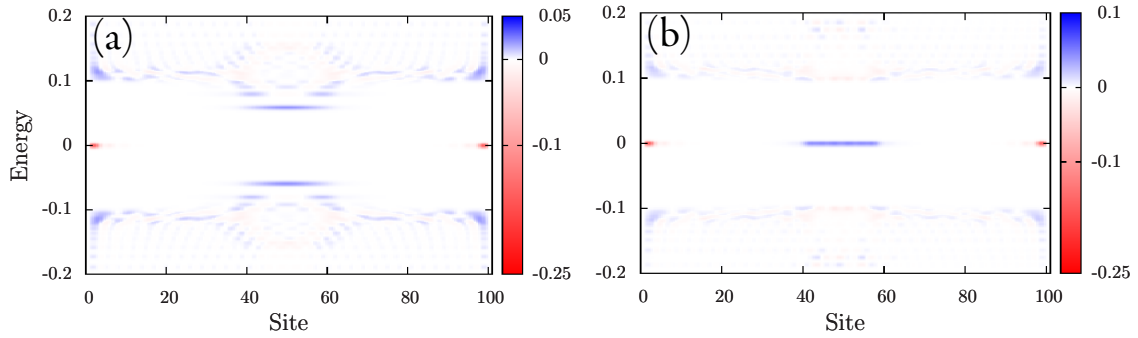

Fig. 5.11: (a) The phase of the superconducting parameter is twisted by π over 20 central sites. The central regions remains topologically nontrivial and Majorana fermions with the same polarization form only at the ends of the wire. (b) Phase gain of 11π over 11 sites. Two Majorana fermions form in the GR having an opposite polarization with respect to the end modes.

Nevertheless, there is one special case in which Majorana fermions can form in the GR. This situation arises when the GR is constructed as a series of Josephson junctions with a phase increase of $(2n+1)\pi$ between two neighboring sites, with n being an integer. The GR must consist of an odd number of sites, to ensure a relative phase difference $(2n'+1)\pi$ between the left and right regions. Then extended Majorana fermions form in the GR. This situation is exemplified in Fig. 5.11(b): two extended Majorana fermions form for a phase difference of $\phi = 11\pi$ over an 11-site GR. Integrating the Majorana polarization over the central region yields a total value of one, showing that only two Majorana states form in this region. This limit case is the only one where Majorana fermions are formed as extended states in the GR. Naturally it is difficult to expect that such strong gradient and such particular conditions can be found in a physical system.

It is noteworty to point the general fact that the system is invariant under a change of 2π in the phase gradient. Hence for an N-site GR, there is a $2\pi N$ periodicity in the total relative phase ϕ between the left and right ends of the wire. In the special case when the gradient is over an odd number of sites with Majorana fermions forming at $\nabla\phi = (2n+1)\pi$, the periodicity in the total phase is $4\pi N$ (see in Fig. 5.12(a)).

5.4.2 Ring with a uniform phase gradient

Let us investigate the presence of Majorana fermions in the ring geometry from Fig. 5.9(b). The phase of the superconducting phase is twisted with a phase gradient $\nabla\phi$. The question is under what conditions do Majorana fermions form in the normal region.

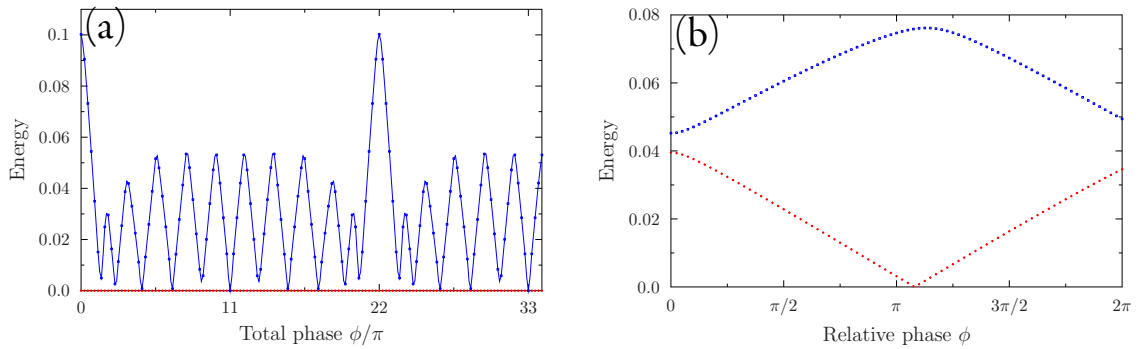

Fig. 5.12: (a) Evolution of the first two positive eigenvalues with the phase difference ϕ for a 11-site GR. The constant zero-energy mode corresponds to an end Majorana state. The energy of the other mode evolves with ϕ and reaches zero only when there is a $(2n+1)\pi$ phase difference between two neighboring sites (this happens here for $n=0$ and $n=1$, corresponding to $\phi=11\pi$ and respectively $\phi=33\pi$). (b) Evolution of the lowest-energy modes with the phase difference ϕ. Note the shift $\delta\phi$ from the expected formation of Majorana fermions at π.

The tight-binding Hamiltonian describing the system reads

$$H=\sum_{j\in\circlearrowleft}\left\{C_j^\dagger[(t-\mu)\tau_3+B_z\sigma_3]C_j-\frac{1}{2}\left[C_j^\dagger(t+i\alpha\sigma_2)\tau_3C_{j+1}+\text{H.c.}\right]\right\}$$
$$-\sum_{j=N_1}^{N_2}C_j^\dagger\Delta e^{-i\phi_j}\tau_1C_j. \tag{5.16}$$

The first sum runs over the entire ring ($\circlearrowleft$), while the second sum runs over the superconducting region between the sites N_1 and N_2. In the superconducting region the phase grows under a uniform gradient $\phi_j=\phi_{j-1}+\nabla\phi$.

While no Majorana states are formed at $\phi=0$, for peculiar values of the phase difference accumulated over the superconducting region, and for phase gradients that are not too large, Majorana fermions can form in the normal region. This can be seen in Fig. 5.12(b), where are plotted the low-energy eigenvalues as a function of the total phase difference. In principle, when the accumulated phase is π, the would-be Majorana states are of opposite type and could exist as extended modes in the normal region. Nevertheless, note that in simulations the Majorana fermions form at a phase difference slightly larger than π (see Fig. 5.12(b)). Such deviation from π can be attributed to finite size effects and to the communication of the zero modes through the superconducting region.[67] In numerical simulation, Majorana fermions form at $\pi+\delta\phi$ and the shift $\delta\phi$ decreases with system size. The Majorana polarization is plotted at this particular value in Fig. 5.13(a). Integration of the polarization shows that the two zero energy modes have the same polarization, which is adding up to a value of one.

This $2(\pi+\delta\phi)$ periodicity in the formation of Majorana fermions is preserved for gra-

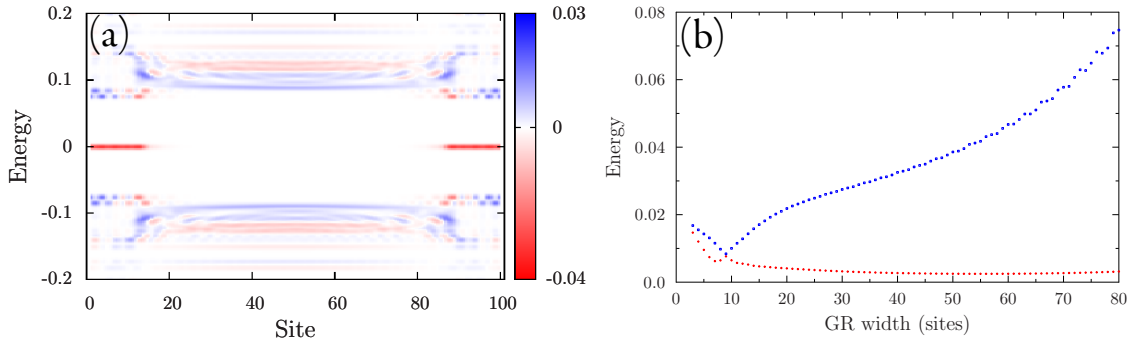

Fig. 5.13: (a) Majorana polarization as a function of energy and position for a ring with a total phase difference of $\pi + \delta\phi$. The system is periodic with site first and last site equivalent. Extended Majorana modes form over the entire normal region. (b) First two positive eigenvalues for a decreasing GR length. The total phase difference is kept at $\phi = \pi$, while the number of sites is varied. Close to the critical value of the gradient $(\nabla\phi)_{gl} = 0.27 \simeq 11.6$, the system passes into a gapless regime. Due to finite-size effects the numerical analysis recovers this transition at a smaller value than the expected 11 or 12 sites.

dients smaller than the critical gapless transition gradient $(\nabla\phi)_{gl} = 0.27$, corresponding to a total phase difference of $\phi \simeq 21.6\pi$. As described above, larger gradients are predicted to drive the GR to a gapless regime. However, numerical simulations indicate that while larger gradient values do seem indeed to take the system into the gapless phase, Majorana fermions may still form for peculiar gradient values; at this point we do not understand the origin of this phenomenon.

Another way to illustrate the evolution of the system with the value of the phase gradient is to fix the total phase gain $\phi = \pi$, and to study the behavior of the low-energy modes with the number of sites in the GR (a larger number of sites is equivalent to a smaller phase gradient). As it has been illustrated in Fig. 5.12(b), due to finite size effects, one has an minigap for the would-be Majorana states; the energy gap for this mode becomes smaller and smaller with increasing the number of sites. When the number of sites is reduced, the constraint of constant total phase ϕ drives the system to larger and larger gradients. Thus it is possible to attain the critical value of the phase gradient that signals the passing of the system into the gapless phase. For an infinite system this is $(\nabla\phi)_{gl} \simeq 0.27$, corresponding to $\pi/11.6$. Thus a phase transition is expected when GR reaches the size of $11 - 12$ sites. Indeed a crossing of the bands and lifting of the low-energy modes happens for a size of the GR of about 9 sites (see Fig. 5.13(b)).

5.5 Discussion

The present chapter has studied the behavior of Majorana modes in several SN and SNS junction constructed from semiconducting spin-coupled wires in proximity to an s-

wave superconductor. Throughout, it was shown that coupling Majorana modes to a normal metal can lead to extended Majorana modes in the latter. The extension of the modes is controlled by the penetration length ξ_p of superconductivity in the normal region. Increasing the penetration length leads to a reduction of the normal region. In the limit of a penetration length larger than the normal region size, the system becomes effectively a topological superconductor with localized Majorana fermions.

In the context of SNS junction, it was shown how Majorana polarization can be used to illustrate the physics of the fractional Josephson effect. The superconducting phase leads to a rotation of Majorana polarization. In this manner, the extended Majorana fermions forming at a phase difference $\phi = \pi$ have the same polarization and do not hybridize to form Andreev bound states.

Finally, cases with a uniform gradient in the induced superconducting phase were treated in linear and ring geometries. In the linear case, a topological superconductor in a nontrivial phase had a central region subjected to a uniform gradient. However it was impossible to induce Majorana fermions at the interfaces with the outer regions. The central region could not be turned into a trivially gapped phase due to the fact that the system always enters first into a gapless regime. Hence the possibility to have localized Majorana fermions at the interface is excluded. Moreover, the gradient has a Cooper pair-breaking effect and without the protection of the bulk gap there are no extended Majorana fermions in the "normal" region. Extended modes were shown to exist only in the case where the total phase gain is an odd multiple of π and, simultaneously, the gradient changes by π from site to site. Then the system behaves as a series of short Josephson junction each at phase difference $\phi = \pi$.

In the case of the ring geometry carrying a "normal" region, it was shown that the uniform gradient can twist the phase in the topological superconducting region such that its two ends have a difference of π. Then the system maps to a regular SNS junction and extended Majorana modes form in the normal section. Finite size effects produce a shift $\delta\phi$ from the ideal value $\phi = \pi$. It remains in the future to investigate the presence of Majorana fermions at higher gradient values above the transition into the gapless regime; these are not predicted by the theory and do not seem to arise with the periodicity $2(\pi + \delta\phi)$.

Chapter 6

Multiple Majorana fermions in a two-band model

The spin-coupled semiconducting wire studied in the previous chapters supports $\mathbb{Z}_2$ topological phases, where Majorana modes appear due to proximity effect to an s-wave superconductor. The index $\mathbb{Z}_2$ means the Majorana fermions are essentially solitary zero bound modes living at the interface of the wire with the vacuum. They are lifted from zero energy through coupling with another Majorana fermion and they form a regular complex fermion. Is it possible to have multiple Majorana living in proximity to each other in a 1D wire? This question has recently received a clear positive answer. In Ref. [126] it was shown that in the class of chiral topological superconductors BDI, one can in principle have a system described by a $\mathbb{Z}$ topological invariant (see Tab. 1). Therefore multiple Majorana fermions could be accommodated at the ends of a wire. The possibility was made more concrete when a simple two-band tight-binding superconducting model for spinless fermions in the BDI class was shown to hold two Majorana modes [127].

In the present chapter the model proposed in Ref. [127] is treated as an ideal model on par with the Kitaev model. It is actually an extension of Kitaev model with the crucial modification that there are next-nearest-neighbor hoppings and superconducting parings in the model. Through simple arguments it is shown here that this is generally a sufficient condition to allow for multiple Majorana fermions localized at an edge.

Furthermore, here are investigated the specific signature due to presence of multiple Majorana fermions. For once the presence of several Majorana fermions at one edge of the superconducting wire opens several Andreev transport channels in SN junctions and therefore the conductance can reach the value $2e^2/h \times Q$ with $Q \in \mathbb{Z}$ [128]. However, the focus here is on the question whether the fractional Josephson effect, for Josephson junction connecting wires which support multiple Majoranas, survives and the anomalous 4π-periodicity of the phase/current dependence is maintained.[129]

Finally, the possibility to create new Majorana modes through the addition of a uniform superconducting phase gradient in the central region of the 1D wire is explored.

The gradient can locally push the system in a non-trivial $\mathbb{Z}_2$ phase, while the rest of the system remains a topologically trivial $\mathbb{Z}_2$ (but nontrivial $\mathbb{Z}$). Then new Majorana fermions form at the interfaces with the uniform gradient region, while multiple Majorana modes can subsist at the end of the wire.

Before analyzing the properties of $\mathcal{H}$, let us provide some general symmetry arguments which explain why a general 1D Hamiltonian can sustain phases with more than one Majorana end states.

6.1 Topological properties of a two-band BDI topological superconductor

6.1.1 Symmetry constraints

A 1D superconducting system can have multiple Majorana bound states at its ends when the system exhibits particle-hole symmetry and, crucially is also time-reversal invariant (TRI) [126, 127]. For the two-band Bogoliubov-de Gennes (BdG) Hamiltonian presented here, this can be seen from the following simple argument. A general two-band BdG Hamiltonian $\mathcal{H}$ obeys PHS by construction, and can be written in the particle hole basis as

$$\mathcal{H} = \mathbf{h} \cdot \boldsymbol{\tau}, \tag{6.1}$$

where τs are the Pauli matrices in the particle-hole space. Note that under PHS symmetry the components of the vector Hamiltonian $\mathbf{h}$ observe

$$\begin{aligned} h_1(k) &= -h_1(-k), \\ h_2(k) &= -h_2(-k), \\ h_3(k) &= h_3(-k). \end{aligned} \tag{6.2}$$

The time reversal operator for spinless fermions is just the complex conjugation operator. Hence, if the system is TRI, the components of $\mathbf{h}$ obey the following constraints:

$$\begin{aligned} h_1(k) &= h_1(-k), \\ h_2(k) &= -h_2(-k), \\ h_3(k) &= h_3(-k). \end{aligned} \tag{6.3}$$

Particle-hole and time-reversal symmetries impose the chiral symmetry represented by the operator τ_1 which anti-commutes with the Hamiltonian

$$\{\mathcal{H}, \tau_1\} = 0. \tag{6.4}$$

If $\mathcal{H}$ obeys all these symmetries, then it follows that h_1 must vanish. Hence $\mathcal{H}$ has only two remaining components and, therefore, $\hat{\mathbf{h}}$ defines a mapping from the Brillouin Zone

(BZ) to the Bloch "circle"

$$\hat{\mathbf{h}} : T^1 \to S^1. \tag{6.5}$$

Hence the mapping is characterized by a winding number w which is an integer [126]. Therefore a two-band BdG Hamiltonian belongs to the topological BDI class characterized by a $\mathbb{Z}$ topological invariant [11–13].

6.1.2 Winding number of a circuit and role of distant site couplings

The form of the winding number will give an insight to how can one increase the number of Majorana fermions by adding distant-site coupling terms in the Hamiltonian. Let us clarify the computation of the winding number of a closed curve around the origin in the 2D plane; the curve is a mapping $f : T^1 \to \mathbb{R}^2\backslash\{0\}$. By components the curve reads $f(t) = (x(t), y(t))$. Let t parametrize this curve with $t \in [0, 2\pi)$. Then the winding number w of the curve around the origin in $\mathbb{R}$ reads

$$w = \frac{1}{2\pi}\int_0^{2\pi} dt \frac{x\dot{y} - \dot{x}y}{r^2}, \qquad r^2 = x^2 + y^2. \tag{6.6}$$

The winding number can be computed using the Brouwer degree of a curve [45]. In the case that the kernel of function $x(t)$ has a finite number of points t, the winding number reduces to

$$w = -\frac{1}{2}\sum_{t\in \ker x} \operatorname{sgn}\big[\dot{x}(t)y(t)\big]. \tag{6.7}$$

An equivalent formula for the winding number can be produced where now one uses a sum over the zeros of $y(t)$.

In the case of a general TRI, BdG Hamiltonian presented in the previous subsection, the winding number is

$$w = -\frac{1}{2}\sum_{k\in \ker h_2} \operatorname{sgn}[\partial_k h_2 h_3]. \tag{6.8}$$

Note from the symmetry constraints that the kernel of h_2 contains at least the special BZ points 0 and π. To create more Majorana bound states at one end, the winding number must satisfy $|w| > 1$. This implies that $\ker h_2$ must contain other points than 0 and π. This can happen by enlarging the unit cell through the addition of hopping and superconducting pair terms coupling distant sites. Then new nodes in the energy dispersion develop for $k \in [0, \pi]$ and can lead to higher winding number. Hence the presence of higher-order hopping or pairing terms is a sufficient condition to have multiple Majorana bound states at the ends of a 1D wire.

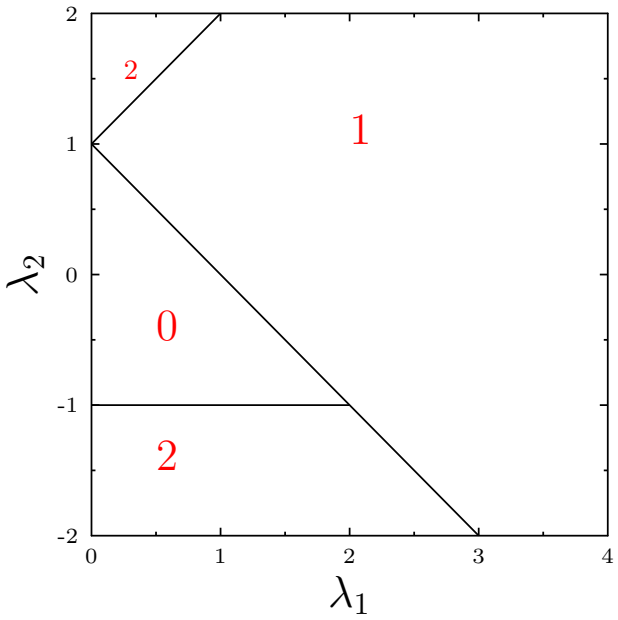

Fig. 6.1: Phase diagram for the Hamiltonian in Eq. (6.9). The insulating phases are separated by black lines. Each insulating phase is characterized by a winding number w in red. The number of Majorana fermions bound at one end is given by $|w|$.

6.2 Model Hamiltonian and phase diagram

The model proposed in Ref. [127] is a two-band tight-binding model for spinless electrons. The Hamiltonian reads

$$H = \sum_i \big[-(1-2c_i^\dagger c_i)\mu - \lambda_1(c_i^\dagger c_{i+1} + c_i^\dagger c_{i+1}^\dagger + \text{H.c.}) \\ - \lambda_2(c_{i-1}^\dagger c_{i+1} + c_{i+1}^\dagger c_{i-1}^\dagger + \text{H.c})\big], \tag{6.9}$$

where λ_1 corresponds both to the nearest-neighbor (NN) hopping amplitude and to the nearest-neighbor superconducting gap while λ_2 denotes the next-nearest-neighbor (NNN) hopping amplitude and next-nearest-neighbor superconducting gap. In what follows, λ_1 is assumed positive. The chemical potential μ is set to one in the following. When $\lambda_2 = 0$, the Hamiltonian in Eq. (6.9) corresponds to the Kitaev model [67].

The phase diagram of H has been established in Ref. [127]. Here we recover this phase diagram in a different manner, by using Eq. (6.8) to unambiguously characterize each topological phase in the (λ_1, λ_2) plane. This phase diagram is drawn for completeness in Fig. 6.1.

The phase diagram associated with H is characterized by phases with $w = 0, 1, 2$. Indeed, for $\lambda_2 > 1 + \lambda_1$ or $\lambda_2 < -1$ and $\lambda_2 < 1 - \lambda_1$, H can sustain a phase with two Majorana zero modes localized at each wire end [127].

6.3 Transport in SN junctions

Before analyzing the physics of Josephson junctions made with wires supporting several Majorana fermions, let us focus on an SN junction for a superconductor described by the Hamiltonian H in Eq. (6.9). For a junction between a wire with one Majorana end state and a normal metal, it has been predicted that the differential conductance exhibits a zero-bias peak of height $2e^2/h$ [103, 104]. A similar question for a junction between a topological superconducting wire characterized by a topological index $w > 1$ and a normal metal has been recently addressed in Ref. [128]. The authors have shown that for such junctions the conductance G can reach a value of $G = |w| \times 2e^2/h$. This prediction is checked here by considering a junction between a wire described by Eq. (6.9) supporting 4 Majorana fermions, 2 at each of its extremities, and a normal wire.

The low-energy properties of such a system are determined by the coupling of the two end Majorana fermions with the normal metal. This coupling can be captured by a 2×2 hybridization matrix $\mathbf{\Gamma}$. In order to compute the low-bias transport properties of this junction, one can directly use the S-matrix formalism developed by Flensberg [104], and noting that the two wave-functions for the Majorana fermions are orthogonal [127], such that there is no inter-Majorana coupling term.

The resulting expression for current can be written as [104]

$$I = \frac{e}{h} \int d\omega M(\omega)[f(-\omega + eV) - f(\omega - eV)], \tag{6.10}$$

where $M(\omega) = \mathrm{Tr}[\mathbf{G}^R(\omega)\mathbf{\Gamma}\mathbf{G}^A(\omega)\mathbf{\Gamma}(\omega)]$, and $\mathbf{G}^R(\omega) = 2[\omega\mathbf{1} + 2i\mathbf{\Gamma}]^{-1}$ denotes the retarded Green's function. The differential conductance becomes

$$\frac{dI}{dV} = -\frac{e^2}{h} \int d\omega M(\omega) \left[\frac{df(-\omega + eV)}{d\omega} - \frac{df(\omega - eV)}{d\omega} \right]. \tag{6.11}$$

which at $T = 0$ reduces to

$$\frac{dI}{dV} = \frac{2e^2}{h} M(eV). \tag{6.12}$$

Taking an explicit trace over the transmission matrix, it follows that

$$\frac{dI}{dV} = \frac{8e^2}{h} \frac{8\det(\mathbf{\Gamma})^2 + (eV)^2 \mathrm{Tr}(\mathbf{\Gamma}^2)}{[(eV)^2 - 4\det(\mathbf{\Gamma})]^2 + [2eV\mathrm{Tr}(\mathbf{\Gamma})]^2}, \tag{6.13}$$

which at zero bias becomes

$$\frac{dI}{dV} = \frac{4e^2}{h}. \tag{6.14}$$

The zero-bias value of the differential conductance is thus the double of that expected for a junction with a single Majorana fermion at the interface. This is consistent with each interface Majorana contributing a $2e^2/h$ to the total conductance.

6.4 Josephson junctions

In this section, it is analyzed how the Jospehson effect is affected by the presence of several Majorana zero modes. In particular, only short Josephson junctions are considered between two wires which can sustain several Majorana end states. The model Hamiltonian reads

$$H = H_L + H_R + H_T. \tag{6.15}$$

The Hamiltonian for the left wire, H_L, is described by the Hamiltonian H in Eq. (6.9) characterized by parameters $(\lambda_1^L, \lambda_2^L)$. The right wire is characterized by H_R, which is obtained from H_L by changing $(c_i^\dagger c_j^\dagger \to c_i^\dagger c_j^\dagger e^{i\phi})$ in Eq. (6.9). Note that the same variable phase ϕ is attached to the NN and NNN pairing terms. The second wire is characterized by the parameters $(\lambda_1^R, \lambda_2^R)$. The tunneling Hamiltonian can be modeled as

$$H_T = -(\lambda_1^L c_N^\dagger c_{N+1} + \lambda_2^L c_{N-1}^\dagger c_{N+1} + \text{H.c.}), \tag{6.16}$$

where the junction is made between site N (last of H_L) and $N+1$, (first of H_R). By convention the hopping/pairing of the tunneling Hamiltonian are taken identical to the ones in the left wire.

Each wire is labeled by a topological index $w^\alpha = 0, 1, 2$ with $\alpha = L, R$. The absolute value of the winding number indicates the number of Majorana fermions at one end in each wire, taken separately. It is useful to think about the junction as formed by bringing adiabatically the wires together. The low-energy physics of the junction reduces to an analysis of the coupling of the several Majorana modes across the junction, as presented in Fig. 6.2. In the figure are illustrated the various $w^L - w^R$ junctions that are being treated in the following: the $1-1$, $1-2$ and $2-2$ junctions. The numerical simulations are made on a 100-site system with the junction at site 50.

Before analyzing the Josephson effect in junctions made from wires supporting multiple Majorana fermions, one may ask if a complex superconducting order parameter in a topological superconducting wire can have an effect on its phase diagram. However, while $H_R(\phi)$ is generically complex, an uniform phase ϕ can be gauged away, yielding a real Hamiltonian and the same phase diagram as the one depicted in Fig. 6.1.

6.4.1 The $1-1$ Josephson junction

Let us consider first a Josephson junction between two wires with a topological index $w^\alpha = 1$. This type of junction has been extensively studied and the model is checked here that it is consistent with the known physics. The model parameters are chosen as $(\lambda_1^\alpha, \lambda_2^\alpha) = (1, 1)$. Our numerical results for the dependence of the energy levels of this junction with the phase difference recover a 4π periodicity consistent with the anomalous Josephson effect (see Fig. 6.3(a)).

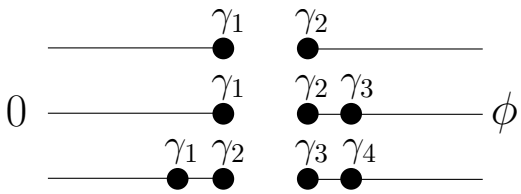

Fig. 6.2: To form Josephson junctions, wires characterized by winding numbers $1-1$, $1-2$ and $2-2$ are brought into contact. Without loss of generality, the left-hand side superconductor has real order parameters, while on the right-hand side they have a superconducting phase ϕ. The low-energy Hamiltonian is assumed to contain only phase-dependent coupling terms between the Majorana fermions.

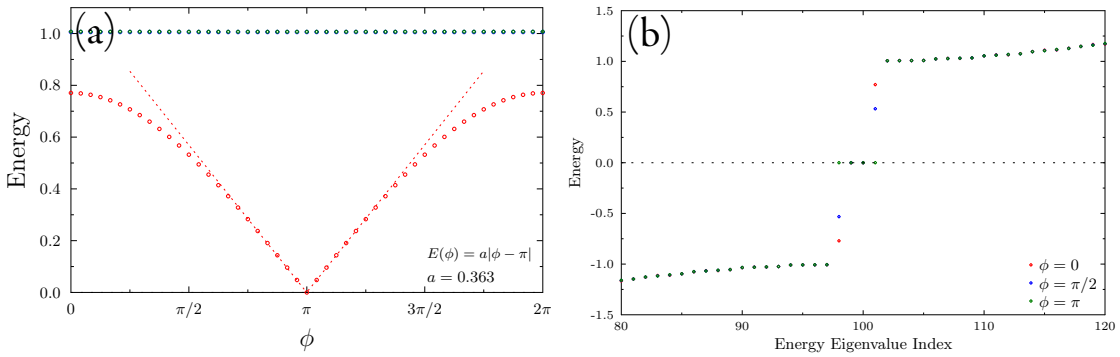

Fig. 6.3: (a) The dependence of the lowest-energy eigenvalues on the superconducting phase difference between the two wires. (b) The eigenvalue spectrum for three different values of $\phi = 0, \pi/2, \pi$. The system exhibits four zero-energy modes at $\phi = \pi$. Model parameters are $\lambda_1 = 1$ and $\lambda_2 = 1$

In Fig. 6.3(b) it is plotted the eigenvalue spectrum of the junction for $\phi = 0, \pi/2, \pi$. Only for $\phi = \pi$ one recovers four zero-energy eigenvalues which corresponds to four Majorana fermions: one at each extremity and two at the junction.

The 4π-periodicity can be understood from a simple effective low energy Hamiltonian following Kitaev [67]. The overlap between the wave functions of the two Majorana fermions at the extremities with the Majorana fermions at the interface is neglected. The simplest low-energy effective Hamiltonian reads [24, 67, 102, 119–121, 130, 131].

$$H_{\text{eff}}^{1-1} = it_{12}\cos(\phi/2)\gamma_1\gamma_2, \tag{6.17}$$

where γ_1 is a Majorana fermion at the right end of the first wire, and γ_2, a Majorana fermion localized at the left end of the second wire. Here t_{12} is the effective tunneling amplitude (see Fig. 6.2). One can check that the cosine behavior reproduces well the low energy spectrum. It is worth emphasizing that $i\gamma_1\gamma_2$ is trivially a conserved quantity of H_{eff}^{1-1}.

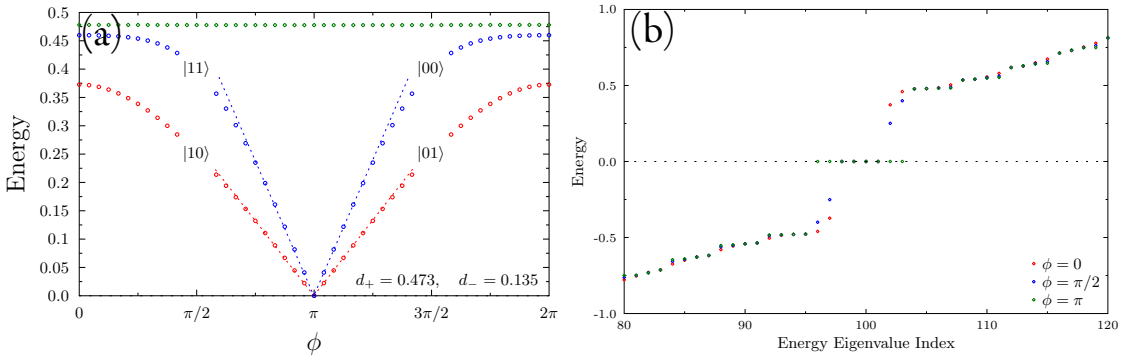

Fig. 6.4: (a) The dependence of the lowest-energy eigenvalues on the SC phase difference between the two wires. The energy branches are labeled using the occupation number representation for the two-fermion states formed from fusing four Majoranas across the junction. At low energy the two energy branches are linearly fitted: $E_+^{2-2} \pm E_-^{2-2} = (d_+ \pm d_-)|\phi - \pi|/2$ and the value off coefficients $d_\pm$ is displayed. (b) The eigenvalue spectrum for three different values of $\phi = 0, \pi/2, \pi$. The system exhibits eight zero-energy modes at $\phi = \pi$.

6.4.2 The $2-2$ Josephson junction

Let us now consider a junction between two superconducting wires characterized by winding numbers $w^\alpha = 2$.

Analysis of the spectrum

The eigenvalue spectrum for a $2-2$ junction is computed numerically. The result is shown in Fig. 6.4(b). The first important thing to note is that the anomalous 4π-periodicity still holds. The only difference is that there are now four Majorana fermions forming at the junction when the phase difference is $\phi = \pi$. At each extremity of the system there are also two Majorana fermions which subsist for any value of ϕ, making the ground state eight-fold degenerate at $\phi = \pi$ (see Fig. 6.4(b)).

A low-energy Hamiltonian capable to describe the numerical results presented in Fig. 6.4 must involve four Majorana fermions. Let us denote by γ_1, γ_2 the Majorana fermions on the left side of the junction and by γ_3, γ_4 the Majorana fermions on the right side of the junction. A general Hamiltonian involving the four Majoranas can be written as

$$H_{\text{eff}}^{2-2} = i\gamma_1(t_{13}\gamma_3 + t_{14}\gamma_4)\cos\frac{\phi}{2} + i\gamma_2(t_{23}\gamma_3 + t_{24}\gamma_4)\cos\frac{\phi}{2} + it_{34}\gamma_3\gamma_4\sin\phi + it_{12}\gamma_1\gamma_2\sin\phi. \tag{6.18}$$

The phase dependence of H_{eff}^{2-2} is fixed by enforcing a 2π-periodicity together with the constraint that for $\phi = 0$ there is no direct coupling between γ_1 and γ_2, nor between γ_3 and γ_4. The $\cos(\phi/2)$ is required by gauge invariance. Here are formally included

some direct-tunneling terms between the Majorana fermions on the same side of the junctions (t_{12} and t_{34}), which may be non-zero when $\phi \neq 0, \pi$ (this explains the $\sin(\phi)$). However, one can argue that such terms must be less significant since they are the result of higher-order hopping processes between the two superconductors. In fact these terms turn out to be negligible for the description of the low-energy spectrum.

Contrary to the $1-1$ junction, where there was an obvious quantity commuting with the Hamiltonian for all values of ϕ, for the $2-2$ junction this is not obvious for $\phi \neq \pi$. In the later case, there are four Majorana fermions fusing to form two regular fermions $c_\pm$. This can be seen from the spectral decomposition of the effective Hamiltonian

$$H_{\text{eff}}^{2-2} = E_+^{2-2}(2c_+^\dagger c_+ - 1) + E_-^{2-2}(2c_-^\dagger c_- - 1), \tag{6.19}$$

where

$$E_\pm^{2-2} = d_\pm \cos(\phi/2), \tag{6.20}$$

with $d_\pm = \frac{1}{2\sqrt{2}}\sqrt{b \pm \sqrt{b^2 - 4a^2}}$ with $a = t_{14}t_{23} - t_{13}t_{24}$ and $b = t_{13}^2 + t_{14}^2 + t_{23}^2 + t_{24}^2$.

Note that even if the f_{22} term in Eq. (6.18) was neglected, the form of the $c_\pm$ fermions as a function of the original Majorana fermions remains complicated. For example, under the reasonable assumption that the coupling strength between Majorana fermions situated at the same distance across the junction is identical, $t_{13} = t_{14}$, if follows that

$$\begin{aligned} c_\pm &= \frac{1}{\sqrt{2 + 2g_\pm^2}}[\gamma_4 + i\gamma_1 + g_\pm(\gamma_3 + i\gamma_2)], \quad \text{with} \\ g_\pm &= \frac{1}{2t_{13}}\left[t_{23} - t_{14} \pm \sqrt{4t_{13}^2 + (t_{14} - t_{23})^2}\right]. \end{aligned} \tag{6.21}$$

However the Hamiltonian and the occupation numbers of the two fermions $n_\pm = c_\pm^\dagger c_\pm$ trivially commute among each other. The occupation numbers for the two fermions are conserved and one can use Eq. (6.19) to label the energy branches in the occupation number representation of the two-particle states, $|n_+ n_-\rangle$ (see Fig. 6.4).The value of $E_\pm^{2-2}$ can be found numerically from a linear fit at low energy near $\phi = \pi$ in Fig. 6.4. Most importantly, the 4π periodicity of the DC Josephson effect is maintained.

Analysis of the Majorana polarization

A useful tool to analyze the behavior of Majorana fermions is the Majorana polarization, a local topological order parameter introduced in Ref. [111] and related to the degree of anomalous pairing in a 1D topological wire.

The existence of a Majorana fermion is recorded as a zero-energy Majorana polarization density of 0.5. A Majorana fermion can have a x- and y-Majorana polarization. When the Hamiltonian is real at $\phi = 0$ and $\phi = \pi$, the y-Majorana polarization P_{M_y} is 0. When the superconducting parameter acquires a phase, the polarization along the y-direction is generally nonzero.

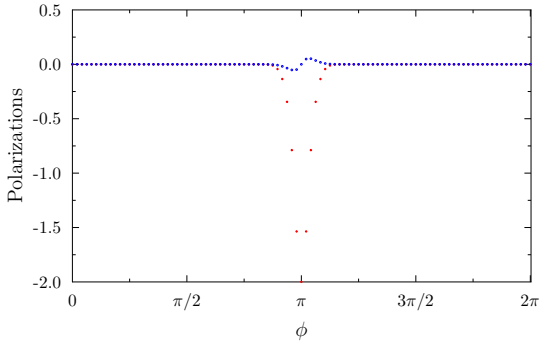

Fig. 6.5: Zero-energy Majorana polarization integrated over the 40 sites around the junction. Four Majorana states form at the junction for $\phi = \pi$ yielding a x-Majorana polarization of 2, and compensating the Majorana polarization of the four end bound state.

Here, similar to Ref. [122], the end Majorana fermions respond to the variation of ϕ by rotating their Majorana polarization. This is due to the superconducting parameter becoming complex. However at $\phi = \pi$ the superconducting parameter becomes real again and the zero-energy end states have the same Majorana polarization. For this particular value of the phase, four new Majorana fermions form at the junction, two in each wire, their x-Majorana polarization compensating the Majorana polarization of the end modes (see Fig. 6.5).

6.4.3 The $1-2$ Josephson junction

In the following, the focus is on the remaining $1-2$ junction. This is a particularly interesting problem since two distinct topological sectors are brought into contact via a Josephson junction.

Analysis of the spectrum

The physics of this junction is expected to be dominated by three interacting Majorana fermions localized at the interface. One can show that for a winding number difference of one between the right side and the left side of the junction, one Majorana mode is bound at the interface for any choice of ϕ. Moreover, at $\phi = \pi$ the system is six-fold degenerate with three zero energy Majorana in the junction region (see Fig. 6.6(b)).

Let γ_1 denote the Majorana fermion on the left side of the junction, and by $\gamma_2,\ \gamma_3$ the Majorana fermions on the right side. The gauge invariance of the Hamiltonian suggests that the phase-dependent couplings between γ_1 and $\gamma_{2,3}$ are proportional to $\cos(\phi/2)$ to compensate the sign change. A low-energy Hamiltonian describing the Majorana coupling in the $1-2$ system can thus be written as

$$H_{\text{eff}}^{1-2} = i\gamma_1(t_{12}\gamma_2 + t_{13}\gamma_3)\cos\frac{\phi}{2} + it_{23}\gamma_2\gamma_3\sin\phi. \tag{6.22}$$

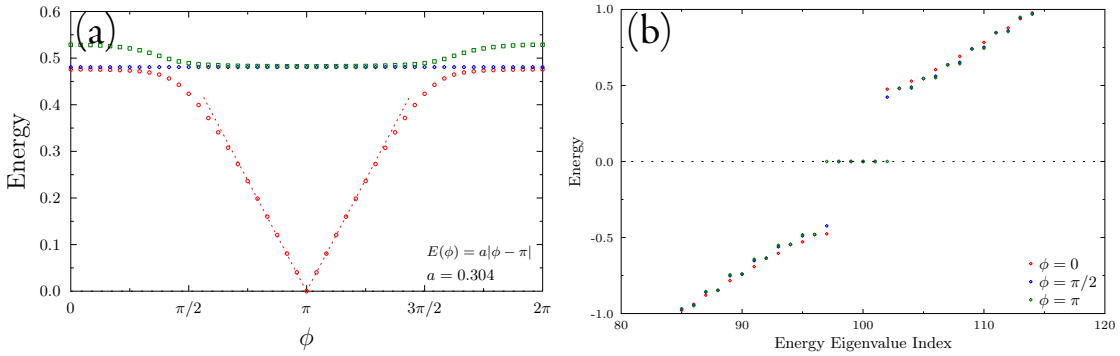

Fig. 6.6: (a) The dependence of the lowest-energy eigenvalues on the superconducting phase difference between the two wires. The dotted line indicate the fit of the lowest-energy numerical eigenvalue with the analytical form in E_+ from Eq. (6.23). The fit parameter is $a = \sqrt{t_{12}^2 + t_{13}^2}/4$. (b) The eigenvalue spectrum for three different values of $\phi = 0, \pi/2, \pi$. The system exhibits six zero-energy modes at $\phi = \pi$.

This Hamiltonian has three zero-energy eigenstates at $\phi = \pi$. For a phase difference of $\phi \neq \pi$, the effective Hamiltonian (6.22) has one zero eigenvalue (required by the anti-symmetry of the 3×3 matrix) and two non-zero eigenvalues. The constant zero-energy state, which is a Majorana edge state bound at the interface between two topologically nonequivalent regions, is the result of the difference of one unity between the topological indices of the two regions.

Similar to the $2 - 2$ junction, if the last term of Eq. (6.22) is neglected, the form for the two eigenvalues becomes

$$E_\pm = \pm 2a \cos(\phi/2). \tag{6.23}$$

The hopping dependent parameter $a = \frac{1}{4}\sqrt{t_{12}^2 + t_{13}^2}$ can be determined from a low-energy fit of the numerical dispersion presented in Fig. 6.6(a). Note that taking into account also the term t_{23} improves the quality of the fit, especially in the vicinity of the superconducting gap. Note also that, while the fit is accurate up to energies close to the superconducting gap, the effective Hamiltonian H_{eff}^{1-2} is exclusively a low-energy effective Hamiltonian and should not be expected to recover the full dependence of the energy eigenvalues on the superconducting phase difference.

Analysis of the Majorana polarization

In the left-side wire, described by a winding number $w = 1$, the superconducting parameter is chosen to be real and the single Majorana fermion at the left end is always fully x-polarized. For the right-hand side wire, at the right end there are two Majorana fermions that respond to the twisting of the phase ϕ by gaining a y-polarization; in Fig. 6.7(a) it is presented the behavior of the x- and y-polarizations of these modes.

Let us now analyze what happens at the junction between the two wires. At $\phi = \pi$ it is expected to have 3 Majorana fermions. For any other ϕ there is always at least one

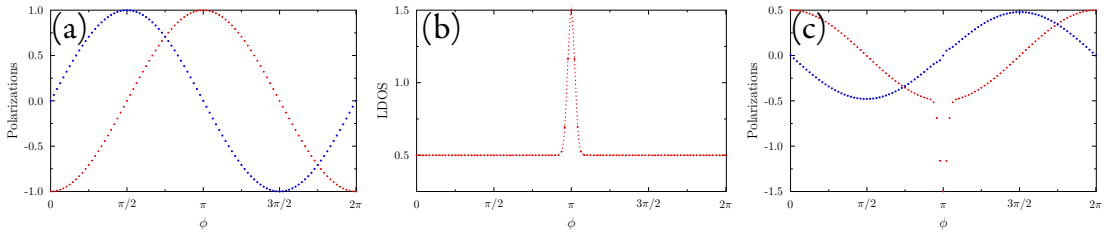

Fig. 6.7: (a) The Majorana polarization of the right-end Majorana fermions integrated over the last 30 sites. Note the oscillatory behavior of the x- (red) and y- (blue) Majoran polarization components with a total constant Majorana density of 2×0.5, corresponding to two rotating Majorana modes. (b) Zero-energy density of states integrated over the 40 sites around the junction point. (c) Zero-energy Majorana polarization integrated over the 40 sites around the junction. The $x-$polarization (red) and the $y-$polarization (blue). Three Majorana fermions having the same polarization are supported at the junction for $\phi = \pi$.

Majorana fermion stuck at the interface between the two topologically nonequivalent regions. This can be seen by plotting the zero-energy density of states, as well as the zero-energy Majorana polarization, integrated over the 40 sites around the junction. In Fig. 6.7(b) it is plotted the integrated zero-energy density of states. Note that for $\phi \neq \pi$ the density of states is constant and equal to 0.5 corresponding to a single Majorana mode bound at the junction. The sharp jump between 0.5 and 1.5 at $\phi = \pi$ describes the contribution of the two extra Majorana modes which reach zero energy at $\phi = \pi$ (these two extra zero-energy states appearing at $\phi = \pi$ can also be seen in the spectrum described in Fig. 6.6(b)). This is also confirmed by a plot of the zero-energy Majorana polarization, integrated over the 40 sites around the junction, in Fig. 6.7(c); the jump in the x-Majorana polarization at $\phi = \pi$ can be understood as coming from the two Majorana modes that develop at zero energy. Thus, at $\phi = \pi$ there are three Majorana fermions at the two extremities of the wire (one at the left end and two at the right end), fully x-polarized in the positive direction. These fermions are compensated by three Majorana fermions which form in the junction which are fully x-polarized in the opposite direction.

6.5 Wires with an inhomogeneous superconducting phase

As it was shown in Ref. [127], the system exhibits two Majorana modes at each end, provided that the time-reversal and chiral symmetries are not broken, namely as long as the system remains in the BDI class [12, 13]. Breaking time-reversal symmetry leads to the removal of the protection for two Majorana fermions since the system now belongs to the D symmetry class (see Tab. 1). Then the system can return to the more typical state with at most one Majorana fermion at each end.

Here it is explored a different way to break TRS, i.e. by adding a constant phase

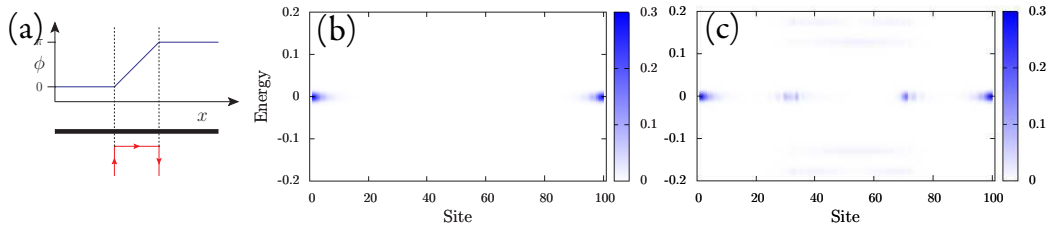

Fig. 6.8: A constant phase gradient over 40 sites twists the superconducting phase from 0 to π. (a) Schematic picture of the setup. Supercurrent in the bulk change the superconductor phase ϕ in the (black) wire from 0 to π. (b) The constant phase gradient removes four MBS in the middle region, leaving two MBS at each end, both x-polarized. (c) Majorana modes form at the ends of a 40 site central region driven in a nontrivial $\mathbb{Z}_2$ phase by a phase gradient $\nabla\phi = 2$.

gradient. Let us take a wire characterized by the topological index $w = 2$. Instead of an abrupt change in the superconducting phase, consider a long junction comprising a region in which the phase can vary smoothly with a constant phase gradient. On the left side of this long junction, the superconducting phase is assumed to be constant and equal to 0 while on the right side it is supposed to be constant and equal to $\phi = \pi$. The phase of the central region is supposed to vary smoothly from 0 to π; such a uniform phase gradient can be induced for example by the presence of supercurrents in the bulk of the superconductor. This situation is schematically depicted in Fig. 6.8(a). The phase gradient can be used to manipulate the creation or destruction of Majorana fermions [125].

Due to the phase gradient, the BdG Hamiltonian gains a TRS-breaking $h_1(k)$ odd component:

$$\begin{aligned} h_1(k) &= \lambda_1 \sin(k)\sin(\nabla\phi/2) + \lambda_2 \sin(2k)\sin(\nabla\phi) \\ h_2(k) &= -\lambda_1 \sin(k)\sin(\nabla\phi/2) - \lambda_2 \sin(2k)\cos(\nabla\phi) \\ h_3(k) &= 2 - 2\lambda_1 \cos(k)\cos(\nabla\phi/2) - 2\lambda_2 \cos(2k)\cos(\nabla\phi), \end{aligned} \tag{6.24}$$

where the gradient $\nabla\phi$ is the change of phase over one site. Note that a phase gradient also creates a non-vanishing h_0 component that multiplies the identity Pauli matrix. Although it is neglected in the following, it indicates the breaking of PHS and the tendency of the gradient to destroy Cooper pairs. This poses a conceptual problem: how are the Majorana fermions protected in case of a broken PHS? In fact numerical simulations show spurious zero modes that appear when the phase gradient is present.

Let us neglect for the moment the breaking PHS, as $h_0 \ll h_3$ when the gradient is small. The system is no longer characterized by a winding number w but instead by the Kitaev $\mathbb{Z}_2$ invariant [67]. Analyzing the topological invariant reveals that the system is in a topologically nontrivial phase if the condition

$$|1 - \lambda_2 \cos(\nabla\phi)| < |\lambda_1 \cos(\nabla\phi/2)| \tag{6.25}$$

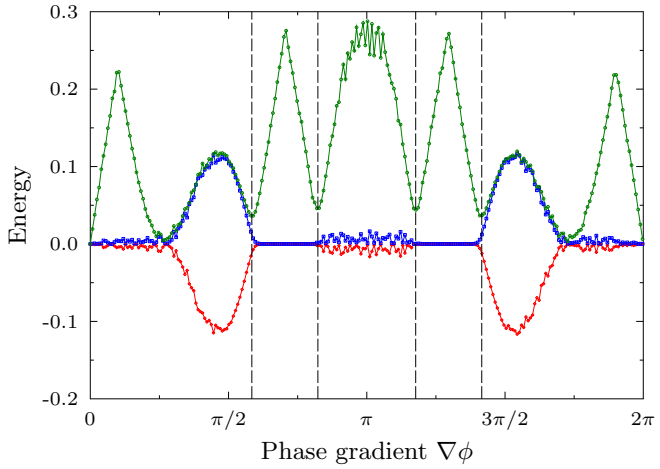

Fig. 6.9: Illustration of the first negative and the first two positive eigenvalues in a 100-site superconducting wire subjected in its entirety to a phase gradient that varies from 0 to 2π. Uniform disorder with a magnitude of $\sim$ 10% of the hopping strength λ_1 removes spurious zero modes leaving zero Majorana modes in the windows predicted by the topological condition (6.25) (marked with dashed lines). $\lambda_1 = 1$ and $\lambda_2 = -1.5$.

is satisfied. Note that at vanishing phase gradient, one recovers the phase diagram in Fig. 6.1, with the only change that $w = 2$ and $w = 0$ are both trivial $\mathbb{Z}_2$ phases.

Therefore adding a small phase gradient removes the Majorana fermions at the ends of the central region. This is due to the fact that locally both sides of the region are topologically $\mathbb{Z}$ trivial. However, at both ends of the wire, in the regions without a phase gradient, two Majorana modes continue to be present because they are locally protected by the time reversal symmetry.

In contrast, one can drive the central region to a topologically $\mathbb{Z}_2$ nontrivial state, by increasing the phase gradient. This happens when the inequality (6.25) is verified. Then the central region is connected to two $\mathbb{Z}_2$ trivial regions and one Majorana fermion forms at each interface. The pair of Majorana fermions persist at the ends of the wire (see Fig. 6.8(c)).

Due to the twist of the phase by π, the two Majoranas at the ends are both x-Majorana polarized in the same direction.

It is noteworthy to realize that the validity of the topological invariant can be questioned in the case where PHS is broken. However one can see that the topological invariant continues to hold true. In numerical simulations, a 100-site system, originally in the $w = 2$ topological phase, is subjected in its entirety to a uniform superconducting phase gradient wire. In Fig. 6.9 one can see that when the gradient is added the system becomes a trivial $\mathbb{Z}_2$ topological insulator, marked by the loss of the four-fold degeneracy near $\nabla\phi = 0$. Spurious modes near zero energy are removed by disorder, and two

robust Majorana modes develop in the window predicted by the topological invariant. At this moment, we lack an explanation of the origin of the spurious zero modes, or for the perplexing effectiveness of the $\mathbb{Z}_2$ topological invariant in the absence of the PHS symmetry. These problems deserve further research.

6.6 Discussion

The study of the Josephson effect between wires supporting multiple Majorana fermions has revealed that the 4π anomalous periodicity is maintained in junctions characterized by a sharp change of the superconducting phase. Moreover, a smooth phase gradient can be used to destroy the $\mathbb{Z}$ phase and to create Majorana fermions at the interface between trivial and nontrivial $\mathbb{Z}_2$ phases. Also a connection was made between the work on topological insulators with large Chern number and BDI class topological superconductors. For the two-band models studied, it was shown that a sufficient condition to create multiple zero-energy bound states at the edges of system is to add coupling terms between distant sites. Let us finally remark that the $\mathbb{Z}$ Majorana modes that appear in these system should be fragile when considered in realistic systems as the spin-orbit coupled semiconducting wire due to the necessity of time-reversal symmetry. The realization of Majorana fermions was shown to depend crucially on the presence of a time-reversal breaking magnetic fields that will naturally act to destroy the high $\mathbb{Z}$ phases.

Conclusion and Perspectives

Topological insulators and superconductors form a class of materials with a bulk gap in the energy spectrum, inhabited by exotic edge states. A topological invariant characterizes the bulk properties of these systems and it is subsequently reflected in the number of the edge states.

In the first part of the thesis, the investigation was centered around two-dimensional tight-binding topological insulators indexed by a Chern number. They are quantum anomalous Hall insulators that support an *arbitrary* number of edge states. However, large Chern number or, equivalently, multiple edge states are usually created by fashioning multiband systems. It was shown here that it is possible to vary the Chern number in simple two-band models by adding distant-neighbor hopping terms.

The key of the entire study lies in understanding that the topological invariant admits a discrete formulation. This allows to see an insulator as a "sum" of a gapless system with Dirac points plus a mass term. Crudely, the topological invariant reduces to a finite sum over the Dirac points weighed by the sign of the mass term. Therefore a necessary condition to increase the number of topological phases is to multiply the nodes in the energy dispersion. This can be realized by having hopping terms between distant sites. The consequences are explored in two models: a new artificial model with five Chern phases and also by adding distant-neighbor hopping in the Haldane model. The method allows one to obtain complete topological phase diagrams for the models.

There are two directions in which to extend the present study. The first consists in generalizing to multiband systems. Already two four-band model extensions are discussed: a $\mathbb{Z}_2$ insulator built from two Chern insulators and a "striped" $\mathbb{Z}$ topological insulator that can have large metallic phases. The second direction is to search for possible physical realizations of the model. The existence of extreme distant-neighbor hopping terms remains rather problematic; however multiband systems might effectively map to such models [37].

While the bulk admits general methods to easily discriminate between the topological phases, the edge-state investigations get quickly mired in details associated to the particular geometry of the edges. Moreover, the fact that there could be several edge states at an interface adds a new layer of difficulty to analytically finding the wave-function so-

lutions. Chap. 2 contains a detailed analysis of a situation in which there are at most two edge states at an interface. In perspective, one needs to generalize to edges of different geometries. Most importantly, one has to clarify the nature of edge states which form between topologically gapped phases with the same Chern number. Conceivably, the decomposition of a topological insulator in a gapless model plus a mass term could be used to extend previous studies of edge states in gapless systems [63, 64] to topological insulators.

The second part of the thesis revolves around the subject of Majorana fermions realized as quasiparticles in one-dimensional topological superconductors. There is a deep analogy to the previous study of topological insulators. The Majorana fermions are the "edge states" of topological superconductor and can be predicted from a knowledge of some bulk properties. They are predicted to emerge in a variety of condensed matter systems (see Sec. 3.2.1). However, Chaps. 4 and 5 are focused on a particular theoretical proposal distinguished by the simplicity of its ingredients. The Majorana fermions are predicted to appear as zero-energy excitations in a 1D spin-orbit coupled semiconducting wire under the effect of a magnetic field and in proximity to an s-wave superconductor [24, 25]. In Chap. 4, a Dresselhaus spin-orbit coupling term was added and it was shown that there is a spin texture to the electronic degrees of freedom that form the Majorana quasiparticle. They are spin-polarized in opposite direction in a transverse plane to the magnetic field. The exact direction is determined by the relative weights of Rashba and Dresselhaus spin-orbit couplings. This information could be used to detect Majorana fermions through the coupling to magnetic impurities. Nevertheless, it still remains to explicit this idea in the form of a complete experimental proposal.

Chap. 5 continued the study to superconductor-normal metal and long superconductor-normal metal-superconductor (SNS) junctions built from the semiconducting wire. The Majorana fermions can form as extended states into the normal part of the system. It was shown that the extension of the modes can depend on the coupling between the normal and superconducting regions and also that leaking of Cooper pairs into the normal metal can further localize the Majorana modes. In the SNS junction the Majorana fermions form only at phase difference π between the two superconductors, otherwise would-be Majorana fermions hybridize to form extended Andreev bound states in the normal region. This phenomenon is a salient feature of the fractional Josephson effect. An order parameter, the Majorana polarization, introduced in Sec. 3.3 is used to investigate the extended zero-energy states in the junction. Finally, the study turned to a ring divided in two regions: a normal metal region and a topological superconducting one with a superconducting phase gradient. The system can be mapped in this case to an SNS junction and again Majorana fermions arise in the normal region when the total phase twist is close to π. It is crucial for future studies to understand in more detail the action of the gradient. The phase gradient has a Cooper pair-breaking effect which can lead to gapless phases in the superconductor. These are large-gradient phases devoid of Majorana fermions. However there are peculiar values where Majorana fermions still form in the normal region. These events are not predicted by the theory and pose an

open question for future studies.

The final Chap. 6 treats a particular model where the presence of time-reversal and chiral symmetries allows the formation of multiple Majorana fermions at the same edge of a wire [127]. It is shown that distant-neighbor pairing terms play the same role as in the 2D $\mathbb{Z}$ topological insulators studied before: they facilitates the increase of the topological invariant and the multiplication of edge states. Moreover, the presence of several Majorana fermions allows to construct SNS junctions between wires in different topologically nontrivial phases. The fractional Josephson effect still characterizes the system and it maintains its signature 4π-periodicity. Furthermore, the multiple Majorana modes can be destroyed by the addition of a phase gradient, which can transform the $\mathbb{Z}$ insulator into a $\mathbb{Z}_2$ insulator with at most one Majorana fermion at an edge. The presence of a phase gradient poses some serious problems; because gradient tends to break the Cooper pairs, the presence of protected zero modes at high gradient values remains to be properly explained.

In perspective, this analysis needs to be carried over to more realistic spinful systems to assess the viability of phases with multiple Majorana. For instance, the spin-coupled semiconducting wire studied before does not seem to be a good candidate, because the magnetic field breaks the TRS necessary to have the $\mathbb{Z}$ insulator. A natural candidate to realize topological $\mathbb{Z}$ superconductors would be a heterostructure involving time-reversal invariant QSH insulators instead [83].

Bibliography

[1] J. Moore, *The birth of topological insulators*, *Nature* **464** (March, 2010) 194–198.

[2] M. Z. Hasan and C. L. Kane, *Colloquium: Topological insulators*, *Rev. Mod. Phys.* **82** (Nov, 2010) 3045–3067.

[3] X.-L. Qi and S.-C. Zhang, *Topological insulators and superconductors*, *Rev. Mod. Phys.* **83** (Oct, 2011) 1057–1110.

[4] C. L. Kane and E. J. Mele, *Quantum spin Hall effect in graphene*, *Phys. Rev. Lett.* **95** (Nov, 2005) 226801.

[5] B. A. Bernevig, T. L. Hughes, and S.-C. Zhang, *Quantum spin Hall effect and topological phase transition in HgTe quantum wells*, *Science* **314** (2006) 1757–1761.

[6] M. König, S. Wiedmann, C. Brüne, A. Roth, H. Buhmann, L. W. Molenkamp, X.-L. Qi, and S.-C. Zhang, *Quantum spin Hall insulator state in HgTe quantum wells*, *Science* **318** (2007) 766–770.

[7] W. Shockley, *On the surface states associated with a periodic potential*, *Phys. Rev.* **56** (Aug, 1939) 317–323.

[8] W. P. Su, J. R. Schrieffer, and A. J. Heeger, *Solitons in polyacetylene*, *Physical Review Letters* **42** (June, 1979) 1698–1701.

[9] K. v. Klitzing, G. Dorda, and M. Pepper, *New method for high-accuracy determination of the fine-structure constant based on quantized Hall resistance*, *Phys. Rev. Lett.* **45** (Aug, 1980) 494–497.

[10] A. Altland and M. R. Zirnbauer, *Nonstandard symmetry classes in mesoscopic normal-superconducting hybrid structures*, *Phys. Rev. B* **55** (Jan, 1997) 1142–1161.

[11] S. Ryu, A. P. Schnyder, A. Furusaki, and A. W. W. Ludwig, *Topological insulators and superconductors: tenfold way and dimensional hierarchy*, *New Journal of Physics* **12** (June, 2010) 065010.

[12] A. Kitaev, *Periodic table for topological insulators and superconductors*, in *Advances in Theoretical Physics: Landau Memorial Conference*, V. Lebedev and M. Feigel'man, eds., vol. 1134, pp. 22–30. AIP, 2009. arXiv:0901.2686 [cond-mat.mes-hall].

[13] A. P. Schnyder, S. Ryu, A. Furusaki, and A. W. W. Ludwig, *Classification of topological insulators and superconductors in three spatial dimensions*, *Phys. Rev. B* **78** (Nov, 2008) 195125.

[14] G. Abramovici and P. Kalugin, *Clifford modules and symmetries of topological insulators*, *International Journal of Geometric Methods in Modern Physics* **09** (2012) 1250023, arXiv:1101.1054 [math-ph].

[15] X.-L. Qi, Y.-S. Wu, and S.-C. Zhang, *General theorem relating the bulk topological number to edge states in two-dimensional insulators*, *Phys. Rev. B* **74** (Jul, 2006) 045125.

[16] A. M. Essin and V. Gurarie, *Bulk-boundary correspondence of topological insulators from their respective Green's functions*, *Phys. Rev. B* **84** (Sep, 2011) 125132.

[17] D. J. Thouless, M. Kohmoto, M. P. Nightingale, and M. den Nijs, *Quantized Hall conductance in a two-dimensional periodic potential*, *Phys. Rev. Lett.* **49** (Aug, 1982) 405–408.

[18] Q. Niu, D. J. Thouless, and Y.-S. Wu, *Quantized Hall conductance as a topological invariant*, *Phys. Rev. B* **31** (Mar, 1985) 3372–3377.

[19] B. I. Halperin, *Quantized Hall conductance, current-carrying edge states, and the existence of extended states in a two-dimensional disordered potential*, *Phys. Rev. B* **25** (Feb, 1982) 2185–2190.

[20] L. Fidkowski and A. Kitaev, *Topological phases of fermions in one dimension*, *Phys. Rev. B* **83** (Feb, 2011) 075103.

[21] E. Tang and X.-G. Wen, *Interaction effects on 1D fermionic symmetry protected topological phases*, arXiv:1204.0520 [cond-mat.str-el].

[22] Z.-C. Gu and X.-G. Wen, *Symmetry-protected topological orders for interacting fermions – fermionic topological non-linear sigma-models and a group super-cohomology theory*, arXiv:1201.2648 [cond-mat.str-el].

[23] F. D. M. Haldane, *Model for a quantum Hall effect without Landau levels: Condensed-matter realization of the "parity anomaly"*, *Phys. Rev. Lett.* **61** (Oct, 1988) 2015–2018.

[24] R. M. Lutchyn, J. D. Sau, and S. Das Sarma, *Majorana fermions and a topological phase transition in semiconductor-superconductor heterostructures*, *Phys. Rev. Lett.* **105** (Aug, 2010) 077001.

[25] Y. Oreg, G. Refael, and F. von Oppen, *Helical liquids and Majorana bound states in quantum wires*, *Phys. Rev. Lett.* **105** (Oct, 2010) 177002.

[26] M. Onoda and N. Nagaosa, *Quantized anomalous Hall effect in two-dimensional ferromagnets: Quantum Hall effect in metals*, *Phys. Rev. Lett.* **90** (May, 2003) 206601.

[27] R. Yu, W. Zhang, H.-J. Zhang, S.-C. Zhang, X. Dai, and Z. Fang, *Quantized anomalous Hall effect in magnetic topological insulators*, *Science* **329** (2010) 61–64.

[28] C.-Z. Chang, J.-S. Zhang, M.-H. Liu, Z.-C. Zhang, X. Feng, K. Li, L.-L. Wang, X. Chen, X. Dai, Z. Fang, X.-L. Qi, S.-C. Zhang, Y. Wang, K. He, X.-C. Ma, and Q.-K. Xue, *Carrier-independent ferromagnetism and giant anomalous Hall effect in magnetic topological insulator*, `arXiv:1108.4754 [cond-mat.mtrl-sci]`.

[29] T.-W. Chen, Z.-R. Xiao, D.-W. Chiou, and G.-Y. Guo, *High Chern number quantum anomalous Hall phases in single-layer graphene with Haldane orbital coupling*, *Phys. Rev. B* **84** (Oct, 2011) 165453.

[30] H. Jiang, Z. Qiao, H. Liu, and Q. Niu, *Quantum anomalous Hall effect with tunable Chern number in magnetic topological insulator film*, *Phys. Rev. B* **85** (Jan, 2012) 045445.

[31] E. Tang, J.-W. Mei, and X.-G. Wen, *High-temperature fractional quantum Hall states*, *Phys. Rev. Lett.* **106** (Jun, 2011) 236802.

[32] K. Sun, Z. Gu, H. Katsura, and S. Das Sarma, *Nearly flatbands with nontrivial topology*, *Phys. Rev. Lett.* **106** (Jun, 2011) 236803.

[33] T. Neupert, L. Santos, C. Chamon, and C. Mudry, *Fractional quantum Hall states at zero magnetic field*, *Phys. Rev. Lett.* **106** (Jun, 2011) 236804.

[34] F. Wang and Y. Ran, *Nearly flat band with Chern number $C = 2$ on the dice lattice*, *Phys. Rev. B* **84** (Dec, 2011) 241103.

[35] Y.-F. Wang, H. Yao, C.-D. Gong, and D. N. Sheng, *Fractional Quantum Hall Effect in Topological Flat Bands with Chern Number Two*, arXiv:1204.1697 [cond-mat.str-el].

[36] M. Trescher and E. J. Bergholtz, *Flat bands with higher Chern number*, arXiv:1205.2245 [cond-mat.str-el].

[37] S. Yang, Z.-C. Gu, K. Sun, and S. Das Sarma, *Topological flat band models with arbitrary Chern numbers*, arXiv:1205.5792 [cond-mat.str-el].

[38] D. Sticlet, F. Piéchon, J.-N. Fuchs, P. Kalugin, and P. Simon, *Geometrical engineering of a two-band Chern insulator in two dimensions with arbitrary topological index*, *Phys. Rev. B* **85** (Apr, 2012) 165456.

[39] J. E. Avron, L. Sadun, J. Segert, and B. Simon, *Topological invariants in Fermi systems with time-reversal invariance*, *Phys. Rev. Lett.* **61** (Sep, 1988) 1329–1332.

[40] Y. Hatsugai, *Edge states in the integer quantum Hall effect and the Riemann surface of the Bloch function*, *Phys. Rev. B* **48** (Oct, 1993) 11851–11862.

[41] M. Kohmoto, *Topological invariant and the quantization of the Hall conductance*, *Annals of Physics* **160** (April, 1985) 343 – 354.

[42] J. E. Avron, R. Seiler, and B. Simon, *Homotopy and quantization in condensed matter physics*, *Phys. Rev. Lett.* **51** (Jul, 1983) 51–53.

[43] M. Stone and P. Goldbart, *Mathematics for Physics*. Cambridge University Press, 2009.

[44] P. Milnor, *Topology from a Differential Viewpoint*. University Press of Virginia, 1965.

[45] B. A. Dubrovin, A. T. Fomenko, and S. P. Novikov, *Modern Geometry-Methods and Applications*, vol. 2. Springer, 1985.

[46] Z. Wang, X.-L. Qi, and S.-C. Zhang, *Equivalent topological invariants of topological insulators*, *New Journal of Physics* **12** (2010) 065007.

[47] G. Volovik, *Universe in a Helium Droplet*. Clarendon Press, 2003.

[48] G. E. Volovik, *Topology of quantum vacuum*, arXiv:1111.4627 [hep-ph].

[49] H. Nielsen and M. Ninomiya, *Absence of neutrinos on a lattice: (I). Proof by homotopy theory*, *Nuclear Physics B* **185** (1981) 20 – 40.

[50] D. N. Sheng, Z. Y. Weng, L. Sheng, and F. D. M. Haldane, *Quantum spin-Hall effect and topologically invariant Chern numbers*, *Phys. Rev. Lett.* **97** (Jul, 2006) 036808.

[51] E. H. Lieb, *Two theorems on the hubbard model*, *Phys. Rev. Lett.* **62** (Mar, 1989) 1201–1204.

[52] C. L. Kane and E. J. Mele, *Z_2 topological order and the quantum spin Hall effect*, *Phys. Rev. Lett.* **95** (Sep, 2005) 146802.

[53] D. Sticlet and F. Piéchon, *Distant-Neighbor Hopping in Graphene and Haldane Models*, `arXiv:1212.4046 [cond-mat.mes-hall]`.

[54] C. Bena and L. Simon, *Dirac point metamorphosis from third-neighbor couplings in graphene and related materials*, *Phys. Rev. B* **83** (Mar, 2011) 115404.

[55] J. L. Mañes, F. Guinea, and M. A. H. Vozmediano, *Existence and topological stability of Fermi points in multilayered graphene*, *Phys. Rev. B* **75** (Apr, 2007) 155424.

[56] G. Montambaux, F. Piéchon, J.-N. Fuchs, and M. O. Goerbig, *A universal Hamiltonian for motion and merging of Dirac points in a two-dimensional crystal*, *European Physical Journal B* **72** (Dec., 2009) 509–520.

[57] A. M. Essin and J. E. Moore, *Topological insulators beyond the Brillouin zone via Chern parity*, *Phys. Rev. B* **76** (Oct, 2007) 165307.

[58] R. Roy, *Z_2 classification of quantum spin Hall systems: An approach using time-reversal invariance*, *Phys. Rev. B* **79** (May, 2009) 195321.

[59] R. S. K. Mong and V. Shivamoggi, *Edge states and the bulk-boundary correspondence in Dirac Hamiltonians*, *Phys. Rev. B* **83** (Mar, 2011) 125109.

[60] S. S. Pershoguba and V. M. Yakovenko, *The Shockley model description of the surface states in topological insulators*, `arXiv:1202.5526 [cond-mat.str-el]`.

[61] C. Wu, B. A. Bernevig, and S.-C. Zhang, *Helical liquid and the edge of quantum spin Hall systems*, *Phys. Rev. Lett.* **96** (Mar, 2006) 106401.

[62] C. L. Kane and E. J. Mele, *Z_2 topological order and the quantum spin Hall effect*, *Phys. Rev. Lett.* **95** (Sep, 2005) 146802.

[63] A. R. Akhmerov and C. W. J. Beenakker, *Boundary conditions for Dirac fermions on a terminated honeycomb lattice*, *Phys. Rev. B* **77** (Feb, 2008) 085423.

[64] P. Delplace, D. Ullmo, and G. Montambaux, *Zak phase and the existence of edge states in graphene*, *Phys. Rev. B* **84** (Nov, 2011) 195452.

[65] G. W. Semenoff, V. Semenoff, and F. Zhou, *Domain walls in gapped graphene*, *Phys. Rev. Lett.* **101** (Aug, 2008) 087204.

[66] J. Li, I. Martin, M. Büttiker, and A. F. Morpurgo, *Marginal topological properties of graphene: a comparison with topological insulators*, *Physica Scripta Volume T* **146** (Jan., 2012) 014021, arXiv:1110.1969 [cond-mat.mes-hall].

[67] A. Y. Kitaev, *Unpaired Majorana fermions in quantum wires*, *Physics-Uspekhi* **44** (Oct, 2001) 131, arXiv:0010440 [cond-mat].

[68] E. Majorana, *Teoria simmetrica dell'elettrone e del positrone*, *Il Nuovo Cimento (1924-1942)* **14** (1937) 171–184.

[69] A. Zee, *Quantum Field Theory in a Nutshell*. Princeton University Press, Mar., 2003.

[70] M. Srednicki, *Quantum Field Theory*. Cambridge University Press, Jan., 2007.

[71] N. Read and D. Green, *Paired states of fermions in two dimensions with breaking of parity and time-reversal symmetries and the fractional quantum Hall effect*, *Phys. Rev. B* **61** (Apr, 2000) 10267–10297.

[72] P. G. De Gennes, *Superconductivity Of Metals And Alloys*. Westview Press, Mar., 1999.

[73] C. Nayak, S. H. Simon, A. Stern, M. Freedman, and S. Das Sarma, *Non-Abelian anyons and topological quantum computation*, *Rev. Mod. Phys.* **80** (Sep, 2008) 1083–1159.

[74] D. A. Ivanov, *Non-Abelian statistics of half-quantum vortices in p-wave superconductors*, *Phys. Rev. Lett.* **86** (Jan, 2001) 268–271.

[75] C. W. J. Beenakker, *Search for Majorana fermions in superconductors*, arXiv:1112.1950 [cond-mat.mes-hall].

[76] J. Alicea, *New directions in the pursuit of Majorana fermions in solid state systems*, *Reports on Progress in Physics* **75** (June, 2012) 076501.

[77] C. Caroli, P. D. Gennes, and J. Matricon, *Bound fermion states on a vortex line in a type II superconductor*, *Physics Letters* **9** (1964) 307 – 309.

[78] N. Read and G. Moore, *Fractional quantum hall effect and nonabelian statistics*, *Progress of Theoretical Physics Supplement* **107** (1992) 157–166.

[79] S. Das Sarma, C. Nayak, and S. Tewari, *Proposal to stabilize and detect half-quantum vortices in strontium ruthenate thin films: Non-Abelian braiding statistics of vortices in a $p_x + ip_y$ superconductor*, *Phys. Rev. B* **73** (Jun, 2006) 220502.

[80] J. Jang, D. G. Ferguson, V. Vakaryuk, R. Budakian, S. B. Chung, P. M. Goldbart, and Y. Maeno, *Observation of half-height magnetization steps in Sr_2RuO_4*, *Science* **331** (2011) 186–188.

[81] V. Gurarie, L. Radzihovsky, and A. V. Andreev, *Quantum phase transitions across a p-wave Feshbach resonance*, *Phys. Rev. Lett.* **94** (Jun, 2005) 230403.

[82] S. Tewari, S. Das Sarma, C. Nayak, C. Zhang, and P. Zoller, *Quantum computation using vortices and Majorana zero modes of a $p_x + ip_y$ superfluid of fermionic cold atoms*, *Phys. Rev. Lett.* **98** (Jan, 2007) 010506.

[83] L. Fu and C. L. Kane, *Superconducting proximity effect and Majorana fermions at the surface of a topological insulator*, *Phys. Rev. Lett.* **100** (Mar, 2008) 096407.

[84] A. Cook and M. Franz, *Majorana fermions in a topological-insulator nanowire proximity-coupled to an s-wave superconductor*, *Phys. Rev. B* **84** (Nov, 2011) 201105.

[85] P. Hosur, P. Ghaemi, R. S. K. Mong, and A. Vishwanath, *Majorana modes at the ends of superconductor vortices in doped topological insulators*, *Phys. Rev. Lett.* **107** (Aug, 2011) 097001.

[86] J. R. Williams, A. J. Bestwick, P. Gallagher, S. S. Hong, Y. Cui, A. S. Bleich, J. G. Analytis, I. R. Fisher, and D. Goldhaber-Gordon, *Signatures of Majorana fermions in hybrid superconductor-topological insulator devices*, `arXiv:1202.2323 [cond-mat.mes-hall]`.

[87] J. D. Sau, R. M. Lutchyn, S. Tewari, and S. Das Sarma, *Generic new platform for topological quantum computation using semiconductor heterostructures*, *Phys. Rev. Lett.* **104** (Jan, 2010) 040502.

[88] J. Alicea, *Majorana fermions in a tunable semiconductor device*, *Phys. Rev. B* **81** (Mar, 2010) 125318.

[89] I. C. Fulga, F. Hassler, A. R. Akhmerov, and C. W. J. Beenakker, *Scattering formula for the topological quantum number of a disordered multimode wire*, *Phys. Rev. B* **83** (Apr, 2011) 155429.

[90] T. D. Stanescu, R. M. Lutchyn, and S. Das Sarma, *Majorana fermions in semiconductor nanowires*, *Phys. Rev. B* **84** (Oct, 2011) 144522.

[91] V. Mourik, K. Zuo, S. M. Frolov, S. R. Plissard, E. P. A. M. Bakkers, and L. P. Kouwenhoven, *Signatures of Majorana fermions in hybrid superconductor-semiconductor nanowire devices*, *Science* **336** (2012) 1003–1007.

[92] A. Das, Y. Ronen, Y. Most, Y. Oreg, M. Heiblum, and H. Shtrikman, *Evidence of Majorana fermions in an Al – InAs nanowire topological superconductor*, arXiv:1205.7073 [cond-mat.mes-hall].

[93] T.-P. Choy, J. M. Edge, A. R. Akhmerov, and C. W. J. Beenakker, *Majorana fermions emerging from magnetic nanoparticles on a superconductor without spin-orbit coupling*, *Phys. Rev. B* **84** (Nov, 2011) 195442.

[94] M. Kjaergaard, K. Wölms, and K. Flensberg, *Majorana fermions in superconducting nanowires without spin-orbit coupling*, *Phys. Rev. B* **85** (Jan, 2012) 020503.

[95] M. Sato and S. Fujimoto, *Topological phases of noncentrosymmetric superconductors: Edge states, Majorana fermions, and non-Abelian statistics*, *Phys. Rev. B* **79** (Mar, 2009) 094504.

[96] S. Fujimoto, *Topological order and non-Abelian statistics in noncentrosymmetric s-wave superconductors*, *Phys. Rev. B* 77 (Jun, 2008) 220501.

[97] M. Sato, Y. Takahashi, and S. Fujimoto, *Non-Abelian topological order in s-wave superfluids of ultracold fermionic atoms*, *Phys. Rev. Lett.* **103** (Jul, 2009) 020401.

[98] L. Fu and C. L. Kane, *Probing neutral Majorana fermion edge modes with charge transport*, *Phys. Rev. Lett.* **102** (May, 2009) 216403.

[99] A. R. Akhmerov, J. Nilsson, and C. W. J. Beenakker, *Electrically detected interferometry of Majorana fermions in a topological insulator*, *Phys. Rev. Lett.* **102** (May, 2009) 216404.

[100] L. Fu, *Electron teleportation via Majorana bound states in a mesoscopic superconductor*, *Phys. Rev. Lett.* **104** (Feb, 2010) 056402.

[101] A. Zazunov, A. L. Yeyati, and R. Egger, *Coulomb blockade of Majorana-fermion-induced transport*, *Phys. Rev. B* **84** (Oct, 2011) 165440.

[102] H.-J. Kwon, V. M. Yakovenko, and K. Sengupta, *Fractional ac Josephson effect in unconventional superconductors*, *Low Temperature Physics* **30** (July, 2004) 613–619, arXiv:0401313 [cond-mat].

[103] K. T. Law, P. A. Lee, and T. K. Ng, *Majorana fermion induced resonant Andreev reflection*, *Phys. Rev. Lett.* **103** (Dec, 2009) 237001.

[104] K. Flensberg, *Tunneling characteristics of a chain of Majorana bound states*, *Phys. Rev. B* **82** (Nov, 2010) 180516.

[105] D. Bagrets and A. Altland, *Class D spectral peak in Majorana quantum wires*, arXiv:1206.0434 [cond-mat.mes-hall].

[106] J. Liu, A. C. Potter, K. T. Law, and P. A. Lee, *Zero-bias peaks in spin-orbit coupled superconducting wires with and without Majorana end-states*, arXiv:1206.1276 [cond-mat.mes-hall].

[107] E. J. H. Lee, X. Jiang, R. Aguado, G. Katsaros, C. M. Lieber, and S. De Franceschi, *Zero-bias anomaly in a nanowire quantum dot coupled to superconductors*, arXiv:1207.1259 [cond-mat.mes-hall].

[108] E. M. Stoudenmire, J. Alicea, O. A. Starykh, and M. P. Fisher, *Interaction effects in topological superconducting wires supporting Majorana fermions*, *Phys. Rev. B* **84** (Jul, 2011) 014503.

[109] A. C. Potter and P. A. Lee, *Engineering a $p + ip$ superconductor: Comparison of topological insulator and Rashba spin-orbit-coupled materials*, *Phys. Rev. B* **83** (May, 2011) 184520.

[110] J. D. Sau, S. Tewari, and S. Das Sarma, *Experimental and materials considerations for the topological superconducting state in electron- and hole-doped semiconductors: Searching for non-Abelian Majorana modes in 1D nanowires and 2D heterostructures*, *Phys. Rev. B* **85** (Feb, 2012) 064512.

[111] D. Sticlet, C. Bena, and P. Simon, *Spin and Majorana polarization in topological superconducting wires*, *Phys. Rev. Lett.* **108** (Mar, 2012) 096802.

[112] R. Shindou, A. Furusaki, and N. Nagaosa, *Quantum impurity spin in Majorana edge fermions*, *Phys. Rev. B* **82** (Nov, 2010) 180505.

[113] R. Žitko and P. Simon, *Quantum impurity coupled to Majorana edge fermions*, *Phys. Rev. B* **84** (Nov, 2011) 195310.

[114] G. Dresselhaus, *Spin-orbit coupling effects in zinc blende structures*, *Phys. Rev.* **100** (Oct, 1955) 580–586.

[115] J. Schliemann, J. C. Egues, and D. Loss, *Nonballistic spin-field-effect transistor*, *Phys. Rev. Lett.* **90** (Apr, 2003) 146801.

[116] C. J. Bolech and E. Demler, *Observing Majorana bound states in p-wave superconductors using noise measurements in tunneling experiments*, *Phys. Rev. Lett.* **98** (Jun, 2007) 237002.

[117] A. R. Akhmerov, J. P. Dahlhaus, F. Hassler, M. Wimmer, and C. W. J. Beenakker, *Quantized conductance at the Majorana phase transition in a disordered superconducting wire*, *Phys. Rev. Lett.* **106** (Jan, 2011) 057001.

[118] L. Fidkowski, J. Alicea, N. H. Lindner, R. M. Lutchyn, and M. P. A. Fisher, *Universal transport signatures of Majorana fermions in superconductor- Luttinger liquid junctions*, *Phys. Rev. B* **85** (Jun, 2012) 245121.

[119] L. Fu and C. L. Kane, *Josephson current and noise at a superconductor/quantum-spin-Hall-insulator/superconductor junction*, *Phys. Rev. B* **79** (Apr, 2009) 161408.

[120] P. A. Ioselevich and M. V. Feigel'man, *Anomalous Josephson current via Majorana bound states in topological insulators*, *Phys. Rev. Lett.* **106** (Feb, 2011) 077003.

[121] L. Jiang, D. Pekker, J. Alicea, G. Refael, Y. Oreg, and F. von Oppen, *Unconventional Josephson signatures of Majorana bound states*, *Phys. Rev. Lett.* **107** (Nov, 2011) 236401.

[122] D. Chevallier, D. Sticlet, P. Simon, and C. Bena, *Mutation of Andreev into Majorana bound states in long superconductor-normal and superconductor-normal-superconductor junctions*, *Phys. Rev. B* **85** (Jun, 2012) 235307.

[123] J. Klinovaja and D. Loss, *Composite Majorana fermion wave functions in nanowires*, *Phys. Rev. B* **86** (Aug, 2012) 085408.

[124] B. Josephson, *Possible new effects in superconductive tunnelling*, *Physics Letters* **1** (1962) 251 – 253.

[125] A. Romito, J. Alicea, G. Refael, and F. von Oppen, *Manipulating Majorana fermions using supercurrents*, *Phys. Rev. B* **85** (Jan, 2012) 020502.

[126] S. Tewari and J. D. Sau, *Topological invariants for spin-orbit coupled superconductor nanowires*, `arXiv:1111.6592 [cond-mat.mes-hall]`.

[127] Y. Niu, S. B. Chung, C.-H. Hsu, I. Mandal, S. Raghu, and S. Chakravarty, *Majorana zero modes in a quantum Ising chain with longer-ranged interactions*, *Phys. Rev. B* **85** (Jan, 2012) 035110.

[128] M. Diez, J. P. Dahlhaus, M. Wimmer, and C. W. J. Beenakker, *Andreev reflection from a topological superconductor with chiral symmetry*, `arXiv:1206.3079 [cond-mat.mes-hall]`.

[129] D. Sticlet, C. Bena, and P. Simon, *Josephson effect in superconducting wires supporting multiple Majorana edge states*, `arXiv:1211.3070 [cond-mat.mes-hall]`.

[130] J. Alicea, Y. Oreg, G. Refael, F. von Oppen, and M. P. A. Fisher, *Non-Abelian statistics and topological quantum information processing in 1D wire networks*, *Nature Physics* 7 (Aug, 2011) 412.

[131] D. M. Badiane, M. Houzet, and J. S. Meyer, *Nonequilibrium Josephson effect through helical edge states*, *Phys. Rev. Lett.* **107** (Oct, 2011) 177002.